

Development of Three-Axis Soft Tactile
Sensor Using Tilted Capacitive-Type
Transducers

複数の静電容量型柔軟触覚デバイスを
用いた三軸力センサの開発

July 2016

Waseda University
Graduate School of Creative Science and Engineering
Department of Modern Mechanical Engineering,
Research on Intelligent Machines

Sophon SOMLOR

ソムロア ソフォン

*To my parents, my family,
and Eve*

ABSTRACT

The sense of touch is not only a very important ability for humans but for robots as well. It can lead to safe, robust, and reliable interactions with unknown environments and especially with humans. With tactile sensors, local information (force magnitude and direction) of each contact force can be extracted including the position of the contact. Therefore, they are often used as robotic skins to detect external contact force. However, most tactile sensors are not soft, flat, flexible, nor able to measure tri-axial force.

This thesis is aimed to develop a sensitive yet soft and flexible robotic skin sensor with tri-axial force sensing capability based on a novel transducers arrangement. Capacitive sensing is preferred due to its advantages and also the availability of a small-sized capacitance-to-digital converter (CDC). The problems often found in capacitive sensing were handled. A thin copper beryllium plate with a thick bump was introduced and used as a deformable capacitive plate. Copper beryllium was used due to its good spring property, high strength, and high conductivity. The bump can increase sensitivity and measurement range because it provides a more uniform and more parallel deformation when the plate is loaded with an external force. The developed sensor not only has high signal-to-noise ratio (SNR), low hysteresis, and is able to counteract thermal drift, but also local digitization and I2C bus is supported; this could drastically reduce the required space. The biggest contribution lies in the development of the novel tactile sensor with a novel configuration of tilting the four transducers in four different directions. This allows the sensor to measure tri-axial force and also being both soft and sensitive at the same time. The experimental results showed that the measurement of tri-axial force can be successfully done with this soft skin sensor. The exerting force vector can be directly calculated from the sensing of the four tilting transducers.

ACKNOWLEDGEMENTS

First of all, I would like to thank my supervisor, Professor Shigeki Sugano, and Assistant Professor Alexander Schmitz who was always available for my questions, guided me, and supported me throughout my memorable years of Ph.D. I have learned a lot of valuable ways of thinking, and has received many inspirations and great opportunities to widen my vision from them. Professor Sugano never hesitate to give me opportunities to learn new things such as giving me a Super Global University (SGU) grant that allow me to do short-term research abroad. Furthermore, I have learned countless things about tactile sensing and received the encouraging idea which led to the topic of my thesis from Assistant Professor Schmitz. The thesis would not have been possible without him. He also proofread my writings many times and always taught me how to improve my English. Furthermore, I would like to thank Professor Masakatsu G. Fujie, Professor Hiroyasu Iwata, Professor Tomoyuki Miyashita, and Professor Tetsuya Ogata for kindly proofreading this thesis several times even with the busy schedules they had.

Moreover, I also would like to thank the people at Waseda University, especially the members of Sugano laboratory and Graduate Program for Embodiment Informatics “Kobo” for supporting me throughout the time I have spent there. In particular, I would like to thank you Richard Sahala Hartanto, a very hard-working student, and a fast learner. He always tried his best to help me even when the tasks were challenging. I also learned a lot from him. I would like to thank Gonzalo Aguirre Dominguez, a good friend who always gave me many valuable opinions. We exchanged many ideas and solutions over many problems. I would like to thank Assistant Professor Mitsuhiro Kamezaki and also Dr. Matthieu Destephe for a lot of guidance about my research and also doctorate regulation. Furthermore, I would like to thank my lab members especially Kuniyuki Takahashi, Shingo Murata, Shunsuke Nagahama, and Junjie Yang. We have been through the unforgettable Ph.D. years together. They had helped me in several ways such as complicated doctorate procedure and many regulations. My fruitful years of Ph.D. would be much more difficult without the kind helps from the secretaries of Sugano lab, Yoko Ono, Kyoko Arai, and the secretaries of Kobo, Atsuko Tsuriya, Madoka Kuniyasu, who always very welcome to help me out with any paperwork and purchasing.

Furthermore, I would like also to thank all of the members of Institute of Cognitive Systems, Technical University of Munich, for their kind and warm hospitality given to me during my 3-month research. In particularly, I would like to give my gratitude to

Professor Gordon Cheng, Dr. Emmanuel Carlos Dean Leon, and, Mohsen Kaboli who had been working closely with me and giving me valuable and countless advice that enhanced my knowledge and way of thinking. Professor Cheng also kindly allowed me to be one of the honorable Marie Curie fellows and a part of CONTEST (COLlaborative Network for Training in Electronic Skin Technology) program where I had a great chance to meet and learn from other great researchers in the field of robotic skin. I would like to thank Dr. Philipp Mittendorfer. Florian Bergner, Katharina Bulla for their kind support in many aspects of research-related and technical issues, and Ilona Nar-Witte for her kind support in countless administration-related matters.

I would like to thank Dr.-Ing. Christian Ott and Sebastian Wolf for their generous hospitality during my visit at Institute of Robotics and Mechatronics, German Aerospace Center (DLR). They were willing to show me many interesting robots and kindly answers my questions. I have learned a lot from them.

This work was supported by the JSPS Grant-in-Aid for Scientific Research (S) [grant number 25220005], JSPS Grant-in-Aid for Young Scientists (B) [grant number 15K21443], Research Institute for Science and Engineering of Waseda University, and the Program for Leading Graduate Schools, ‘Graduate Program for Embodiment Informatics’ of the Ministry of Education, Culture, Sports, Science and Technology.

Thank you to Kayla Friedman and Malcolm Morgan of the Centre for Sustainable Development, University of Cambridge, the UK for producing the Microsoft Word thesis template used to produce this thesis.

Last but not least, I would like to thank my parents, my family, and Eve, my girlfriend who were always there to support me, stay beside me, and be the ones that I could talk to even though we have lived in the different countries. I would not be able to start my Ph.D. here in Waseda University without their constant encouragement, and support. Furthermore, I would like to thank Mrs. Rattana Chaichanakol, the founder of UNIPART Co., Ltd. who has always supported me since my Master degree, believed in my potential, and taught me countless meaningful things that I could not learn from books. Without her kind help, I would not be able to start my graduate study. Finally, I also want to thank all of my friends in Japan and in Thailand who were always supportive and believed in me.

CONTENTS

| | |
|---|-----------|
| 1 INTRODUCTION..... | 15 |
| 1.1 MOTIVATION..... | 15 |
| 1.2 BACKGROUND | 18 |
| 1.2.1 <i>Importance of tactile sensing</i> | 18 |
| 1.2.2 <i>Current state of tactile sensor development</i> | 18 |
| 1.2.3 <i>Existing tactile and force-torque sensors</i> | 18 |
| 1.3 AIMS AND OBJECTIVES..... | 26 |
| 1.4 NOVEL CONTRIBUTION..... | 27 |
| 1.5 THESIS OUTLINE..... | 29 |
| 1.5.1 <i>Chapter 2</i> | 29 |
| 1.5.2 <i>Chapter 3</i> | 29 |
| 1.5.3 <i>Chapter 4</i> | 30 |
| 1.5.4 <i>Chapter 5</i> | 30 |
| 2 CAPACITIVE-TYPE FORCE TRANSDUCER WITH A BUMP..... | 31 |
| 2.1 CONCEPT | 31 |
| 2.2 IMPLEMENTATION | 33 |
| 2.2.1 <i>Digitization of the Capacitance</i> | 33 |
| 2.2.2 <i>Temperature Compensation Pad</i> | 34 |
| 2.2.3 <i>The Sensor</i> | 34 |
| 2.2.4 <i>Copper Beryllium Plate with Bump</i> | 36 |
| 2.3 EXPERIMENTS..... | 41 |
| 2.3.1 <i>Experimental setup</i> | 41 |
| 2.3.2 <i>Result and discussion</i> | 43 |
| 2.4 CONCLUSION | 47 |
| 3 DISTRIBUTED TACTILE SENSING OF MR-FLUID HAPTIC INTERFACE | 48 |
| 3.1 BRIEF INTRODUCTION TO HAPTIC INTERFACE AND MAGNETORHEOLOGICAL FLUID | 49 |
| 3.2 CONCEPT | 50 |
| 3.3 IMPLEMENTATION | 50 |
| 3.3.1 <i>Electromagnet</i> | 51 |
| 3.3.2 <i>Device's support structure</i> | 51 |
| 3.3.3 <i>MR fluid pouch</i> | 52 |
| 3.3.4 <i>Haptic Interface</i> | 53 |
| 3.4 EXPERIMENTS..... | 54 |

| | |
|---|------------|
| 3.4.1 <i>Experiment setup</i> | 54 |
| 3.4.2 <i>Result and discussion</i> | 55 |
| 3.5 CONCLUSION | 59 |
| 4 3-AXIS DISTRIBUTED SOFT SKIN SENSOR..... | 60 |
| 4.1 CONCEPT | 60 |
| 4.2 IMPLEMENTATION: VERSION 1 | 62 |
| 4.2.1 <i>Circuit design and manufacturing</i> | 62 |
| 4.2.2 <i>Sensor molding</i> | 66 |
| 4.2.3 <i>Experiments setup</i> | 71 |
| 4.2.4 <i>Pre-mold experimental result</i> | 74 |
| 4.2.5 <i>Discussion</i> | 84 |
| 4.3 IMPLEMENTATION: VERSION 2 | 85 |
| 4.3.1 <i>Circuit redesign</i> | 86 |
| 4.3.2 <i>Improved production process</i> | 89 |
| 4.3.3 <i>Conductive ink</i> | 95 |
| 4.3.4 <i>Bending angle assessment</i> | 97 |
| 4.3.5 <i>Sensor molding improvement</i> | 97 |
| 4.3.6 <i>Experiments setup</i> | 98 |
| 4.3.7 <i>Result and discussion</i> | 102 |
| 4.4 CONCLUSION | 107 |
| 5 CONCLUSION AND FUTURE WORK | 110 |
| 5.1 CONCLUSION | 110 |
| 5.2 FUTURE WORK..... | 112 |
| REFERENCES..... | 115 |
| LIST OF PUBLICATION..... | 123 |
| RELATED PUBLICATION..... | 123 |
| ADDITIONAL PUBLICATION | 123 |

LIST OF TABLES

| | |
|--|-----|
| TABLE 1.1 GENERAL COMPARISON BETWEEN DIFFERENT TRANSDUCING TECHNOLOGIES. | 19 |
| TABLE 2.1 THE PROPERTIES OF COPPER BERYLLIUM CW101C R580 (ALLOY 25 1/2H, C17200 TD02)..... | 36 |
| TABLE 4.1 THE COMPARISON OF THE SNRdB VALUE OF EACH SENSING ELEMENT THE MOLDING..... | 75 |
| TABLE 4.2 THE LIST OF WEIGHTS WHICH WILL BE PUT ON A SINGLE FORCE SENSING UNIT DURING THE ACCUMULATED LOAD TEST AT EACH STEP. THE LOADING SEQUENCE GOES FROM 0 TO 17 AND THE UNLOADING SEQUENCE GOES FROM 17 TO 0..... | 76 |
| TABLE 4.3 THE COMPARISON OF THE SNRdB VALUE OF EACH SENSING ELEMENT BEFORE AND AFTER THE MOLDING. | 80 |
| TABLE 4.4. THE COMPARISON OF THE FORCE VECTOR CALCULATION'S ACCURACY AT ALL EXPERIMENTS IN THE TRIAXIAL FORCE TEST SECTION. | 106 |
| TABLE 5.1. THE SPECIFICATION OF THE CAPACITIVE-TYPE FORCE TRANSDUCER DEVELOPED IN CHAPTER 2..... | 111 |
| TABLE 5.2. THE SPECIFICATION OF THE SECOND VERSION OF THE 3-AXIS SOFT SKIN SENSOR DEVELOPED IN CHAPTER 4. | 112 |

LIST OF FIGURES

| | |
|--|----|
| FIGURE 1.1 AN EXAMPLE OF EXISTING PIEZOELECTRIC-BASED SENSORS..... | 20 |
| FIGURE 1.2 AN EXAMPLE OF EXISTING OPTICAL-BASED TACTILE SENSORS | 21 |
| FIGURE 1.3 AN EXAMPLE OF EXISTING HALL EFFECT-BASED SENSORS..... | 22 |
| FIGURE 1.4 AN EXAMPLE OF EXISTING SENSORS BASED ON PRESSURE-SENSITIVE ELECTRIC CONDUCTIVE RUBBER (PSECR)..... | 22 |
| FIGURE 1.5 AN EXAMPLE OF EXISTING PIEZORESISTIVE-BASED SENSORS. | 24 |
| FIGURE 1.6 AN EXAMPLE OF EXISTING CAPACITIVE-BASED SENSORS..... | 25 |
| FIGURE 2.1 SIDE VIEW OF A SINGLE FORCE SENSING UNIT | 32 |
| FIGURE 2.2 CAPACITANCE MEASUREMENT USING AD7147..... | 33 |
| FIGURE 2.3 THE CAPACITIVE FORCE SENSOR..... | 35 |
| FIGURE 2.4 THE CONFIRMATION OF THE CAPACITOR'S GAP | 35 |
| FIGURE 2.5 THE ANSYS SIMULATION OF A $6 \times 6 \times 0.1$ MM 3 CUBE ₂ PLATE SUBJECT TO A 5 N LOAD..... | 38 |
| FIGURE 2.6 THE SUPPORTS UNDER THE CUBE ₂ PLATE IN THE SIMULATION | 38 |
| FIGURE 2.7 THE ANSYS SIMULATION OF A $6 \times 6 \times 0.1$ MM 3 CUBE ₂ PLATE WITH THE 0.31 MM-HIGH, Ø3 MM CYLINDER BUMP SUBJECT TO A 5 N LOAD..... | 39 |
| FIGURE 2.8 THE FINAL DIMENSION OF THE COPPER PLATE WITH A BUMP..... | 40 |
| FIGURE 2.9 THE COPPER BERYLLIUM PLATE WITH A BUMP WHICH IS PRODUCED BY PHOTOLITHOGRAPHIC ETCHING..... | 41 |
| FIGURE 2.10 OVERVIEW OF THE EXPERIMENTAL SETUP | 42 |
| FIGURE 2.11 OVERVIEW OF THE TEMPERATURE DRIFT TEST SETUP. | 42 |
| FIGURE 2.12 THE RESPONSE OF THE SINGLE FORCE SENSING UNIT S ₁ TO THE LOAD OF 0.254 KG. | 44 |
| FIGURE 2.13 THE RESPONSE OF THE SINGLE FORCE SENSING UNIT S ₁ TO THE LOAD OF 1.044 KG. | 44 |
| FIGURE 2.14 THE RESPONSE OF THE CAPACITIVE SENSOR S ₁ WHICH WAS SUBJECTED TO DIFFERENT LOADS IS PLOTTED AGAINST TIME..... | 45 |

| | |
|---|----|
| FIGURE 2.15 LOADING/UNLOADING TEST PLOT OF THE AVERAGE OF THE SENSOR READOUT. THE LOAD IS RANGE FROM 0.045 KG TO 1.144 KG..... | 46 |
| FIGURE 2.16 THE EFFECT OF TEMPERATURE CHANGE ON THE SENSOR IS SHOWN TOGETHER WITH AN ATTEMPT OF COMPENSATION OF SENSOR READOUT (S_1 , GREEN) READOUT (CYAN)..... | 47 |
| FIGURE 3.1 THE DIAGRAM SHOWING THE WORKING PRINCIPLE OF THE DEVICE AND THE LOCATION OF EACH COMPONENT..... | 50 |
| FIGURE 3.2 THE ELECTROMAGNET USED IN THE PROPOSED HAPTIC INTERFACE..... | 51 |
| FIGURE 3.3 THE TOP AND BOTTOM SUPPORT FOR THE SENSOR AND THE MR-FILLED POUCH. | 52 |
| FIGURE 3.4 THE PROCESS OF FORMING AN IMPRESSION OF SEALANT RIDGE ON THE TWO NITRILE RUBBER SHEETS..... | 53 |
| FIGURE 3.5 THE FINISHED DEVICE, FROM ABOVE, THE POUCH (BLUE) FILLED WITH MR FLUID CAN BE SEEN..... | 54 |
| FIGURE 3.6 THE BOTTOM SIDE OF THE DEVICE..... | 54 |
| FIGURE 3.7 EXPERIMENTAL SETUP WITH A SET OF WEIGHT AND THE VERTICAL FORCE TRANSFER STRUCTURE..... | 56 |
| FIGURE 3.8 EXPERIMENTAL SETUP WITH A VOICE COIL MOTOR, TWO MOTOR DRIVERS, ARDUINO DUE AND AN AMMETER..... | 56 |
| FIGURE 3.9 SENSOR RESPONSE TO DIFFERENT LOADS WHEN THE MAGNET IS NOT POWERED | 57 |
| FIGURE 3.10 SENSOR RESPONSE TO DIFFERENT LOADS WHEN THE MAGNET IS POWERED WITH 2 A..... | 57 |
| FIGURE 3.11 SENSOR RESPONSE TO DIFFERENT LOADS WHEN THE MAGNET IS POWERED WITH 4 A..... | 57 |
| FIGURE 3.12 SPATIAL RESPONSE OF THE SENSOR TO THE LOAD OF 450 G WITH 2 MM SPACING BETWEEN EACH PUSH..... | 58 |
| FIGURE 3.13 THE LAYOUT SHOWING THE LOCATION OF EACH SENSING UNIT WITH DESIGNATED NUMBER..... | 59 |

| | |
|---|-------|
| FIGURE 4.1 THE CONCEPTUAL DESIGN OF THE PROPOSED 3-AXIS DISTRIBUTED SKIN SENSOR. | 61 |
| | |
| FIGURE 4.2 THE FORCE DETECTION PRINCIPLE OF THE PROPOSED SKIN SENSOR. | 62 |
| FIGURE 4.3 THE OVERVIEW OF THE CIRCUIT..... | 63 |
| FIGURE 4.4 THE COMPARISON OF THE SIZE OF THE SURROUNDING PAD OF THE TWO DESIGNS. | |
| | 64 |
| FIGURE 4.5 THE COMPARISON BETWEEN THE SIZE OF THE COPPER BERYLLIUM PLATE AND THE SIZE OF THE SURROUNDING PAD CAN BE SEEN; THE PLATE WAS SLIGHTLY SMALLER..... | 64 |
| FIGURE 4.6 THE SENSOR's PCB AFTER ALL OF THE COMPONENTS WERE SOLDERED TO IT.66 | |
| FIGURE 4.7 THE SILICONE RUBBER USED TO MAKE THE SOFT SKIN SENSOR. | 67 |
| FIGURE 4.8 THE CROSS SECTION VIEW SHOWS HOW THE TRIANGULAR SUPPORT CONTACT WITH THE CuBe ₂ PLATE. | 68 |
| FIGURE 4.9 THE FIRST MOLD USES IN MAKING THE TRIANGULAR SUPPORT SILICONE. | 69 |
| FIGURE 4.10 THE SECOND MOLD USES IN MAKING THE TRIANGULAR SUPPORT SILICONE. 69 | |
| FIGURE 4.11 THE MOLDING PROCESS OF THE PROPOSED SKIN SENSOR. | 70 |
| FIGURE 4.12 THE EXPERIMENT SETUP USED IN SNR AND ACCUMULATED LOAD TEST..... | 72 |
| FIGURE 4.13 THE EXPERIMENT SETUP FOR THE TEMPERATURE TEST. | 72 |
| FIGURE 4.14 THE EXPERIMENT SETUP OF THE TRIAXIAL FORCE TEST. | 73 |
| FIGURE 4.15 THE RESPONSE OF S ₂ UNDER 250 G OF WEIGHT. | 75 |
| FIGURE 4.16 THE RESPONSE OF S ₃ TO THE LOAD OF 50 MG..... | 75 |
| FIGURE 4.17 THE RELATIONSHIP BETWEEN TIME AND SENSOR READOUT OF S ₃ DURING THE ACCUMULATED LOAD TEST BEFORE MOLDING..... | 77 |
| FIGURE 4.18 THE RELATIONSHIP BETWEEN THE LOAD AND SENSOR READOUT OF S ₃ BEFORE THE MOLDING AND ITS QUADRATIC APPROXIMATION LINE OF BOTH LOADING AND UNLOADING SEQUENCES..... | 77 |
| FIGURE 4.19 THE THERMAL DRIFT OF ALL SENSING UNITS BEFORE THE MOLDING INCLUDING TCP (GRAY, SCALED DOWN BY 50) ARE SHOWN TOGETHER WITH THE ACTUAL TEMPERATURE (PURPLE) SENSED BY THE TMP102 SENSOR. | 78 |

| | |
|--|----|
| FIGURE 4.20 THE SENSOR READOUT OF ALL FOUR TRANSDUCERS AFTER THE TEMPERATURE COMPENSATION (PRE-MOLD) | 79 |
| FIGURE 4.21 THE POST-MOLD STEP RESPONSE OF ALL SENSING ELEMENTS WHEN THE LOAD OF 250 G IS APPLIED TO S_2 | 80 |
| FIGURE 4.22 THE RELATIONSHIP BETWEEN TIME AND SENSOR READOUT OF S_3 DURING THE ACCUMULATED LOAD TEST AFTER MOLDING | 81 |
| FIGURE 4.23 THE RELATIONSHIP BETWEEN THE LOAD AND SENSOR READOUT OF S_3 AFTER THE MOLDING AND ITS QUADRATIC APPROXIMATION LINE OF BOTH LOADING AND UNLOADING SEQUENCES..... | 81 |
| FIGURE 4.24 THE THERMAL DRIFT OF ALL SENSING UNITS AFTER THE MOLDING INCLUDING TCP (GRAY, SCALED DOWN BY 5) ARE SHOWN TOGETHER WITH THE ACTUAL TEMPERATURE (PURPLE) SENSED BY THE TMP102 SENSOR..... | 82 |
| FIGURE 4.25 THE SENSOR READOUT OF ALL FOUR TRANSDUCERS AFTER THE TEMPERATURE COMPENSATION (POST-MOLD) | 83 |
| FIGURE 4.26 THE SENSOR READOUTS WHEN APPLYING A SHEAR FORCE IN DIFFERENT DIRECTIONS | 84 |
| FIGURE 4.27 THE COMPARISON BETWEEN THE SIZE OF THE SURROUNDING PAD OF THE FIRST AND THE SECOND VERSION | 87 |
| FIGURE 4.28 THE COMPARISON OF THE CuBe ₂ SUPPORT AREA OF THE FIRST AND SECOND VERSION | 87 |
| FIGURE 4.29 THE COMPARISON OF THE POSITION OF THE TRANSDUCERS BETWEEN THE FIRST AND THE SECOND PROTOTYPE | 88 |
| FIGURE 4.30 THE COMPARISON BETWEEN THE DESIGN OF THE FIRST AND THE SECOND VERSION | 89 |
| FIGURE 4.31 THE ACTUAL PCB OF THE SECOND VERSION | 89 |
| FIGURE 4.32 THE STENCILS USED IN THE PRODUCTION OF THE 2ND VERSION SENSOR | 90 |
| FIGURE 4.33 THE PCB SUPPORT BLOCKS | 91 |
| FIGURE 4.34 THE COMPONENTS USED IN APPLYING THE SOLDER PASTE ON THE 2ND VERSION PCB | 92 |

| | |
|---|-----|
| FIGURE 4.35 THE RESULT OF USING THE STENCIL TO REGULATE THE AMOUNT OF SOLDER AND CONTROL THE DESIRED LOCATION | 92 |
| FIGURE 4.36 THE VERTICAL VACUUM PICK-UP TOOL SETUP USED TO STEADILY PLACE THE COPPER BERYLLIUM PLATE ON THE PASTED PCB | 93 |
| FIGURE 4.37 THE RESULTANT PCB AFTER REFLOW SOLDERED. | 94 |
| FIGURE 4.38 THE DEGASSING EQUIPMENT..... | 94 |
| FIGURE 4.39 THE SECTION VIEW OF THE TRANSDUCER..... | 95 |
| FIGURE 4.40 THE CONDUCTIVE INK USED IN THIS VERSION OF THE SENSOR. | 96 |
| FIGURE 4.41 THE SENSOR'S PCB AFTER IT IS PAINTED WITH THE CONDUCTIVE INK AT THE PERIMETER OF THE CUBe ₂ PLATE. | 96 |
| FIGURE 4.42 THE SENSOR'S PCB AFTER IT IS PAINTED ON THE SIDE OF THE TRANSDUCERS. | 96 |
| FIGURE 4.43 THE METHOD OF USING A PROTRACTOR TO CONFIRM THE BENDING ANGLE OF ALL THE TRANSDUCERS..... | 97 |
| FIGURE 4.44 THE IMPROVED MOLD CONSISTS OF 2 PIECES: THE BASE AND THE COVER. | 98 |
| FIGURE 4.45 THE MOLDING PROCESS OF THE SECOND SKIN SENSOR..... | 99 |
| FIGURE 4.46 THE EXPERIMENTAL SETUP OF THE TRIAXIAL FORCE TEST. | 100 |
| FIGURE 4.47 THE ADJUSTABLE ANGLE STAGE FIXED AT 45 DEGREES WITH RESPECT TO THE X-Y STAGE SURFACE AND THE CORRESPONDING 45-DEGREE PUSH PLATE..... | 100 |
| FIGURE 4.48 THE LOCATION OF THE 4 FORCE SENSING UNITS AND THE AXES AND ORIGIN OF THE SKIN SENSOR ARE SHOWN..... | 101 |
| FIGURE 4.49 A 3D PRINTED PLASTIC BLOCK THAT ALLOWS THE SENSOR TO BE ALIGNED AT 45 DEGREES WITH RESPECT TO THE OUTER EDGE OF THE BLOCK | 101 |
| FIGURE 4.50 THE ADJUSTABLE ANGLE STAGE IS SET AT 15 DEGREES WITH RESPECT TO THE X-Y STAGE SURFACE AND THE CORRESPONDING 15-DEGREE PUSH PLATE..... | 102 |
| FIGURE 4.51 THE RESULT OF THE SENSOR CALIBRATION EXPERIMENT | 103 |
| FIGURE 4.52 THE RESULTANT FORCE SENSED BY ALL 4 UNITS WHEN BEING PUSHED WITH A NORMAL AND A SHEAR FORCE ACTING IN DIFFERENT DIRECTIONS..... | 104 |

FIGURE 4.53 THE COMPARISON BETWEEN THE CALCULATED FORCE VECTOR AND THE ACTUAL FORCE VECTOR WHEN NORMAL FORCE AND +X SHEAR FORCE IS APPLIED. 105

FIGURE 4.54 THE COMPARISON BETWEEN CALCULATED FORCE VECTOR AND THE ACTUAL FORCE VECTOR WHEN THE NORMAL FORCE AND +X+Y SHEAR FORCE IS APPLIED... 106

FIGURE 4.55 THE COMPARISON BETWEEN CALCULATED FORCE VECTOR AND THE ACTUAL FORCE VECTOR WHEN NORMAL FORCE AND +Y SHEAR FORCE IS APPLIED..... 107

LIST OF ABBREVIATIONS AND ACRONYMS

CuBe₂ Copper Beryllium: a kind of copper alloy which has high strength, good spring, and high electronics conductivity properties.

CDC Capacitance to Digital Converter

I2C Inter-Integrated Circuit: a multi-master, multi-slave, single-ended, serial communication. It can handle up to 125 devices with 4 wires.

PCB Printed Circuit Board

PSECR Pressure Sensitive Electric Conductive Rubber

PVDF Polyvinylidene Fluoride: a kind of thermoplastic material which has strong piezoelectricity; it is often used as a piezoelectric transducer.

TCP Temperature Compensation Pad: a capacitive sensor which is insensitive to pressure. It is used to monitor thermal drift effect which can be found in the capacitive sensing modality.

1 INTRODUCTION

1.1 Motivation

In humans, the sense of touch has been proven to be a crucial ability in many aspects such as object manipulation, object exploration, and response to external force ranging from light touch to strong impact and pain [1][2]. It may seem to be rather trivial for humans to achieve several forms of manipulations such as performing a dexterous/swift maneuver or a stable grasp, realizing and preventing slippage when grasping, or rolling or re-orienting an object in-hand. Tactile sensing plays a major role in achieving those manipulation skills. Inducing anesthesia to the hands of experimentees resulted in a difficulty in maintaining a stable grasp [3]. Awareness of the frictional condition of an object also helps in grasping it with just enough force while preventing damaging the object. By touching an object, several properties of the object including non-visible ones, such as its hardness, roughness, temperature, moisture, and shape, can be obtained. These properties are difficult or even impossible to gain through other sensing modalities [4]–[8]. Furthermore, the sensors provide important information for manipulation, exploration, and haptics [9]. They can be used for example for in-hand manipulation [10][11] or to identify objects even without visual information [12]. Tactile sensing can be used to actively explore surrounding environment and in-hand object which result in obtaining more information when comparing to passive touch [13][14].

From the safety point of view, tactile sensing can be used not only to prevent unintended damage to any grasped object, but also to protect humans from injuries (e.g. from holding a glass, or a sharp edge of a knife too strong). In the scenario where other senses cannot be used effectively such as in a completely dark room, humans use their hands and legs

to reach out in the direction they want to go in order to explore and sense if there is any object in the way to prevent collision with that object (e.g. a corner of a dining table, or a wall cabinet). In robots, the sense of touch is very crucial as in the same way as that for humans, or even more important since human safety is the utmost importance especially when they have a close interaction, sharing the same environment or co-exist [15]. Tactile sensors are used allow robots to sense and interact with the outer world effectively. It can allow both industrial and welfare robots to perform safe, robust, and reliable interaction with unknown and/or uncontrollable environments, and especially with humans. If the robot fails to sense a contact with human reliably and promptly enough, it could lead to serious injury of humans.

Additionally, the sense of touch contributes also to the development of self-awareness [1][2]. It is considered as an important part of the “body schema” which represents the posture of oneself in space, and the relative location of one’s limbs [16]. This sense of self is very important for a robot in order for it to interact intelligently and effectively with its environment. For an instance, when a robot, that has tactile sensors installed on its two hands, touch his hands together, the tactile sensors on both hands could allow the robot to realize that the two hands belong to it and it could use its hands to explore the environment. Furthermore, a robot in [17] use its sensors and joints information to constantly perform self-modelling so that it can continue its locomotion even when a part of its limb is lost.

Lastly, apart from being useful for the field of robotics, the tactile sensor can be used in many applications. It can be used not only in the robotics field but it also as a soft gripper in natural or fragile product handling, as knee joint pressure sensor or force-feedback minimal invasive surgery devices in the medical field, as brake pad and tire pressure monitoring system in automotive, as body pressure mapping use in ergonomic product design, and as force interface found in consumer electronics¹ [18].

Nevertheless, despite of how important tactile sensing is, compared to other sensory modalities such as vision, previously developed tactile sensors cannot satisfy all the requirements (which will be summarized later) and face several problems, which will be discussed in the following and which is evident by the lack of tactile sensors in most robots, even though many transduction techniques have been investigated and sensors

¹ www.pressureprofile.com, www.softroboticsinc.com

have been implemented since the 1970s [1][2][9][18]. The development of tactile sensor did not receive much attention mainly during 1980s due to its low demand from the manufacturing industrial departments. A few common problems of the available tactile sensors are that they are not mechanically compliant, lack of conformability, not robust enough to abrasion and impact, too big for achieving high spatial density sensing, or having the difficulty of routing the wires of many sensors. The latter two reasons are often overlooked but are the major problem in the practical scenario where there is only a limited space in robots. Besides the space for the transducers, the space for the readout circuit and the wires for a high number of spatially distributed sensor elements need to be taken into consideration as well because these units are often larger than the transducers [2][9]. Another common limitation of many distributed tactile sensors is that they can sense only normal forces; sensors that can sense and differentiate sheer forces are often too big for the integration into thin robot skin.

Tactile or force sensing for a robot can be divided into 2 major methods; direct and indirect force sensing. The external force can be sensed indirectly using force/torque sensor installed at joints. Nevertheless, only the summation of the forces/torques exerted on the joint can be measured. On the other hand, sensing external forces by using distributed tactile sensors installed on the cover of the robot as a skin can provide the most direct feedback. With this method, local information (force magnitude and direction) of each contact force can be extracted including the position of the contact, while it is not trivial for a 6-axis force/torque sensor installed at a robot's joint (or even impossible in the case of multiple contacts on one segment) [19].

Ideally, the skin should be soft in order to guarantee safe interaction of the robot with its surrounding, especially humans, and to assist in object manipulation where some error can be compensated by the softness. In order to achieve soft skin, compliant material (usually viscoelastic material such as silicone) needs to be integrated into the skin [15][20]. Placing the compliant layer above the sensors leads to a reduction of the sensitivity, spatial resolution and time response of the sensor. If the compliant material is part of the transducer as in [21], this usually leads to severe hysteresis in the sensor measurements. Therefore, ideally the compliant material is placed below the transducers and the transducers are placed as close as possible to the skin surface, which is beneficial for example for the sensitivity and a faster time response. However, in several sensors, the transducer is more rigid than the compliant material. Putting this rigid transducer directly at the outermost surface could lead to injury in human-robot interaction.

Therefore, this leads to a challenging decision of what would be the configuration that gives the sensor both compliance and sensitivity.

1.2 Background

1.2.1 Importance of tactile sensing

The sense of touch is an important ability not only for humans but also for robots [1][2]. Tactile sensing allows humans to perform swift and precise object manipulation, obtaining many properties of an object only through touch and exploring their surroundings effectively, for example. Without the sense of touch, humans cannot grasp an object robustly, even when looking at it [22]. Furthermore, humans can lose the control of their limbs completely when losing the sense of touch, and cannot walk or stand upright. In the same fashion, tactile sensing allows a robot to perform smooth, flexible, and/or dexterous manipulation [23]. Moreover, when it comes to human symbiotic robots that share their workspace with humans, the safety of humans becomes the most important issue.

1.2.2 Current state of tactile sensor development

Despite the rising in demand for the tactile sensor that can satisfy the aforementioned criteria, there is currently no compact digital tactile sensor that can measure tri-axial force while providing a thin, soft and flat-surfaced layer. Many sensors are too big to be integrated into thin skins. For the sensors that have been integrated into thin skins, one major limitation is that most of them measure only normal forces, not tangential forces [20][24]. Tangential forces are an important component of the interaction forces, and information about the tri-axial contact forces would make object manipulation and recognition tasks easier. For example, the weight of a grasped glass that is filled with water, the force that is being applied while using a hammer, or possibly the surface curvature of a grasped object could be evaluated. Measuring distributed force vectors directly at the impact sites could also lead to improved collision reaction and impedance control possibilities.

1.2.3 Existing tactile and force-torque sensors

There are many sensing principles which can be employed for tactile sensing [1][2]. Table 1.1 shows the summarized advantages and disadvantages of the different sensing principles in general. The discussion here will be focused mainly on sensors that are

capable of measuring shear forces and related capacitive sensors. For a more in-depth discussion of different transduction technologies and integration issues in robotic systems please refer to [25]–[27] and a more recent one in [28]. The importance of tactile sensing to robot manipulators can be found in [29]. More recently, an overview on tactile sensing in both human and humanoid was provided in [1]. Reviews on tactile sensing for human-robot interaction were provided in [30] and [31].

Table 1.1 General comparison between different transducing technologies.

| Sensing Principle | Advantage | Disadvantage |
|-------------------|--|--|
| Piezoelectric | <ul style="list-style-type: none"> • High sensitivity • Dynamic sensing • Slip detection | <ul style="list-style-type: none"> • Thermal sensitive |
| Optical | <ul style="list-style-type: none"> • Immune to electromagnetic • Flexible • Sensitive • Fast | <ul style="list-style-type: none"> • Often large size • Need of light source and light receiver |
| Hall Effect | <ul style="list-style-type: none"> • Small 3D chip available • Simple construction | <ul style="list-style-type: none"> • Significantly interfered by another magnetic source |
| Piezoresistive | <ul style="list-style-type: none"> • Linear • Robust | <ul style="list-style-type: none"> • Amplified noise • Thermal sensitive • Power consumption |
| Capacitive | <ul style="list-style-type: none"> • Small CDC chip available • Good sensitivity • Wide dynamic range • Robust | <ul style="list-style-type: none"> • Stray capacity • Severe hysteresis (due to the use of viscoelastic material) • Thermal sensitive |
| MEMS | <ul style="list-style-type: none"> • Small in size • Excellent sensitivity | <ul style="list-style-type: none"> • Fragile • Small measurement range • Complicated production • Production inconsistency |

1.2.3.1 Piezoelectric-based sensors

In general, piezoelectric sensors can detect changes in force; a single piezoelectric sensor embedded in a soft substrate can detect changes in normal as well as in shear forces, but

cannot distinguish them. Piezoelectric sensors based on polyvinylidene fluoride (PVDF) have been incorporated into several robotic hands [32]–[35], and can be used for example to detect slippage. The body of the CB2 humanoid robot [36] is covered with 197 sensors based on PVDF films which are put between a layer of a soft silicone outer skin and inner urethane foam. The sensor detects the rate of change of its bending; the readout of all sensors can be done with 100 Hz. Nevertheless, only few information about the performance of the sensor is available. In [34][35] the piezoelectric sensors were embedded in the soft skin, but in none of the aforementioned implementations the force vector (the direction of applied force) can be measured. Furthermore, a company named Touchence² sells a thin, small-sized 3-axis tactile sensor based on MEMS piezoelectric elements, but the sensor is rigid and the necessary electronics are bigger than the sensor itself. Illustrations of some of the aforementioned sensor can be seen in Figure 1.1.

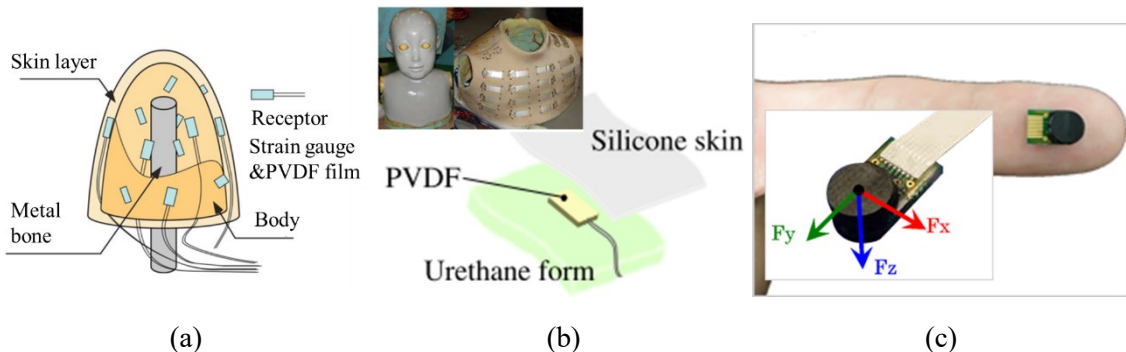


Figure 1.1 An example of existing piezoelectric-based sensors. (a) Randomly placed PVDF tactile sensor. (b) PVDF tactile sensors installed on the whole body of CB2. (c) 3-axis piezoelectric MEMS sensors by Touchence Company. The pictures are taken from [35][36] and www.touchence.jp respectively.

1.2.3.2 Optical-based sensors

Many optical sensors that can measure shear forces are too big to be integrated into the skin which is only several millimeters thick, as they need a camera to look at the skin, for example [37][38]. A small-sized optical sensor that can measure both normal and shear forces was already proposed more than 10 years ago in [39], but to the best of the author's knowledge has not been integrated into a robotic system yet. Cubic soft optical 3-axis sensors have also been integrated into a $20 \times 20 \times 20 \text{ mm}^3$ light-weight polyurethane foam in [40]. Similar sensors have recently been made commercially available by Touchence. These sensors, however, are rather thick which could drastically increase the overall size

² www.touchence.jp

of the robot when they are used as a soft skin. The highly sensitive 3-axis distributed sensors in [41] were designed as a robotic fingertip with the size of 42.6 mm-high and 27 mm-wide. It consists of rigid conical sensing elements installed on a dome-shaped aluminum base and a soft rubber outer cover. However, due to the non-uniform thickness of the cover silicone it could lead to some challenging in controlling contact force. A 10 mm-wide and 8 mm-high optical sensor that can measure the force vector is currently available from OptoForce³. However, an additional analog-to-digital (ADC) unit which has a bigger size comparing to the sensor is required for each sensor. Images of some existing sensors based on optical technology can be found in Figure 1.2.

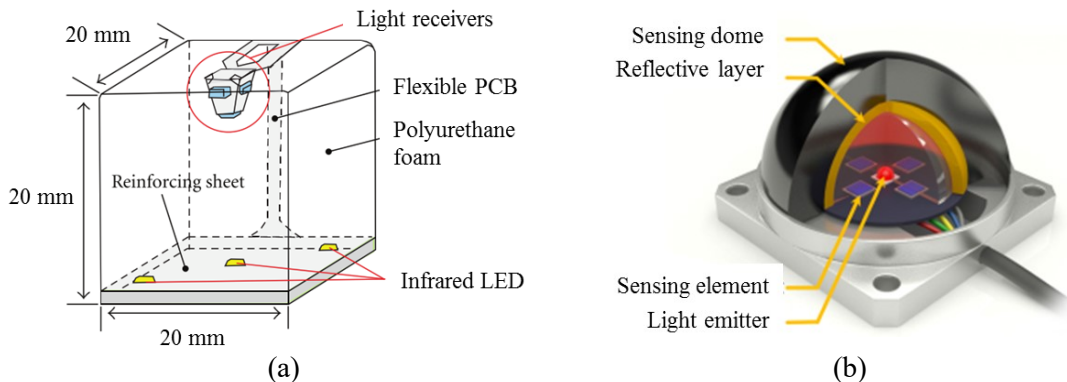


Figure 1.2 An example of existing optical-based tactile sensors. (a) 3-axis soft sensor flesh. (b) 3-axis dome-shaped sensor from Optoforce Company. The pictures are taken from [40], and optoforce.com respectively.

1.2.3.3 Hall Effect-based sensors

Hall Effect sensor and magnet can also be used together for tactile sensing. A 1-axis soft sensor for robotic fingertips and phalanges was recently integrated on a robot hand for classifying several kinds of objects [42]. An extended study on the characteristic of the sensor was published in [43]; the sensor provides high sensitivity because of an extra layer of air to increase the deformability. Furthermore, the studies in [44][45] proposed a 3-axis sensor made of dome-shaped silicone rubber; it consists of a magnet in the top of the dome and 4 Hall Effect sensors located at the base of the dome. The sensor was installed on various parts of several robots such as Obrero. The sensor prototype in [46] instead introduced the use of a single chip that can measure a magnetic field in 3 dimensions. However, only preliminary experiments on one sensor were performed and

³ optoforce.com

no integration on a robot is reported. Figures of some sensors based on Hall Effect can be found in Figure 1.3.

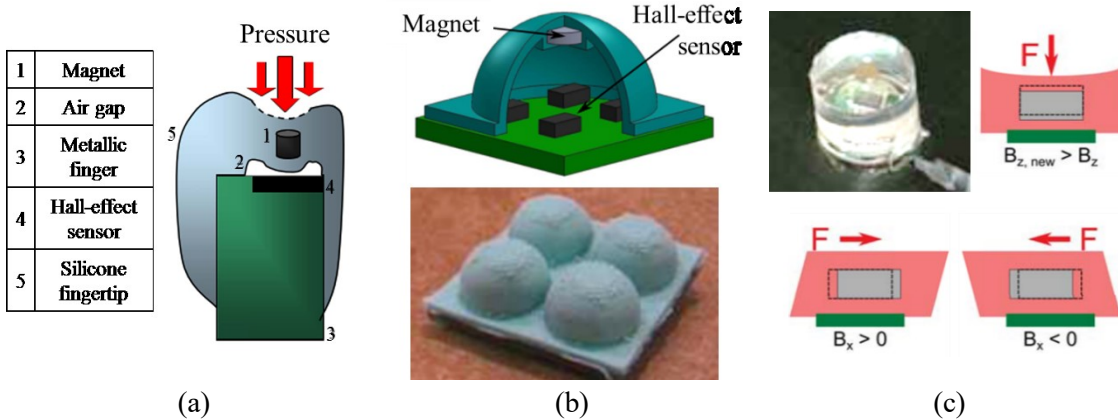


Figure 1.3 An example of existing Hall Effect-based sensors. (a) 1-axis sensor with an air gap. (b) 3-axis dome-shaped sensor. (c) 3-axis sensor prototype with a flat surface. The pictures are taken from [43][45], and [46] respectively.

1.2.3.4 PSECR-based sensors

Furthermore, in [47] a dome-shaped sensor based on pressure-sensitive electric conductive rubber (PSECR) and pectinate circuit design is described. The resistivity of the pectinate circuit changes when a pressure applies to the sensor's top. The sensor prototype is 10 mm in diameter. In general, a dome-like structure can assist in sensing the shear forces; however, the size of the dome is the determinant of the smallest size of its detectable object. Additionally, a smooth skin surface is preferable in many applications. Figure 1.4 shows some example of the sensors mentioned in this section.

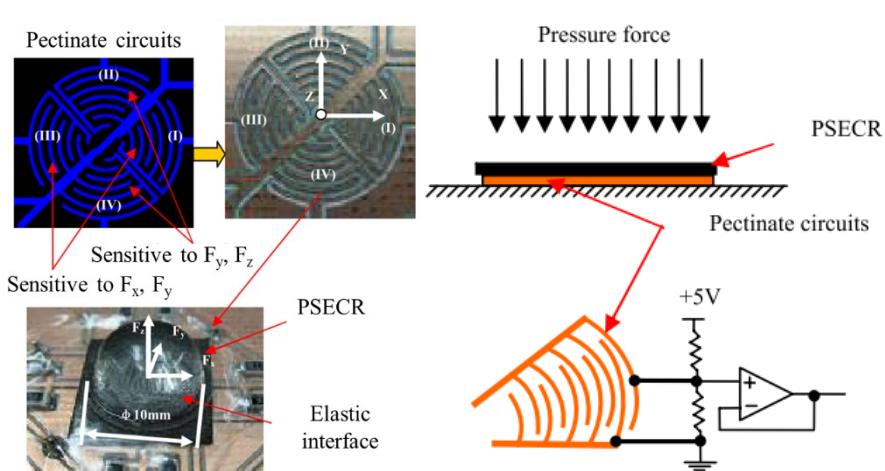


Figure 1.4 An example of existing sensors based on pressure-sensitive electric conductive rubber (PSECR). Its dome shape enhanced 3-axis force measurement. The pictures are taken from [47].

1.2.3.5 Piezoresistive-based sensors

Several sensors that can measure 3-axis or even 6-axis F/T are based on piezoresistive or strain gauges, but many are too big to be embedded in a relatively thin skin. In the WENDY robot [48], a 6-axis force-torque sensor and force-sensitive resistor (FSR) pads were integrated into a box-type structure enveloping a robot link such as its forearm. Similarly, the MAC hand used a $10 \times 7.5 \times 5.5 \text{ mm}^3$ 3-axis joystick which is connected to a rigid hollow cover to detect contact forces. Additional electronics are integrated inside each finger link as well for the digitization of the sensor [49][50]. Each soft and curved fingertip of TWENDY-ONE [15] installed a 6-axis force/torque sensor and 241 distributed sheet-type tactile sensing elements which cover the inside of the hand and fingers. They allow the robot to pick up and manipulate small objects. However, the necessary ADC units were installed on the back of each hand. The Robonaut 2 hand [51][52] used a specially-designed 6-axis force/torque sensor with miniature strain gauges itself as a phalange resulting in a compact robotic hand. The ADC unit of the sensors, however, was located in the palm of each hand. The aforementioned sensors are not compliant and most require remotely installed digitization electronics which could lead to a susceptibility to noise. More importantly, only the summation of all the forces acting on the link can be sensed. The DLR-HIT hand [53], however, has each fingertip installed with a $16 \times 20 \text{ mm}^2$ compact cylindrical 6-axis sensor. It provides digital output directly but it is not commercially available. Nevertheless, an implementation of 4 tri-axial sensors in a robotic fingertip is presented in [54].

Moreover, 3-axis F/T sensors were integrated into the soft skin of the robot Macra; the sensors are covered by a relatively thick layer of polyurethane foam [40]. Recently, a small-sized sensor based on piezoresistive beams is described in [55]. The $2.0 \times 2.0 \times 0.3 \text{ mm}^3$ sensor was fabricated and embedded in polydimethylsiloxane (PDMS) sheet. The test result showed the crossover of sensor readout when subjected to normal stress but the thermal drift was reduced significantly comparing to typical piezoresistor. The work in [56] and its extended work in [57] proposed a concept to sense two-directional shear forces using vertical beams suspending in an elastic material with an additional liquid layer in the later work. Only a shear force perpendicular to the bending axis is sent by the piezoresistor installed at the bending part of each beam. However, the sensor cannot measure normal force and limited shear force was only approximately 0.02 N. Due to its vertical beam configuration, it could be prone to damage when a pure normal force acting directly on the beam. The sensor fabrication is rather complicated; a magnetic field was

used to bend each beam up, and PDMS was used to cover the beams. Moreover, the ADC unit is not mentioned in these works [55]–[57]. Also, small-sized ADC converting chips for strain gauges are currently not available, hence, additional space would be necessary for containing the digitization electronics. Pictures of the aforementioned piezoresistive based sensors are shown in Figure 1.5.

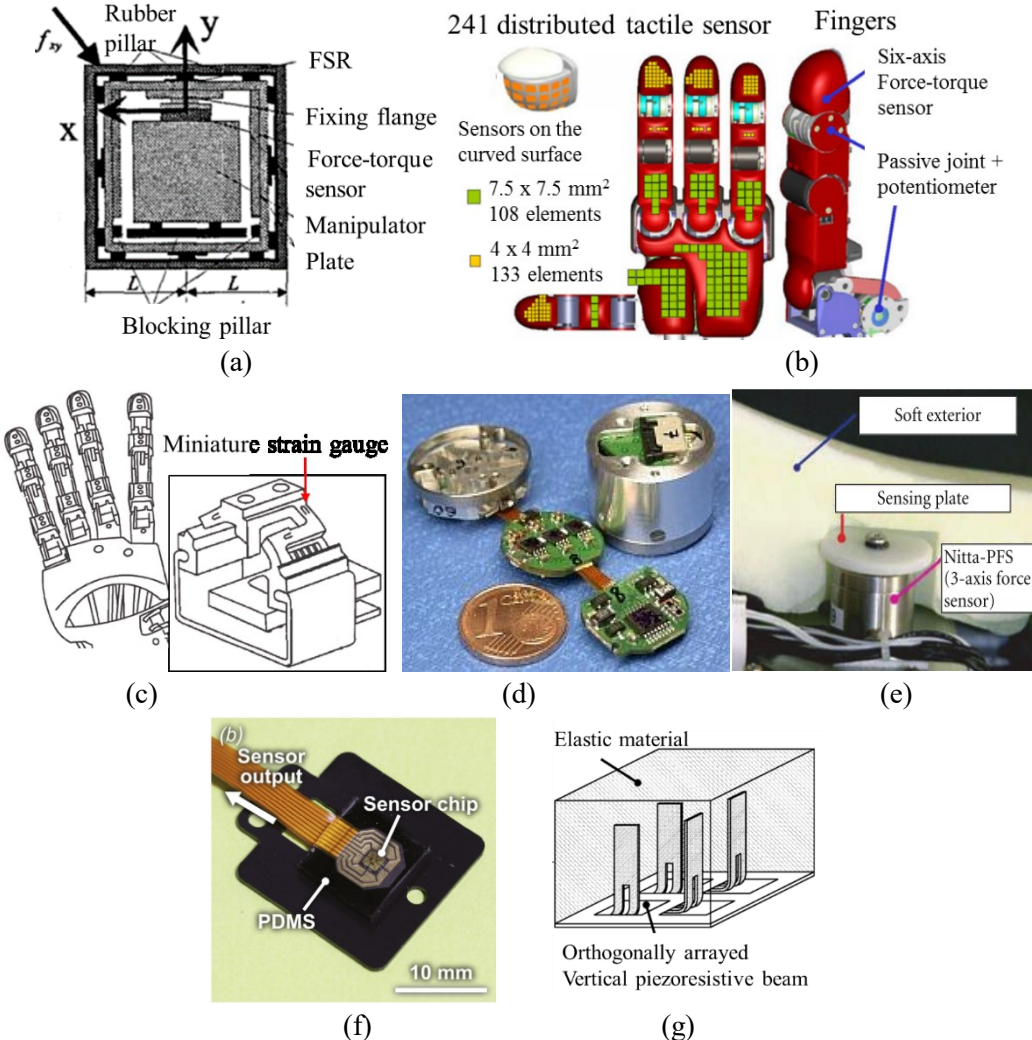


Figure 1.5 An example of existing piezoresistive-based sensors. (a) 6-axis force/torque sensor and the hard shell. (b) TWENDY’s fingertip with 6-axis force/torque sensor. (c) Integrated 6-axis force/torque sensor used in Robonaut 2. (d) Small digital 6-axis force/torque sensor used in DLR-HIT hand. (e) 3-axis force sensor with soft skin installed on Macra. (f) Small and thin 3-axis sensor. (g) A shear force sensor using vertical piezoresistive beams. The pictures are taken from [48], [15], [52], [53], [40], [55], and [56], respectively.

1.2.3.6 Capacitive-based sensors

Capacitive sensors have preferential sensor characteristics such as high sensitivity, yet they often have severe hysteresis and thermal drift [1]. In [58][59] a bump was added on

top of an array of four capacitive sensors to allow the shear forces measurement but both sensors can sense only millinewtons force which is too little for humanoid robots application. Flexible capacitive sensors that can measure the shear forces without a bump were suggested in [60][61]; there were four capacitors which share one common and a bigger electrode on the top. However, the measurements electronics were not included, therefore, the integration into a large-scale skin is not straightforward.

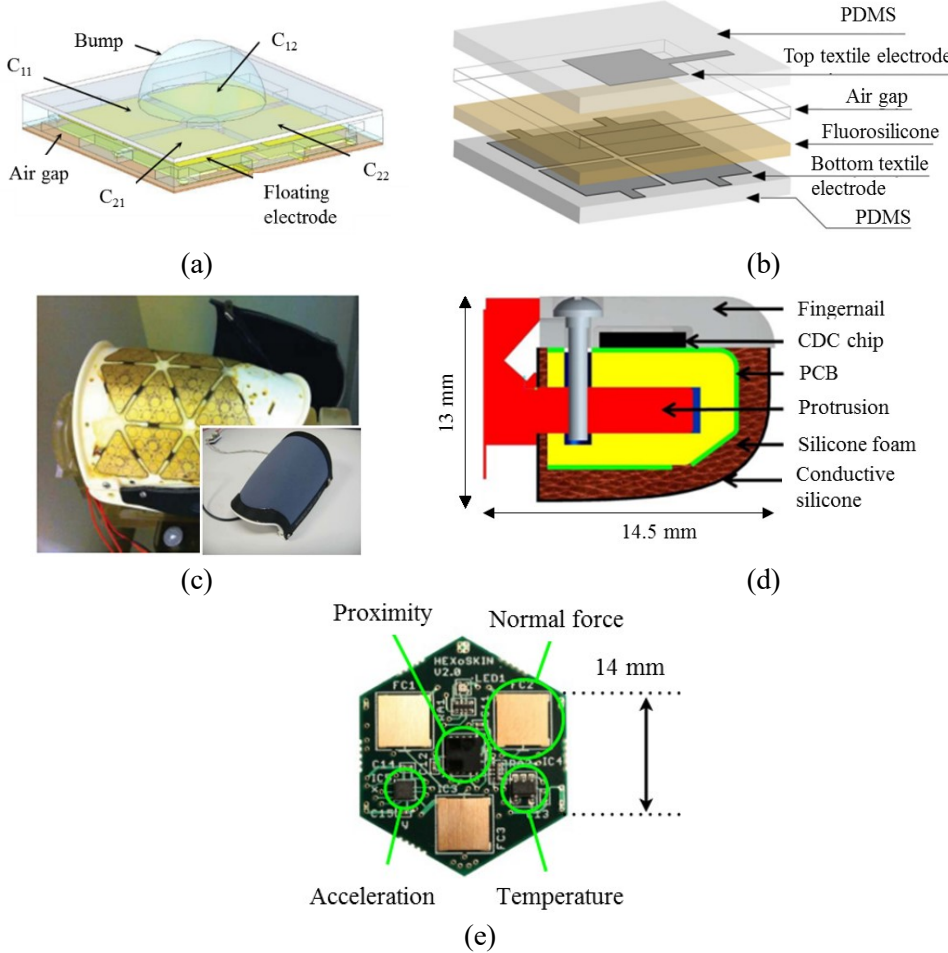


Figure 1.6 An example of existing capacitive-based sensors. (a) 3-axis small-sized sensors utilizing bump to detect force vector. (b) 3-axis small sized sensors using no bump to detect force vector. (c), (d) 1-axis flexible tactile sensors installed on iCub robot. (e) Multimodal Hex-O-Skin including 1-axis force sensor using CuBe₂. The pictures are taken from [58], [60], [7], [9], and [24], respectively.

CDC chips, such as the AD7147 from Analog Devices, became available recently [62]. This chip enables digitization of capacitance in very limited space and has been previously used for flexible robotic skin sensing [20][21]. The hysteresis was present in both sensors due to the soft dielectric used. A pressure-insensitive capacitor was used in [20] to countermeasure the thermal drift. Time-dependent behavior of the silicone used in [21] was taken into account by modeling the relaxation of the material. A capacitive-

type force sensor that uses copper beryllium (CuBe_2) plates was firstly implemented in [24] as a part of multi-modal skin sensor; it can also sense proximity, temperature, and its own orientation. There were 4 connection ports to reduce the total amount of necessary wires. Nevertheless, the sensors in [20][21][24] can measure only normal force while the current thesis aims to measure also the tangential forces. Furthermore, compared to [24], the shape of the CuBe_2 plates was changed to foster a parallel deformation [63], and in [24] the sensors are embedded in a rather hard casing while the sensors described in this thesis are embedded in soft silicone. Figure 1.6 shows some example of previously mentioned capacitive-type tactile sensors.

1.2.3.7 MEMS-based sensors

MEMS-based sensors are another ongoing research area. They can detect force at a very tiny magnitude of 1 mN or less. However, the drawback of MEMS sensors is that they are fragile and easy to break if overload force is applied to them [24][64], which make them not suitable for integration into a robotic fingertip or hand.

1.2.3.8 Proximity detection

Instead of force sensors, some research such as in [65][66] focus instead on proximity detection of obstacles with 500 pairs of infrared light emitting diodes (IRED) and light receiving PIN diodes, to cover an industrial robotic arm to allow it to work in an unknown environment. The multi-modal skin sensor in [24] also included proximity detection module into each sensor. Proximity sensing has the benefit that it can detect collisions before they occur, but self-sensing and sensing of nearby but not colliding objects has to be taken into account.

1.3 Aims and Objectives

The goal of this research is to develop a tri-axial distributed skin sensor which is not only sensitive but also compliant. Moreover, the design of the sensor was done with taking into consideration the features that benefit the practical use of the sensor such as local digitization, and reduction of required wires. The process of the development was divided into the development of two main prototypes. The first version was aimed to initially test several basic features of the sensor; it has high signal-to-noise ratio (SNR), low hysteresis, temperature compensation, low nonlinearity, high sensitivity, and broad measurement range (from a few grams to kilograms). The final version of the skin sensor focused on achieving the tri-axial force measurement while providing compliance property. This is

accomplished with a novel arrangement of the force transducers developed in the first prototype. The skin sensor was aimed to use as a robotic skin which can be installed on several parts of a robot. This soft sensor installed on a robotic hand could provide not only detailed information about an object inside the hand but also the safe interaction with human and objects. The provision of local contact force vector from the skin installed on an arm could potentially assist in counteracting an impact force effectively.

The features which taken into consideration to improve the practical usage of the sensor will not only make the installation of the sensor itself easier but also that of its related electronic component and wires because there is only a limited space in arm and hand of the robot. Local digitization circuit can reduce the susceptibility of analog signal's noise. Serial communication such as I2C bus can be used to reduce the amount of digital wires required by allowing multiple sensors to share the same data line.

1.4 Novel Contribution

As mentioned previously that despite many tactile sensors have been developed, there is currently no compact digital tactile sensor that can measure tri-axial force while providing a thin, soft and flat-surfaced layer. Most existing sensors can measure only 1-axis of force, are not compliant, or are too big to be installed on robots where only limited space is available. Therefore, the thesis seeks to fill the gap by developing a sensor with such characteristics. Having the ability to provide digital output directly from a sensor can not only reduce the susceptibility to noise but also could significantly reduce the amount of required wires needed for using many sensors as an array of skin sensors. Some sensors such as ones found from optoforce, [45][47][58][59] used protruded bump to solve the tri-axial force measurement problems but the size of the dome can limit the size of the detectable object. Additionally, in most cases, the sensors with a smooth surface are more preferable. Some sensors proposed tri-axial tactile sensors with a flat surface such as in Touchence's ShokacChip and ShokacCube, [14][40][52][53][55]. However, they are rigid, too thick, require additional electronics which is relatively bigger than their transducers, or have only a few information about the sensors' characteristics available.

This thesis proposes a novel arrangement of the transducers which allows the sensor to measure tri-axial force (more detail is presented in Chapter 4). The proposed skin sensor has four capacitive-type force sensing transducers tilting in four different directions and suspended in a soft material, in particular, silicone rubber. The way a group of transducers is being aligned in a sensor can determine how effective and how many degrees of

freedom of force the sensor can measure. Even the same transducers are used, but with two different alignments, the two sensors can measure the same force differently, one might only able to sense just 1-axis component of that force, while the other could measure all 3 components of the force. Moreover, by combining the novel proposed transducers' alignment with flexible and compliant materials, namely, the flexible PCB (which the transducers are mounted to) and the soft silicone rubber, the developed sensor can be both compliant and sensitive at the same time. This is because the tilted transducers are located close to the sensor surface where the interaction with external force occur, and the silicone and the flexible PCB allow the tilting angle of the transducers to change temporarily corresponding to the applied force acting of the sensor's surface. Hence, the compliance of the sensor is not compromised by the fact that the transducers are tilted so that they can be close to the sensor's surface.

Another contribution lies in the introducing of the improved shape of copper beryllium plate used in the capacitive-type force transducers presented in this thesis (please refer to Chapter 2 for more detail). This improved design can increase both the sensitivity and the measurement range of the sensor by allowing the plate to elastically deform in a more uniform and more parallel fashion. The copper beryllium plate used in this thesis has a thick bump on top of a thin plate which is produced as one piece by the lithographic etching process. Comparing to a thin plate, the thick bump in the center of the plate prevent the inverted bell-shaped deformation where the maximum deformation distance is at the center. With the same initial gap between two parallel copper plates, if the top plate is a normal thin plate, the top plate will be in contact with the lower plate with less force acting on the center of the top plate comparing to when the top plate is a thin plate with a thick bump. Moreover, since the deformation of the normal thin plate is the inverted bell shape, only the small area at the center of the plate affect the overall capacitance, hence only a small capacitance change is achieved. On the other hand, in the case of using the copper plate with a bump in the center of the plate, more uniform deformation allows more area of the plate to move down resulting in a more change in the capacitance. Furthermore, the more capacitance change can be easily differentiated from noise while the subtle change in the capacitance due to the external force is difficult to differentiate. Therefore, the sensor can be more sensitive and have an increased range of measurement with the using of the copper plate with a thick bump.

Lastly, this thesis also proposes a new application of using the developed sensor with magnetorheological (MR) fluid to create an adjustable stiffness haptic device to exploit

the benefit of MR fluid characteristic in changing its apparent viscosity according to the magnetic field. The haptic device is made from a soft rubber pouch filled with MR fluid with the distributed tactile sensor installed underneath the pouch. By touching the pouch, users can feel the changing in the stiffness of the pouch which can be varied from liquid-like soft to stiff. This variable stiffness can be programmed to respond to a virtual reality software to simulate the stiffness of an object inside that virtual world, for example. The sensor is used to detect both the magnitude of the force exerted by a user and its position. It is discovered that the tactile sensor was fully functional even in the presence of a magnetic field; the good characteristics of the sensor are preserved. The adjustable stiffness had only minor effect on the transient and steady-state responses of the sensor. Only small crosstalk was recognized even at the stiff state of the MR fluid. Moreover, it was found that the MR fluid can provide another feedback to users in the form of adjustable vibration. The vibration can be achieved by changing the direction of the magnetic field and the frequency of the vibration can be controlled by the frequency of the switching magnetic field. Hence, the developed haptic device can provide users with two dimensions of feedbacks, the adjustable stiffness, and the adjustable vibration.

1.5 Thesis Outline

This section provides the organization of the rest of this thesis with a brief detail of the content inside each chapter.

1.5.1 Chapter 2

In this chapter, the first prototype of the capacitive-type tactile sensor is presented. The prototype is based on a simple construction in order to first test the feasibility and the performance of the proposed concept. The new design of a copper beryllium plate with a bump is shown with its result of the finite element simulation which presents the improvement over the design used in the previous literature. The criterion for designing capacitive sensors is also discussed. Lastly, the construction of the sensor and the experiments of the sensor are explained. The sensor has high signal-to-noise ratio, small hysteresis, and is able to compensate the effect of thermal variation. The digital readout can be acquired directly from the sensor via I2C bus.

1.5.2 Chapter 3

In Chapter 3, an application of utilizing the sensor developed in the previous chapter is discussed. A haptic interface with adjustable stiffness using MR fluid and incorporating

the tactile sensor is proposed. A prototype of the device was constructed and its performances were tested. The results showed that the device can provide several level of stiffness as a feedback to a user who is touching the device. On the other hand, the device can sense the user's contact force and position using the developed tactile sensor with only slight reduction in time response and magnitude. It can also be found that the capacitive sensor can be used without any interference from the adjacent electromagnet. Interestingly, the device can provide also another dimension of feedback in the form of variable vibration through the switching of the direction of the input current of the electromagnet.

1.5.3 Chapter 4

In this chapter, the work done in chapter 2 is further developed in order to achieve the main objective of this thesis which is to develop a soft, flexible, and sensitive tri-axial skin sensor. The novel arrangement of four transducers allows the sensor to measure the force vector is proposed and realized. The arrangement also allows the sensor to be soft and sensitive at the same time. Several techniques including double-sided transducers are used in order to further enhance the performance of the sensor. Lastly, the sensor is evaluated with various tests, especially the tri-axial test which showed that the proposed concept can successfully measure the force vector acting on the top flat surface of the sensor. The hysteresis of the sensor is only 3%, and the temperature compensation can reduce the susceptibility to temperature by approximately 80%.

1.5.4 Chapter 5

In this last chapter, the conclusion of this thesis is presented. It consists of the summary of the work presented in Chapter 2 to 4. The key features of the developed three-axis soft skin sensor are then noted. Although the sensor can successfully measure the tri-axial force vector, there is still room for improvement in several perspectives. These improvements are discussed in future work.

2 CAPACITIVE-TYPE FORCE TRANSDUCER WITH A BUMP

In this chapter, the capacitive-type force transducer with a bump on the transducer top is introduced. Firstly, the concept of the sensor is explained and followed by the implementation of the sensor. The finite element analysis (FEA) of the bump showed that the thick bump on a thin plate made of copper beryllium provides a more uniform deformation of the plate which leads to a more sensitive response. The copper beryllium alloy was selected due to its superior spring property, high strength, and high conductivity. The sensor used a local digitization chip which provides digital I2C output; up to 4 of the sensors can share the same data line. Experiments were performed to test several characteristics of the developed sensor. The result showed that the sensor has high sensitivity, high SNR, and only small hysteresis. The temperature compensation pad can attenuate the effect of thermal variation on the sensor's readout.

2.1 Concept

The capacitive-type force transducer proposed in this chapter employed the principle of a parallel capacitor where the capacitance between two electrode plates can be calculated from Eq. 1.

$$C = \epsilon_r \epsilon_0 \frac{A}{d} \quad (1)$$

Where

C is the capacitance (F)

ϵ_r is the relative static permittivity (unitless)

ϵ_0 is the electric constant (F/m)

A is the overlap area of the two electrode plates (m^2)

d is the relative distance between the two electrode plates (m)

It can be seen that if there is an external force which leads to a change in the relative distance between the two electrode plates, the magnitude of the force can be detected as the capacitance changes accordingly.

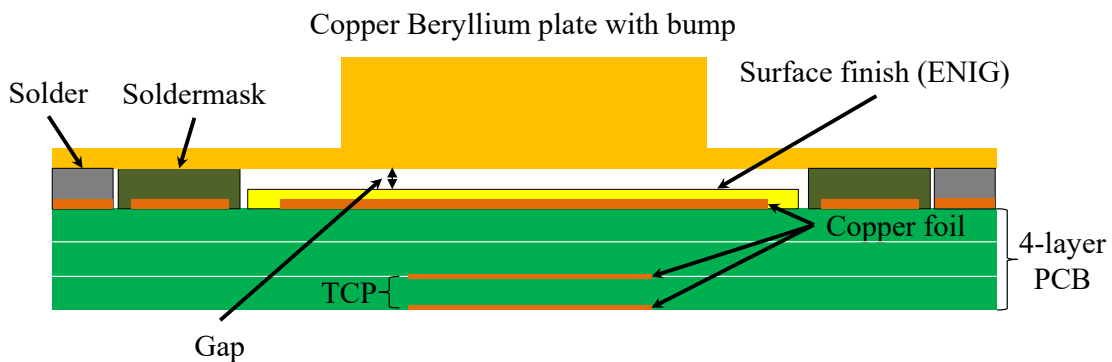


Figure 2.1 Side view of a single force sensing unit. The copper beryllium plate rests on the solder mask layer of the PCB. The gap is according to the difference in thickness between the solder mask and the surface finish (ENIG) layer.

The diagram of the capacitive-type force transducer proposed in this chapter can be seen in Figure 2.1. It is composed of a coated copper foil, which is part of the PCB itself, and a copper beryllium plate above the copper foil, to act as a pair of capacitor plates. The technique of implementing a CuBe₂ plate as a capacitor plate was inspired by the force sensing unit of a multimodal artificial skin presented in [24]. However, the implementation of the plate has been changed by having a bump as a part of the plate itself; several advantages of the bump will be discussed in Section 4.2.2. When force is applied on the plate, a deformation occurs causing the relative distance between the plates to decrease, thereby resulting in a change in capacitance which can be sensed by an electronic circuit. A layer of non-conductive soldermask which is commonly found in PCBs is used to control the initial gap between the CuBe₂ plate and the copper foil and to provide a support for the copper plate to rest on as well. One well-known disadvantage of any capacitive sensor is that it is susceptible to thermal change. To counteract this

phenomenon, a pressure-insensitive capacitor which firstly introduced in [20] is included in the sensor as well.

It can be seen that the concept required only two main components which are the copper beryllium plate and the PCB. The next section will discuss the realization of this concept.

2.2 Implementation

The concept of the force transducer was explained in the previous section. The detailed explanation will be provided here by focusing more on technical detail of how the sensor was produced.

2.2.1 Digitization of the Capacitance

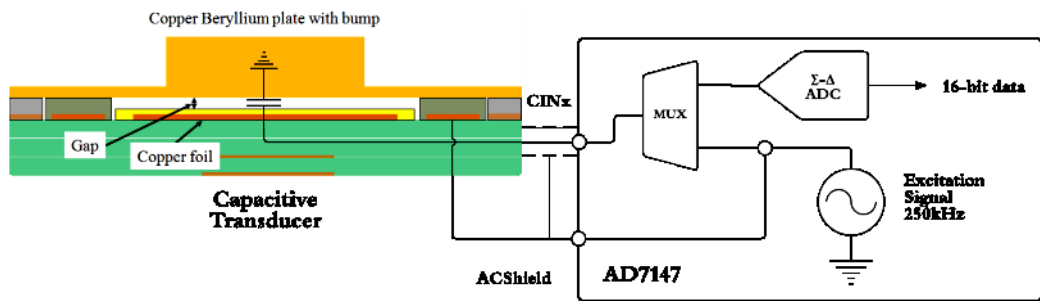


Figure 2.2 Capacitance measurement using AD7147. The sensor's electrode (not grounded) is charged and discharged by the excitation signal; the response of the same electrode is then converted into 16-bit data. The AC Shield is also excited with the same signal simultaneously to minimize stray capacitance and noise coupling. The figure is reconstructed based on that in [62].

To minimize the interference of electronic noise and distortion, it is preferential that the length of the analog signal (or in this context, capacitance signal) trace should be as short as possible. Therefore, the digitization module should be close to the capacitive transducer. Since a $4 \times 4 \text{ mm}^2$ capacitance-to-digital converter (CDC) chip AD7147 has been made commercially available by Analog Devices [62], it is more straightforward to realize the local digitization module. Each AD7147 can measure and convert the capacitances of up to twelve capacitors into digital signals and send them over I₂C bus to any I₂C-compatible master microcontroller. By using the I₂C bus, up to four AD7147 chips can share the same data line thereby drastically reducing the amount of necessary wires.

To measure the capacitance of a capacitive sensor with respect to ground, the AD7147 will alternately charge the capacitive electrode with the excitation signal and convert its response into 16-bit data at 250 kHz sampling frequency (see Figure 2.2). The output from each conversion stage is calculated from the averaging of several samples which can be customized to either 192, 384 or 768 samples per conversion. This decimation process is to reduce the amount of noise of CDC result; the more the samples per conversion, the less the noise is, but indeed the longer the conversion time is as well.

Moreover, in order to minimize stray capacitance to ground of the sensor and noise coupling, the PCB circuit was designed according to [67]. As a result, we use a 4-layered PCB and the AC shield function of the chip is used to shield all analog signals (capacitance measurement in this case) from all digital signals. In particular, the ACShield output is used to surround the sensor's electrode and its trace (as seen in Figure 2.2) both at the side of the top layer and at the second layer underneath. The ACShield is excited by the same signal use in the capacitance measurement, hence, there will be no potential difference (i.e. no capacitance) between the shield and the sensor.

2.2.2 Temperature Compensation Pad

As briefly discussed in Section 4.1 capacitive sensors are susceptible to thermal change. Therefore, in order to sense the influence of temperature on the sensor, a pair of copper foils is put in the third and the bottom layer to create a pressure-insensitive capacitor called Temperature Compensation Pad (TCP) as can be seen in the lower part of Figure 2.1. Its capacitance changes only according to temperature. With the measurements from the TCP, the effect of temperature on the force measurement can be compensated, as it has been done in [20]: temperature compensation can be achieved by adding to the force measurement the change in TCP multiplied by a certain gain. The validity of this approach will be evaluated in Section 4.3.1.

2.2.3 The Sensor

The 4-layer PCB was designed and produced according to the aforementioned concept and the design recommendation of the AD7147 chip [67]. The PCB can be seen in Figure 2.3(a). On the top layer; three circular copper electrodes are surrounded by the light green soldermask. The soldermask is used to support the CuBe₂ plate and to create a gap between the plate and the circular electrode as explained earlier in Section 2.1 and shown in Figure 2.1. To protect the electrode pad from oxidation, a surface finishing typically

found in PCB manufacturing called Electroless Nickel Immersion Gold (ENIG) is used. The ENIG was selected because of its smooth and very thin layer of coating of only approximately 5 microns. As a result, the gap between the capacitive plates can be maintained at around 10 microns according to the PCB manufacturer, which was confirmed with the measurement of SurfCoder SE-3400 of Kosaka Lab (see Figure 2.4).

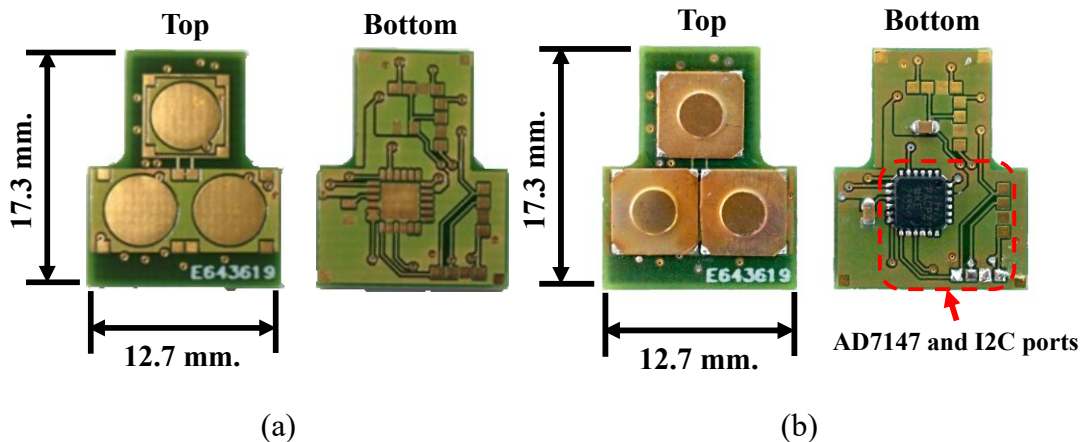


Figure 2.3 The capacitive force sensor. (a) The top and bottom side of an empty PCB. (b) The top and bottom side of the PCB after all of the components are mounted; the force sensing units, the AD7147 CDC chip, and the I2C port can be seen.

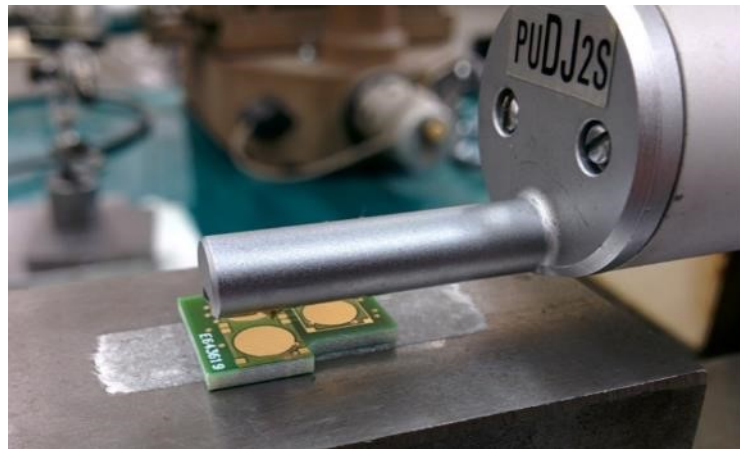


Figure 2.4 The confirmation of the capacitor's gap. The surface roughness measuring machine, Kosaka's Lab SurfCoder SE-34000 was used; the height difference between the soldermask top and the copper pad of approximately 10 microns was observed.

Additionally, the copper foil under the soldermask (top layer) and that in the second layer are connected to ACShield. This provides a protection to the analog signals from the interference of the digital signal located in the third and the bottom layer and to minimize stray capacitance. Since the CDC chip will be mounted on the bottom side of the PCB, the ACShield is also used to separate the analog traces from the digital traces as well.

Finally, as can be seen in Figure 2.3(b), three copper beryllium plates are manually soldered onto the top side of the PCB at four rectangular copper pads located around each of the circular electrode pads. The lead-free no-clean solder paste SMD291SNL from Chip Quik Company was used and it was melted at around 250 °C to the copper plate and the four pads by a hot air gun. This solder paste was selected because the included solder flux is not corrosive, hence cleaning it after soldering is not necessary; this is important because cleaning the remaining flux under the copper beryllium plate is not possible. The detail about the dimension and the shape of the copper beryllium will be discussed in the next section. The AD7147 and two ceramic capacitors (as a requirement of using AD7147) were soldered on the bottom side.

Table 2.1 The properties of copper beryllium CW101C R580 (Alloy 25 1/2H, C17200 TD02)

| Properties | Unit | Value | Specification | |
|-----------------------------|-------------------|--------------|----------------------|------------|
| | | | Min | Max |
| Density | g/cm ³ | 8.30 | - | - |
| Melting Point | °C | 870 | - | - |
| Electrical Conductivity | μΩ-cm | - | 6.2 | 7.8 |
| Elastic Modulus | GPa | 131 | - | - |
| Poison Ratio | - | 0.3 | - | - |
| Tensile strength | N/mm ² | 621 | 586 | 689 |
| Yield strength @0.2% offset | N/mm ² | 572 | 510 | 655 |
| Strain (4D) | % | 18 | 12 | 30 |
| Vickers Hardness | HV | 208 | 176 | 216 |

2.2.4 Copper Beryllium Plate with Bump

Copper beryllium (CuBe_2) is used as the top deformable capacitive plate due to its high strength, spring properties, high electric conductivity, and its solderability. It is widely used for both industrial (e.g. spring, flexible hose) and electronics purposes (e.g. connector, contact bridge, switch parts) [68][69]. It has also been used as a flat capacitive plate for a force sensing module in [24]. The variant of copper beryllium used here is

CW101C R580 due to its availability in the form of thin sheets. The properties of this material are shown in Table 2.1.

Prior to the manufacturing of the plate, there were several requirements needed to be fulfilled; namely the shape and dimension of the plate, preferred manufacturing process, and feasibility in manufacturing.

2.2.4.1 The comparison of bump and no-bump plate

Regarding the shape of the plate, when a fully-flat plate is loaded at its center with a circular shape object, the deformation of the plate will be in a bell shape where the maximum deformation is at the center (where the load is applied). The finite element simulation (ANSYS R16.1) of a $6 \times 6 \times 0.1$ mm³ CuBe₂ plate which is subject to a load of 5 N is shown in Figure 2.5. In the simulation, two types of supports were used as can be seen in Figure 2.6. Four fixed supports were applied at the four corners on the bottom side of the plate with the size of 0.8×0.8 mm² for each corner; these supports represent the soldering points. The frictionless support was to represent the support of soldermask layer which the copper plate will rest on (as explained in the PCB design in Section 2.2.3).

Furthermore, according to Eq. 1, this bell-shaped deformation will result in a non-uniform change in capacitance of a parallel plate capacitor in radial direction where the overlap area, A and the relative distance, d between two capacitive plates varies toward the center of the plate. If the initial gap between the two capacitive plates is small, the center of the plate will eventually be in contact with the other capacitive plate which leads to no potential difference between the two plates. This means that with just a flat plate, the two plates need to be distant in order to have a broader range of measurement. However, the large gap can result in a less sensitive sensor since there is an only minor change in the sensor's capacitance which could be difficult to distinguish by the capacitance reading circuit. Therefore, in order to attenuate the effect of the bell-shaped deformation, a cylindrical bump was added at the center of the flat plate. This bump strengthens the center portion of the plate which results in a more parallel and more homogeneous deformation of the whole plate when the bump is pushed by an external force. The simulation result of merging a 0.31 mm-high, Ø3 mm bump on the $6 \times 6 \times 0.1$ mm³ copper beryllium plate is shown in Figure 2.7. It can be seen that more uniform deformation is achieved. Furthermore, the bump allows the sensing of external force easier without any addition components since the force will be exerted on the bump in the center of the plate rather than the other part of the plate.

Chapter 2: Capacitive-Type Force Transducer with a Bump

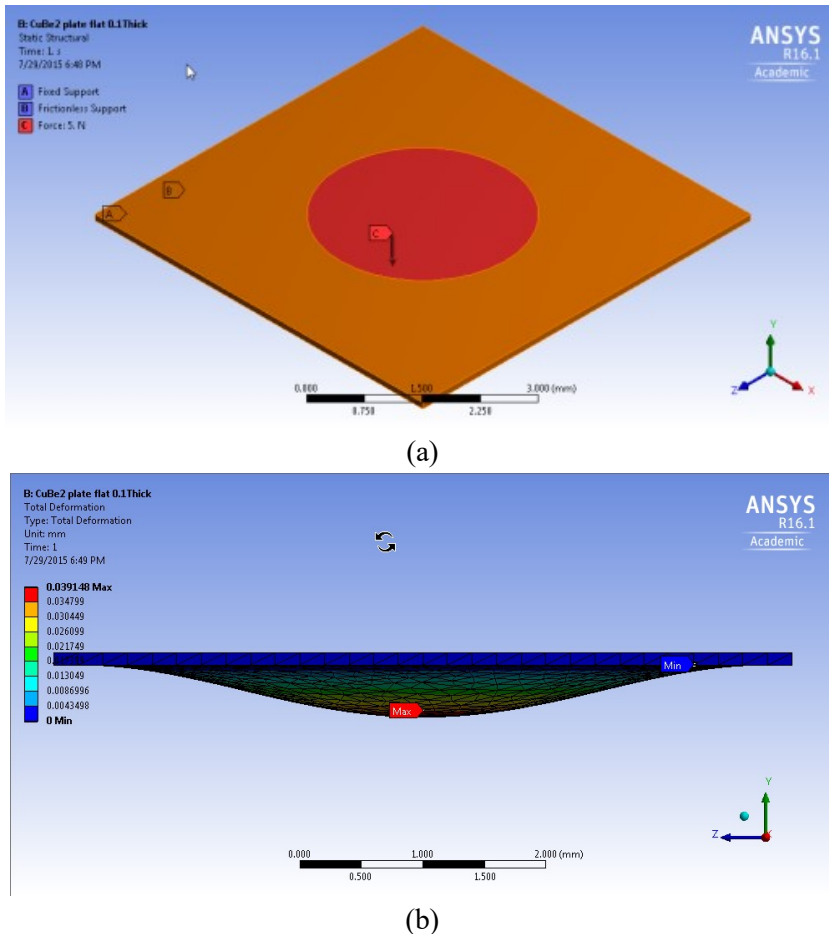


Figure 2.5 The ANSYS simulation of a 6×6×0.1 mm³ CuBe2 plate subject to a 5 N load. (a) The isometric view of the plate where the effective loading area of Ø3 mm is highlighted in red. (b) The side view of the deformation result which has a bell-like shape.

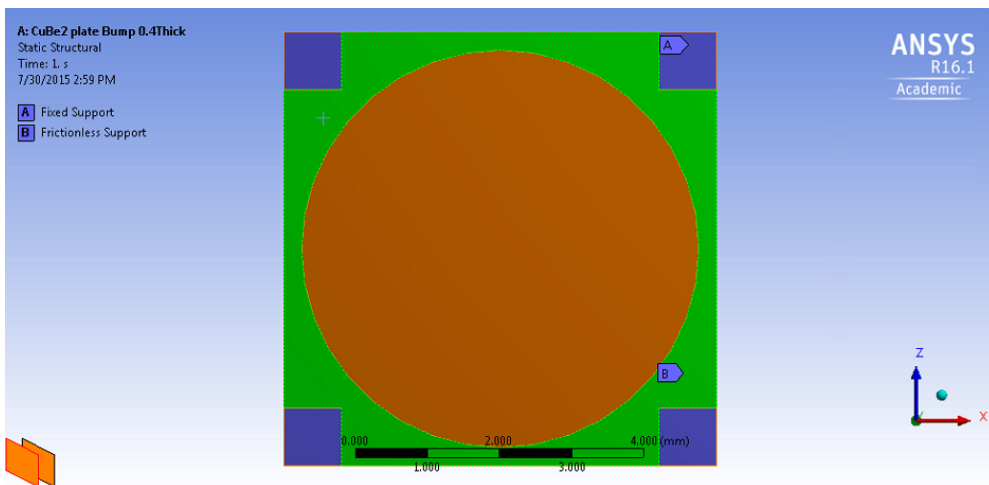


Figure 2.6 The supports under the CuBe2 plate in the simulation. The fixed supports at the four corners are highlighted in purple; they represent the solder points on the PCB. The frictionless support is highlighted in green; it represents the soldermask layer supporting the copper plate. Note that all areas under the plate are at the same level.

Moreover, the uniform deformation of the plate with a bump allows the capacitance to change more with the same deformation distance because not only the area where the force acts on will deform but a wider area of the plate will deform homogeneously. Additionally, with the same magnitude of the normal force, the plate with bump will deform less so it can be placed closer to the signal pad of the PCB in order to gain more sensitivity. Counter-intuitively, a smaller initial distance of the capacitive plates is beneficial for the sensitivity/range. For example, with half the initial distance, double the range with the same sensitivity can be achieved.

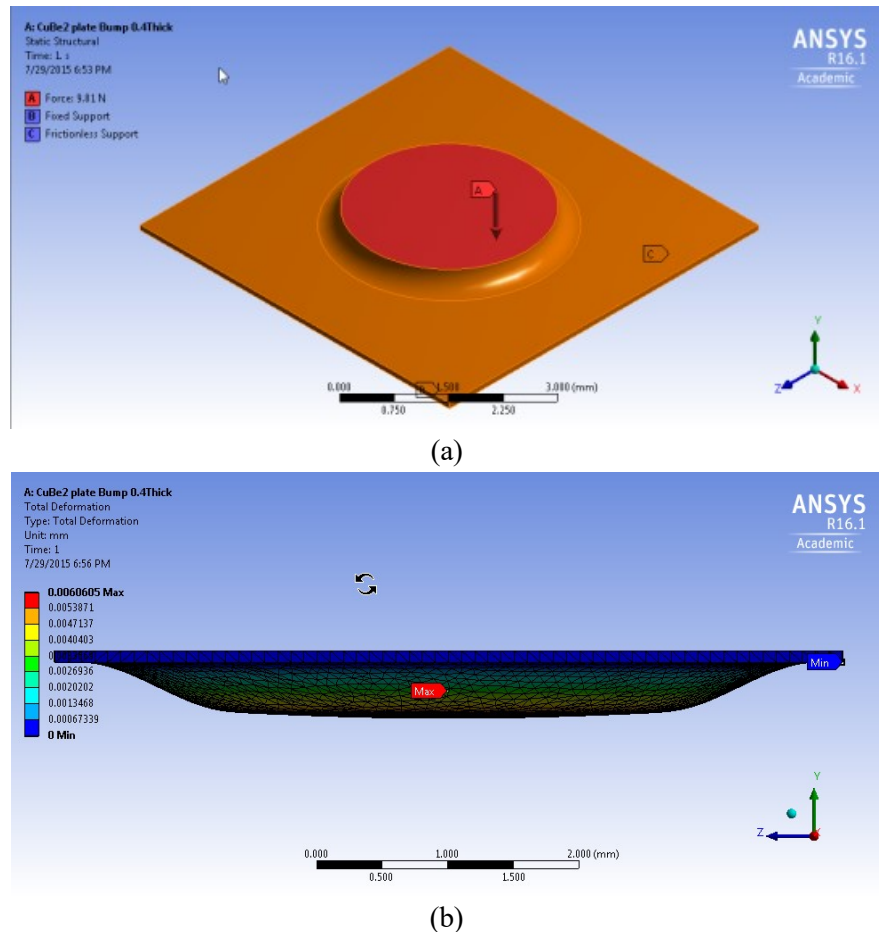


Figure 2.7 The ANSYS simulation of a $6 \times 6 \times 0.1 \text{ mm}^3$ CuBe₂ plate with the 0.31 mm-high, Ø3 mm cylinder bump subject to a 5 N load. (a) The isometric view of the plate where the effective loading area of Ø3 mm is highlighted in red. (b) The side view of the deformation result which is more parallel and more homogeneous.

2.2.4.2 Manufacturing process of the copper plate

Several manufacturing processes were taken into consideration in realizing the desired copper plate. Typical machining process using some cutting bit will cause too much stress on such thin plate of copper beryllium. Electrical discharge machining (EDM) usually

can only perform a through cut. Laser cutting also has the same problem. Moreover, in the above manufacturing techniques, each plate is needed to be produced one at a time.

On the other hand, photolithographic etching uses only chemical treatment to remove the uppermost layer of material to create the desired pattern. The pattern is controlled by applying an etching resist layer on the part prior to exposing the part to the chemical treatment. A batch of the same object can also be produced at the same time. The achievable precision of etching can be around $\pm 20 \mu\text{m}$. One limitation is the undercutting where the material under the edge of the etching resist layer can be removed from the side due to the isotropic property of the chemical solution. Therefore, the aspect ratio between the size of the pattern and the thickness of the material need to be controlled. Accordingly, the final design of the desired copper beryllium plate was done by taking into account the requirements and the limitation of using the etching method.

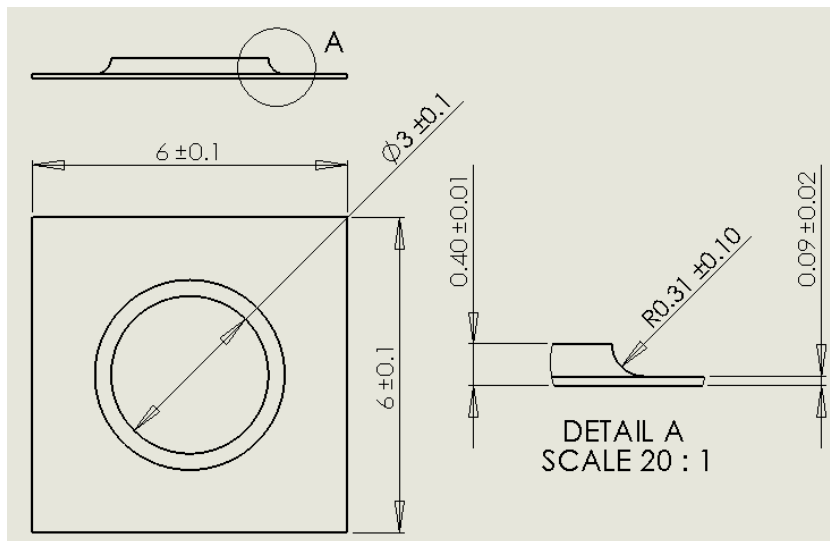


Figure 2.8 The final dimension of the copper plate with a bump. The tolerances were recommended by the etching manufacturer. The fillet of 0.31 was due to the etching characteristic.

2.2.4.3 Final dimension of the copper plate with a bump

Prior to the manufacturing of the sensor, further finite element simulation of copper beryllium plate was done in order to determine the desired dimension of the plate and understand the expected value of force that the plate can withstand and the expected deformation to achieve the high sensitivity yet high force range capacitive sensor.

According to the distance between the capacitive plates of a sensor unit that can be manufactured as mentioned in Section 2.2.3, a 10-micron initial distance is the desired goal to achieve the required sensor range. For the current study, we aimed that each

sensing unit could measure the force up to 5 N (0.510 kg). Furthermore, by considering the accuracy that can be achieved in the production of the copper beryllium plate, we designed the plate so that, with the force of 0.510 kg, the plate will deform around 6.4 microns with the dimension of the plate as described in Figure 2.8; the rest of the 10-micron gap is for the manufacturing uncertainty of the plate and the PCB. The actual copper beryllium plate can be seen in Figure 2.9.

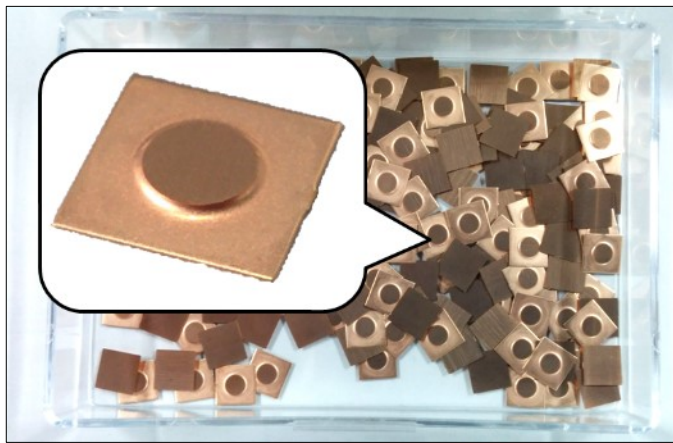


Figure 2.9 The copper beryllium plate with a bump which is produced by photolithographic etching. The plate has a 0.33 mm-high, Ø3 mm cylinder bump and a $6 \times 6 \times 0.09$ mm³ flat base.

2.3 Experiments

2.3.1 Experimental setup

A simple test setup was used to test the sensor measurements resulting from different weights that push against the sensor. In particular, the signal-to-noise ratio test and the accumulated load/unload test were performed with this setup. The setup consists of a set of calibration weights ranging from 1 g to 500 g, a weight placement plate with a Ø6 mm shaft for pushing on the Ø3 mm sensor's knob, a stand with a linear ball bearing bushing that allow only the vertical movement of the shaft, and a digital scale with a resolution of 1 g and the range of 2000 g for monitoring the actual force pushing on the sensor, see Figure 2.10. The sensor PCB is placed on a 3D printed plastic base providing a steady placement for testing and the whole unit is placed on the scale. The microcontroller used for reading data from the sensor is Arduino Due with an SD card module for recording CDC data at a sampling rate of 15 ms. For this configuration of three capacitive sensors, the CDC process of AD7147 is completed every 12.288 ms [62]. The communication between the microcontroller and the sensor is done via an I2C bus.

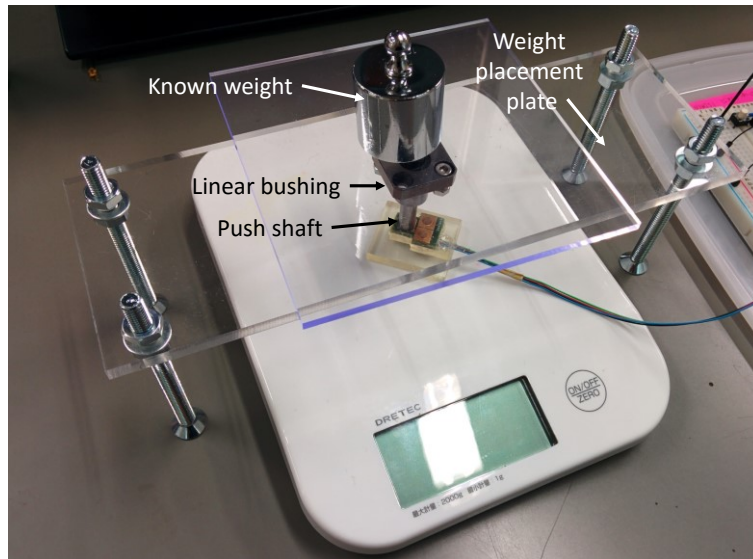


Figure 2.10 Overview of the experimental setup. The setup consists of a digital scale, a linear ball bearing bushing with its support structure, a sliding shaft with weight placement plate.

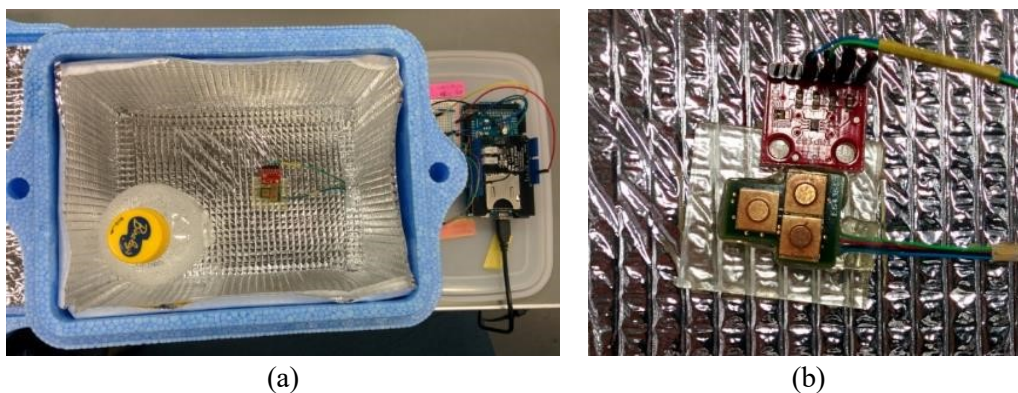


Figure 2.11 Overview of the temperature drift test setup. (a) The expanded polystyrene box covered with an aluminum sheet for temperature isolation. The temperature sensor TMP102 is placed next to the sensor. The Arduino Due is located outside the box for data recording. (b) The close-up view shows the location of the TMP102 and the sensor.

Another experimental setup was also prepared for testing the ability of the sensor to counteract the capacitance drift due to the change in temperature. The simple setup as shown in Figure 2.11 consists of an expanded polystyrene box that is covered with an aluminum sheet in order to maintain temperature, and a closed PET bottle filled with hot water. The temperature sensor TMP102 from Sparkfun is placed next to the capacitive sensor inside the box to monitor the actual temperature as a comparative measurement; it has the resolution of 0.01 °C and I2C interface. The wires of the sensors connect to the

Arduino Due which is located outside the box through a small hole which is covered with an aluminum sheet to minimize temperature leakage. The Due is used for recording the sensor response including the readout of the TCP to observe to what extent the temperature affect the sensor, and also the TMP102 readout simultaneously.

2.3.2 Result and discussion

2.3.2.1 Signal-to-noise Ratio (SNR) Test

This experiment was done with 2 sizes of the load; 0.254 kg and 1.044 kg. Each load was manually put on the weight placement plate which will transfer the force to one of the three sensors, namely S_1 for a period of approximately 5 seconds, and the response of the sensor was recorded. The result is shown in Figure 2.12 and Figure 2.13. The SNR was then calculated according to [70],

$$\text{SNR} = \frac{|\mu_U - \mu_P|}{\sigma_u} \quad (2)$$

$$\text{SNR}_{\text{dB}} = 20 \log_{10} \left(\frac{|\mu_U - \mu_P|}{\sigma_u} \right) \text{ dB} \quad (3)$$

Where:

μ_U = mean value of sensor when not loaded

μ_P = mean value of sensor when loaded

σ_u = standard deviation of value when not loaded

For the load of 0.254 kg, the resultant values are as follow: $\mu_U = 3744.17$, $\mu_P = 6400.95$, $\sigma_u = 0.75$, and those for the load of 1.044 kg are as follow: $\mu_U = 3849.40$, $\mu_P = 16415.07$, $\sigma_u = 0.61$. As a result, the SNR of the 0.254 kg load is 3534.6 or 70.97 dB, and that of the 1.044 kg load is 20638.7 or 86.3 dB which can be considered as very high ratios for the sensor.

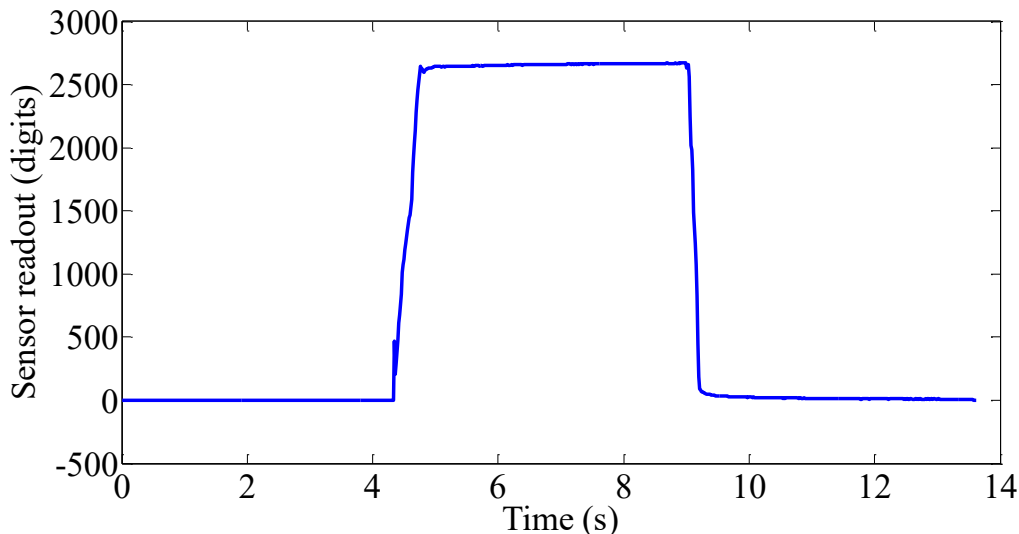


Figure 2.12 The response of the single force sensing unit S₁ to the load of 0.254 kg.

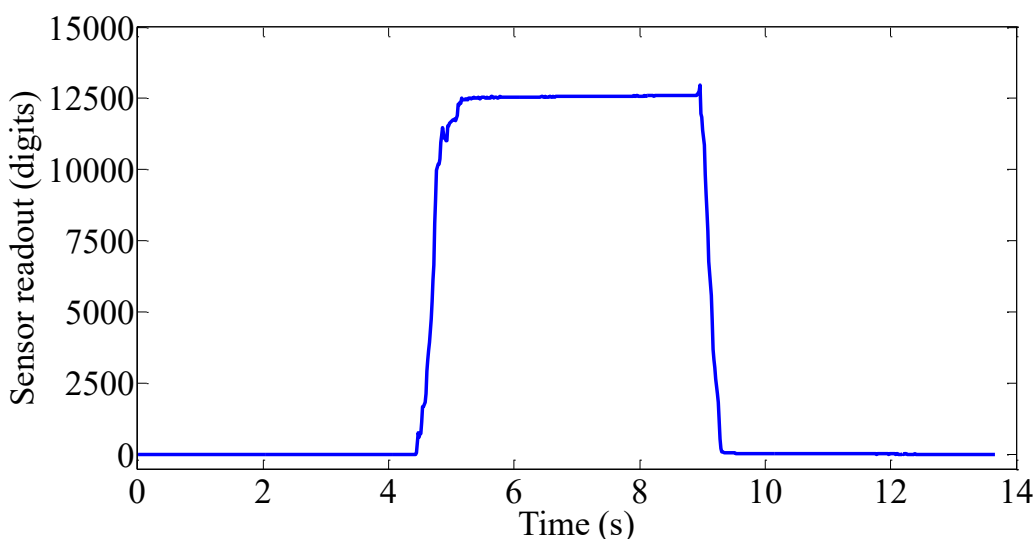


Figure 2.13 The response of the single force sensing unit S₁ to the load of 1.044 kg.

2.3.2.2 Accumulated load/unload test

The purpose of this test is to examine the response of a sensor unit (S₁) to a load change. The test was done by putting weight on manually one after another on the weight placement plate of the test stand to increase the load to the sensor, and then taken out one by one to decrease the load. The load range used here was varied from 0.046 kg to 1.144 kg by using a set of weights which consisted of 0.001 kg to 0.500 kg weights. The load sensed by the sensor also included the weights of the push shaft and the weight placement plate of the test stand which were 0.046 kg in weight). The time in between loading and unloading each weight was approximately 5 seconds and the overall time of the whole loading/unloading experiment was around 2 minutes 30 seconds.

The time series of the sensor readout of S_1 is shown in Figure 2.14 where the stepwise change of loading and unload can be seen. The hysteresis can be found in the sensor due to the difference in readout value of the same weight during loading and unloading period, the maximum drift that can be found is 636.77 digits or approximately 0.042 kg, and the average drift is around 212 digits or 0.014 kg which can be considered as a low level of hysteresis providing that a unit can measure the force up to 1.144 kg.

The response of the S_1 to the weights in both the load and unloading sequence is shown in Figure 2.15. It can be seen that loads of approximately 0.046 kg to 0.150 kg were located very close to the linear approximation line. However, the loads of around 0.200 kg and above gradually went under the line, but the response of the final weight of 1.144 kg went beyond the line. However, the resulting response can be considered sufficient for many tasks with humanoid robots.

Additionally, the maximum standard deviation of the sensor readout in this test was 81.16 digits, which is found at the unloading of the heaviest weight of 0.500 kg. This considered to be small since the mean readout at that step was approximately 8800 digits; it was only 1% of the sensor readouts. The average value of all standard deviation of the whole test was 13.79 digits and the lowest standard deviation is 1.74 digits.

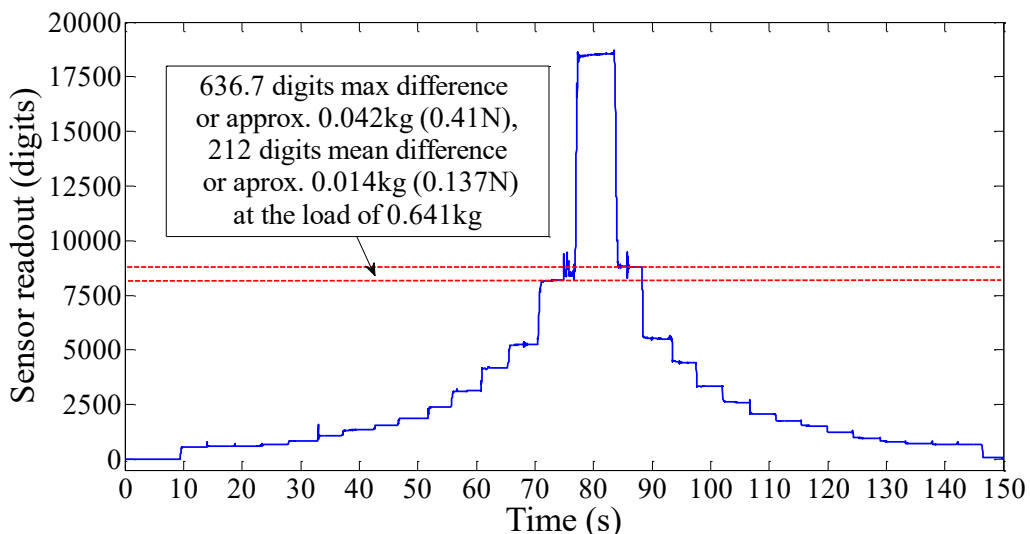


Figure 2.14 The response of the capacitive sensor S_1 which was subjected to different loads is plotted against time. Different readouts between loading and unloading sequence can be seen. The maximum difference is approximately 0.042 kg (0.41 N) found when the load of 0.641 kg was applied. The biggest mean difference is approximately 0.014 kg (0.137 N) found when the load of 0.641 kg was applied.

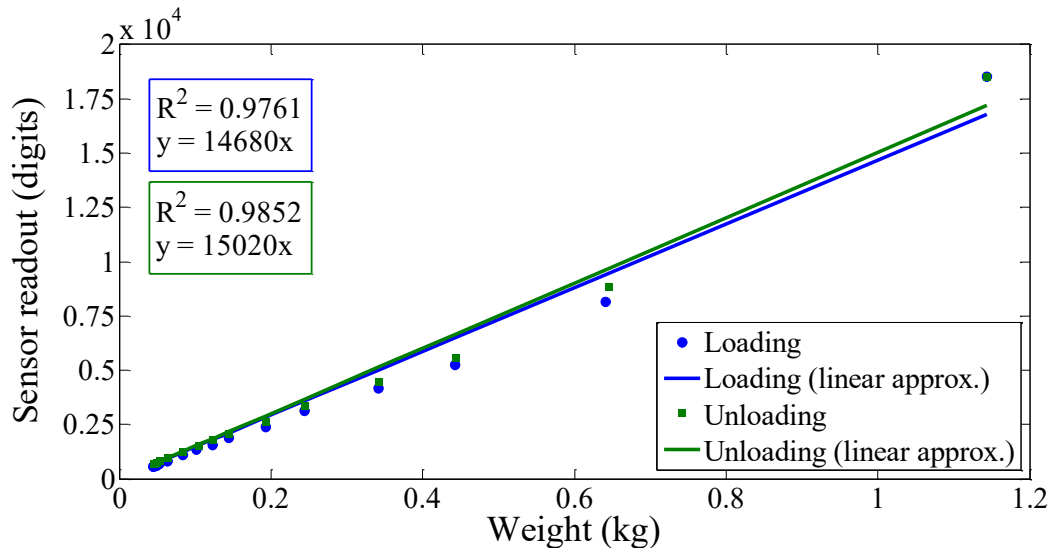


Figure 2.15 Loading/unloading test plot of the average of the sensor readout. The load is range from 0.045 kg to 1.144 kg.

2.3.2.3 Temperature drift test

This test is aimed at studying the feasibility of using the TCP to counteract the thermal drift in the sensor measurements. The test was done by monitoring the drift in sensor readout signals due to the change in temperature.

The experiment starts by using the room air conditioner to cool down the sensors, as well as the overall temperature of the room where the experiment is performed until the temperature drops to around 20°C. After that, the bottle filled with hot water was put inside the box and the box was closed to allow the temperature inside to rise to 40°C. The box was then opened again to allow the temperature to gradually drop to around 25°C while the bottle was still kept inside the box to achieve a slow drop in temperature.

As the result of the experiment as shown in Figure 2.16, it can be seen that the drift of both a force sensing unit (S_1 , in green) and TCP (in blue) responded to the thermal variation in almost the same fashion but at a different magnitude. The S_1 was more responsive to the change than the TCP. A simple compensation trial has been done in order to test the feasibility of temperature compensation by subtracting the drift in S_1 with the drift in TCP times with a fixed gain (5 in this case) in a similar fashion as can be found in [20]. The result of compensation is not perfect but drift in S_1 is reduced from the maximum value of around 140 digits to 20 digits and the rest of the drift almost stay in a band of ± 20 digits which can be roughly translated into ± 0.002 kg misread.

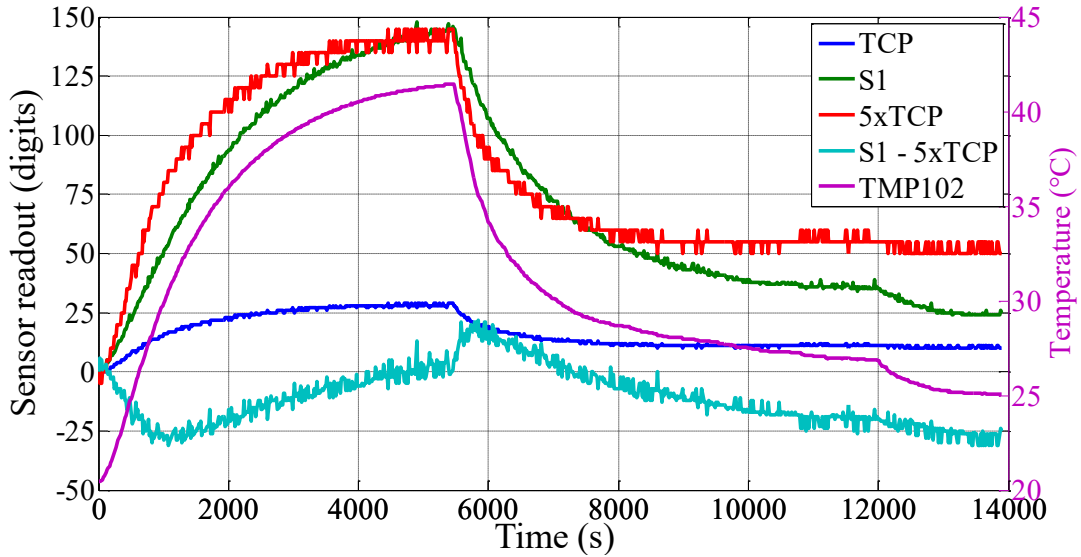


Figure 2.16 The effect of temperature change on the sensor is shown together with an attempt of compensation of sensor readout (S1, green) readout (cyan). The compensation value comes from the drift in TCP (blue, red (5-time scaled)) and the actual temperature is sensed by TMP102 (magenta).

2.4 Conclusion

The chapter presented the prototype of a capacitive-type force sensing unit in order to examine the performance of the sensor. In this study, the finite element simulation of the copper beryllium plate was done prior to the manufacturing of the actual plate to finalize the dimension of the plate and, more importantly, to confirm the benefit of the bump in allowing a more parallel deformation; more sensitivity and range of measurement can be achieved. The experiment for investigating the performance of the actual sensor was then performed. It included the test for determining the signal-to-noise ratio of the sensor, the loading/unloading test to see how linear the response of the unit can achieve and what level of hysteresis occur in the implementing of copper beryllium as the deformable transducer and the test of thermal variation's influence on the sensor. The results of the experiments shown that with the implementation of the copper beryllium plate, the AD7147 chip and the careful design of the sensor PCB, very high SNR, low hysteresis sensor with a high sensitivity was obtained and also an ability to compensate the effect of the thermal change.

3 DISTRIBUTED TACTILE SENSING OF MR-FLUID HAPTIC INTERFACE

In this chapter, a two-way tactile interface is suggested as an example of the many applications that tactile sensor can be used. It can provide a user a tactile sensation of variable stiffness surface while the interface itself is able to measure the force input from the user including the location where the force is applied to. The capacitive tactile sensor developed in chapter 3 was used as the interface's sensing part, and the adjustable stiffness was realized using MR fluid. The concept of this haptic interface is discussed first and then followed by the implementation of the interface including the production of the interface structure, the electromagnet, and the MR fluid-filled pouch. Later on, a set of experiments was conducted in order to evaluate the interface especially the effect of various stiffness on the response of the capacitive sensor, the spatial resolution, and the crosstalk of the sensor. The result showed that the capacitive sensor is not affected by the presence of the magnetic field, and the effect of the variable stiffness on the response of the sensor is minor. The tactile sensing of the interface has the spatial resolution of 2 millimeters.

3.1 Brief introduction to haptic interface and magnetorheological fluid

An increasing number of tactile interfaces exist, for example, the success of tablet computers and smartphones would hardly have been possible without advancements in tactile sensing devices. At the same time, there is an increasing number of devices to provide tactile feedback to the user. Yet, the haptic feedback is usually limited to vibrations. Other devices, such as Phantom, provide force feedback to the user. Recently, MR fluids have shown their potential to provide easily controllable changes in stiffness; in particular MR fluids have been used successfully for adjustable damping in luxury cars.

Many different ways exist to provide haptic feedback to the user [71], including vibration, forces or motions. The applications are widespread, ranging from manufacturing to rehabilitation and recreation. In manufacturing, teleoperation in assembly tasks is a topic of interest [72][73]. In the field of rehabilitation, work has been done to restore haptic feedback mechanisms in amputated limbs. In [74] a multi-functional haptic device was developed that could provide touch, pressure, vibration, shear force, and temperature feedback to amputees using sensors placed on a prosthetic hand in order to enhance the control of grip force. Commercially available haptic feedback devices use different types of actuation [75], the most common being DC motors. Other types include shape memory metals, magnetic and piezoelectric materials, and electrorheological fluids.

Recently, devices using MR fluid have also been proposed. MR fluids are a kind of smart materials, based on ferromagnetic particles suspended in a non-colloidal medium. These materials are able to change their rheological properties, i.e. apparent viscosity when placed in a controlled magnetic field. Nowadays, there are several kind of devices that employ the properties of these materials to create unique behaviors. Adaptive damping systems for limb assistance [76], variable stiffness clutches for telerobotic applications [77], and magnetorheological valves for hydraulic systems [78] are examples of such devices.

Currently, there are even commercially available products from LORD⁴, in particular, they provide MR dampers. Some works have shown also the potential of MR fluids for haptic interfaces, for example [79].

⁴ www.lordmrstore.com

3.2 Concept

The concept of the proposed two-way tactile interface is shown in Figure 3.1. In order to provide the user the feeling of variable stiffness, MR fluid is filled inside a pouch made of a thin layer of nitrile rubber which is oil-resistant. MR fluid is a kind of smart materials based on ferromagnetic particles suspended in a non-colloidal medium. The fluid is able to change their rheological properties, i.e. apparent viscosity when placed in a controlled magnetic field. Furthermore, since the concealed fluid needs to be made as a part of the magnetic circuit in order to utilize its adjustable stiffness property, metal screws are used to penetrate through the bottom of the pouch while maintaining the sealant of the pouch. The other ends of the bolts then connect with the rest of the magnetic circuit where the electromagnet provides magnetic flux to the circuit. By controlling the current fed to the electromagnet, the stiffness of the MR fluid can be controlled.

For the tactile sensing part of the haptic interface, two of the capacitive sensors developed in Chapter 3 are placed under the pouch. Two sensors consisting of 6 force transducers in total are sufficient to cover the area under the pouch. By touching on the top of the pouch, the tactile sensor can sense the location and the force magnitude of that touch.

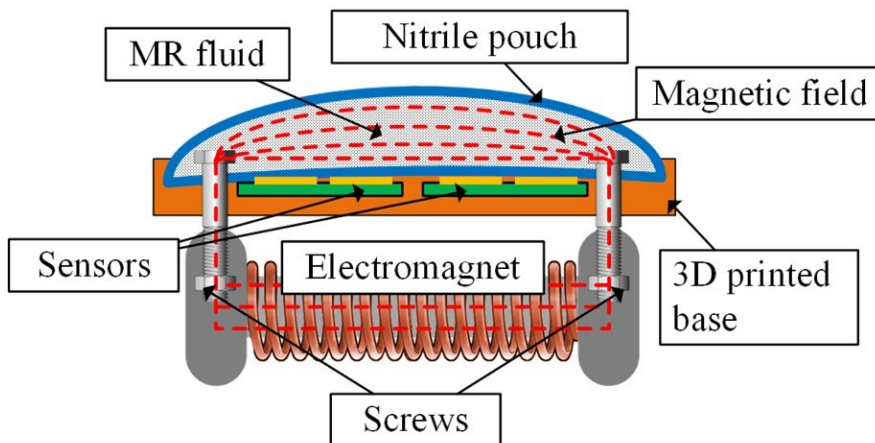


Figure 3.1 The diagram showing the working principle of the device and the location of each component.

3.3 Implementation

To realize the proposed haptic interface concept, a prototype was produced. The different parts of the device are discussed in this section.

3.3.1 Electromagnet

The electromagnet was built by manually winding copper wire around a metal core. The metal core used here was a metal shackle used in typical construction. The copper wire used here has a diameter of 0.8 mm. The number of turns is around 400 turns in order to provide sufficient resistance to reduce the overall current not to exceed the rated current of the copper wire, and more importantly, in order to have a sufficiently strong magnetic field to utilize the adjustable stiffness property of MR fluid.

The electromagnet is shown in Figure 3.2. The upper parts of the circular holes were surfaced and drilled. The flat top is used to support the upper portion of the interface, and the holes are for the metal bolts which are used to connect the MR fluid in the pouch to the electromagnet.



Figure 3.2 The electromagnet used in the proposed haptic interface.

3.3.2 Device's support structure

The support structure for the capacitive sensors and the MR-filled nitrite pouch is shown in Figure 3.3. It consists of the top and bottom support plastic pieces which were 3D-printed. The top's sealant canal and the bottom's sealant ridge together are used to assist the pouch in preventing leakage of the fluid. This sealant was used when the pouch was being produced as well; further detail on this will be explained in the next section. Under the top support, there is a side canal for the rubber tube which attached to the pouch and was used to fill the MR fluid into the pouch.

The two bases located at the center of the bottom support are used to support the two capacitive sensors. The cavities on the bases are for the CDC chip and the capacitors used in the circuit board of the sensor. Hot glue was confirmed to be sufficient to hold the PCB

firmly in place on the bases. The wires of the sensor go under the bottom support via the slot located in the middle of the two bases.

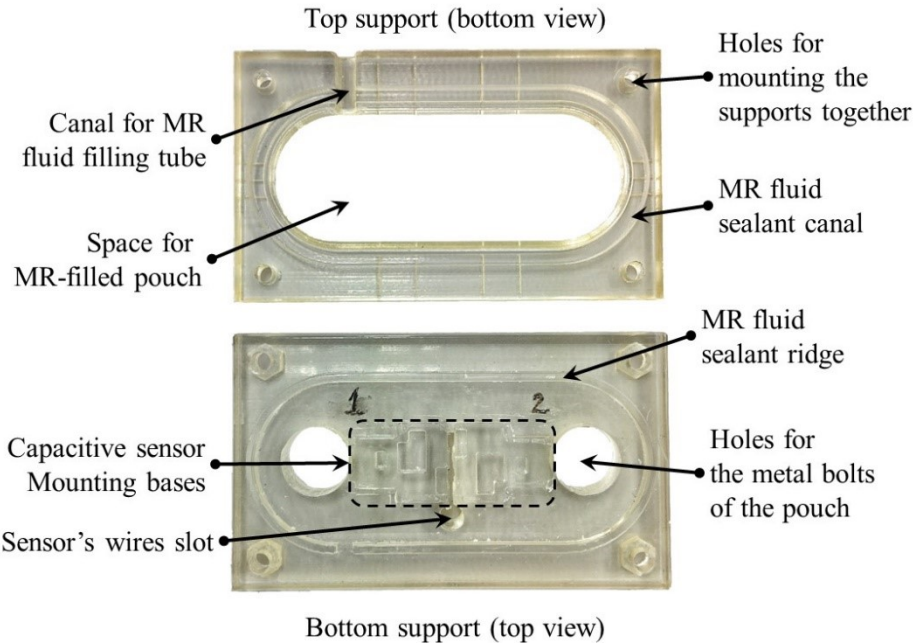


Figure 3.3 The top and bottom support for the sensor and the MR-filled pouch.

3.3.3 MR fluid pouch

The pouch for containing the MR fluid was custom-made using two sheets of 0.2 mm and 0.075 mm thick nitrile rubbers. The thicker nitrile sheet was used as the bottom part of the pouch in order to prevent tear due to the rubber being in contact with the sensor while the thinner sheet was used as the top part to reduce the stiffness of the rubber which might affect the feeling a user feels. For the production of the pouch, firstly, the top sheet of the rubber was slightly heated and stretched on a curve-contour metal in order to form a desired half-capsule-like shape. The two sheets were then pressed in between the support plates with screws and clamps as shown in Figure 3.4 in order to form an impression of sealant ridge from the support plates on the sheets. This ridge on the rubber was to display the location which the two sheets would be bonded together with super glue. After pressing for approximately 1 hour, two holes were made on the bottom rubber sheet according to those on the bottom support plate and two metal screws were tightened firmly to prevent leakage around the holes. The rubber tube was also inserted at the designated position provided by the top support and glued to the rubber sheets as well. The super glue proved to be sufficient to completely bond the nitrile sheets and the tube together. After the sealing is done, MR fluid was filled into the pouch using a syringe. The MR fluid used here is MR fluid E-600 from Sigma Hi-Chemical. It consists of 80%

magnetic particle with the specific gravity of 3.0 and the viscosity of 7450 mPa/sec at 20 °C. The air inside the pouch was also removed with the syringe as well. The amount of the fluid of around 4 milliliters was filled into the pouch in order to make the pouch marginally full (slightly stretched).



Figure 3.4 The process of forming an impression of sealant ridge on the two nitrile rubber sheets. The two sheets are pressed in between the support plates with screws and clamps.

3.3.4 Haptic Interface

The completed haptic interface can be seen in Figure 3.5. The pouch, the capacitive sensors, and their support plates were assembled together and rested horizontally on another base where they were mounted by the two screws to the electromagnet which located under them. The tube was inserted with a plastic plug to prevent the MR fluid from coming out of the pouch. There were 2 sets of wires for the two capacitive sensors. This is due to the fact that the prototype PCBs were identical to simplify the PCB design and to reduce costs of producing the PCBs. As a result, every PCB had the same I2C address. Therefore, the complete set of wires was necessary for each sensor. Underneath the device, as shown in Figure 3.6, the bottom of the CDC chips can be seen as well as the connection between the pouch and the electromagnet via the two metal screws.

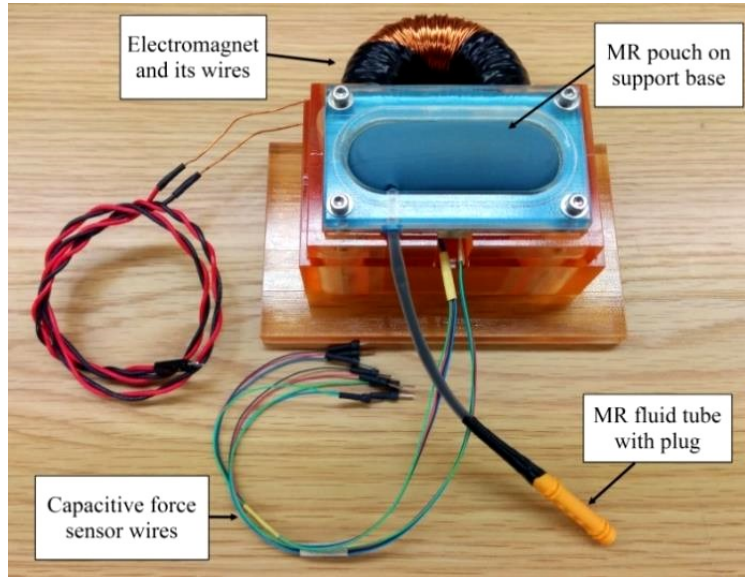


Figure 3.5 The finished device, from above, the pouch (blue) filled with MR fluid can be seen. Also, the wires that connect to the sensor and the ones that connect to the magnet can be seen.

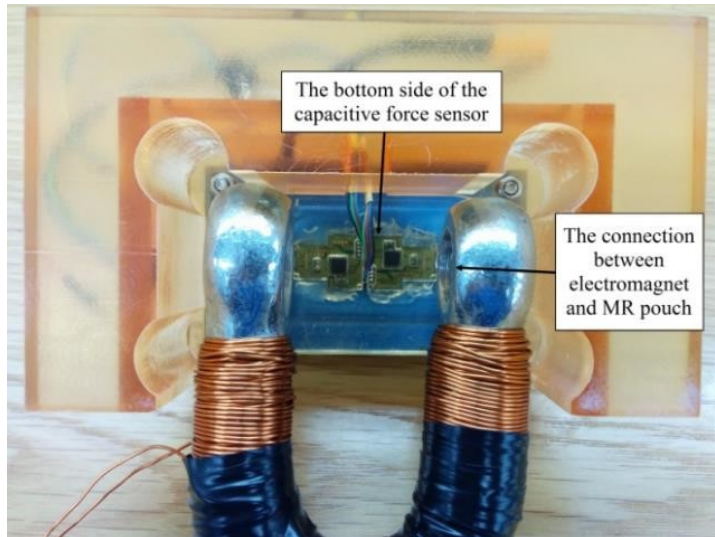


Figure 3.6 The bottom side of the device. The bottom of the sensors and the magnet can be seen.

3.4 Experiments

3.4.1 Experiment setup

Two experimental setups are used here. The first setup consists of an x-y table, a vertical force transfer structure using a linear bushing and a set of weights. The push rod of 6 mm in diameter was used to transfer the weight to a sensing unit (see Figure 3.7). This setup was used to evaluate the sensor response under the MR pouch. In the experiment, different

currents were applied to the magnet and the device was loaded with different loads, and the sensor measurements were taken. At each value of magnetization current, 5 weights would be loaded on a sensing unit. The weights of 50 g, 100 g, 200 g, and 500 g were individually placed on the weight placement plate (which weights at 18.6 g including the push rod) and manually put on the sensing unit at 5 seconds interval. At each unload interval, no current would be provided to the MR pouch in order to restore the default shape of the pouch, and the pouch would be magnetized once again before the next loading cycle. The restoration of the pouch shape and the magnetization take approximately 1 second. An Arduino Due was used to monitor the sensor readout via I2C bus.

The second experimental setup is shown in Figure 3.8. The device was mounted on the support of a sturdy press drill, which included an x-y-table. Force was applied to the device with a voice coil motor (VM5050 from Geeplus) which has a nearly linear relationship between output force and input current. The voice coil motor was then controlled with a full-bridge motor driver LMD18245 from Texas Instruments which has internal current control. Another LMD18245 was used to control the current supply to the MR pouch in order to automatically control both the pushing force and the strength of the magnet at the same time. At the end of the voice coil motor's shaft, a push rod with a diameter of 8 mm was installed; a slightly larger push rod compared to that of the first setup was chosen to ensure that there is, at least, one sensing unit being pushed at each 2 mm space with a total length of 26 mm. Each push would be performed at the interval of 10 seconds with an unload cycle of another 10 seconds. The restoration of the pouch shape and the magnetization was done in the same fashion as in experiment 1. An Arduino Due was then used to control both devices and also to collect the sensor measurements. We tested the response of the sensor under different levels of magnetization of the MR fluid. This setup was used to study the sensor response not only under different levels of magnetization but also at different locations of force exertion.

3.4.2 Result and discussion

Figure 3.9, Figure 3.10, and Figure 3.11 show the response of the sensors to the 5 weights (18.6g, 68.6g, 118.6g, 218.6g, and 518.6g) when the magnet was powered with 0, 2, and 4A, respectively. Even though the viscosity of the device changed a lot, the sensor readings were nearly the same for all currents. Furthermore, very limited crosstalk between the sensors can be observed. With the maximum current, the sensor response

was slightly lower, and minimal crosstalk appears, which was expected. Overall, our experiments show that the sensor can work below the MR fluid, even though a magnetic field was applied, and even though the viscosity of the pouch above it had drastically changed.

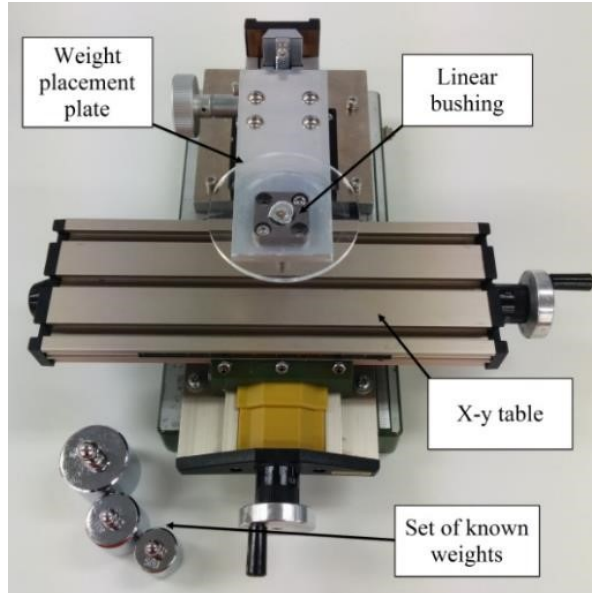


Figure 3.7 Experimental setup with a set of weight and the vertical force transfer structure.

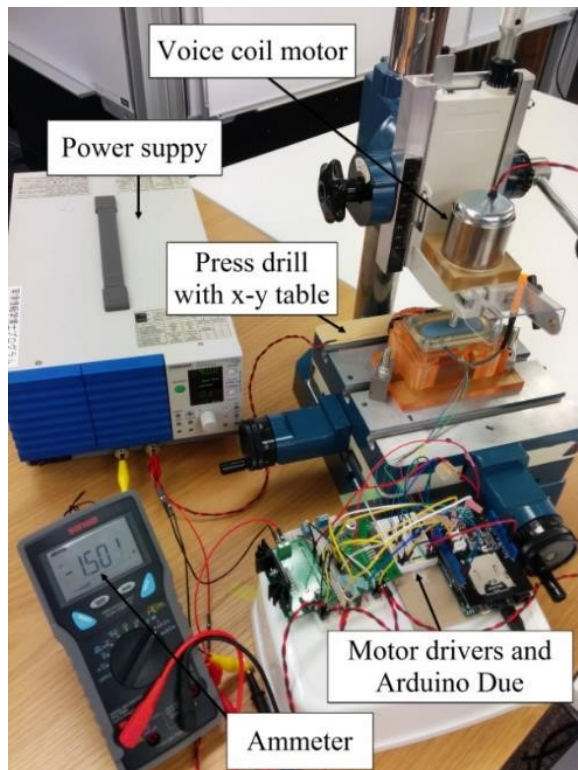


Figure 3.8 Experimental setup with a voice coil motor, two motor drivers, Arduino Due and an ammeter.

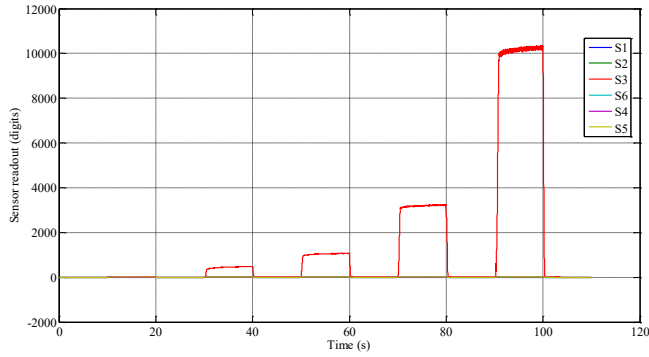


Figure 3.9 Sensor response to different loads when the magnet is not powered

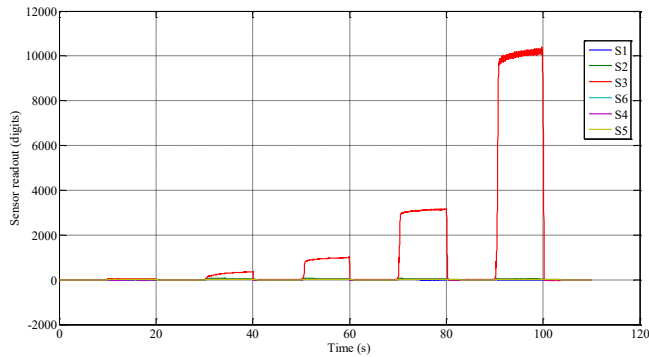


Figure 3.10 Sensor response to different loads when the magnet is powered with 2 A.

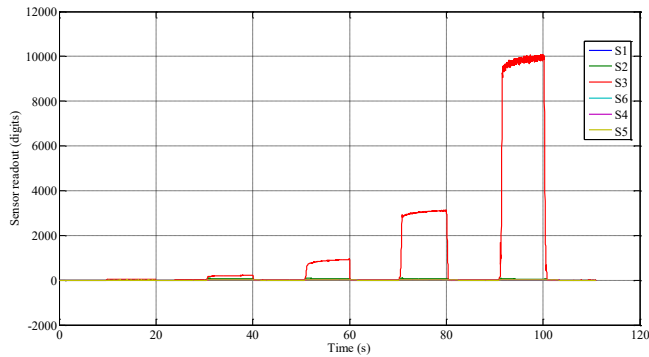


Figure 3.11 Sensor response to different loads when the magnet is powered with 4 A.

Figure 3.12 shows the response of the sensor under magnetized MR pouch when a constant force of 450 g was being applied to the device at different positions; three

different responses from 3 different magnetization currents (0 A, 1.5 A, 2.5 A) were overlaid to show the effect of different currents. The sensor was pushed at different locations; at 2 mm spacing between each push and the diagram of pushing position is shown in Figure 3.13 along with the sensor number. The transition of force from one sensor to another can be seen in Figure 3.12; it shows that every 2 mm space the force can be sensed by the sensor. More importantly, it can be seen that with higher magnetization current, the transient response of each push is more noticeable. There was a difference of approximately 7% in sensor readout between when the magnet was powered and when it was not but there was only a slight difference in readout between the magnetization current of 1.5 A and 2.5 A of only 2%, and it was not always the case that less force will be sensed at the higher magnetization current. Hence, it can be said that the variation in the magnetization current has no significant influence on the force sensing of the sensor located underneath the MR pouch. Even being loaded with the same force, the response of S₁ was less than that of S₂ and S₅ because the area of the sensor's knob which was pushed by the push rod was smaller in the former case. Finally, the reason why S₆ has higher readout than the others will be further investigated in future work.

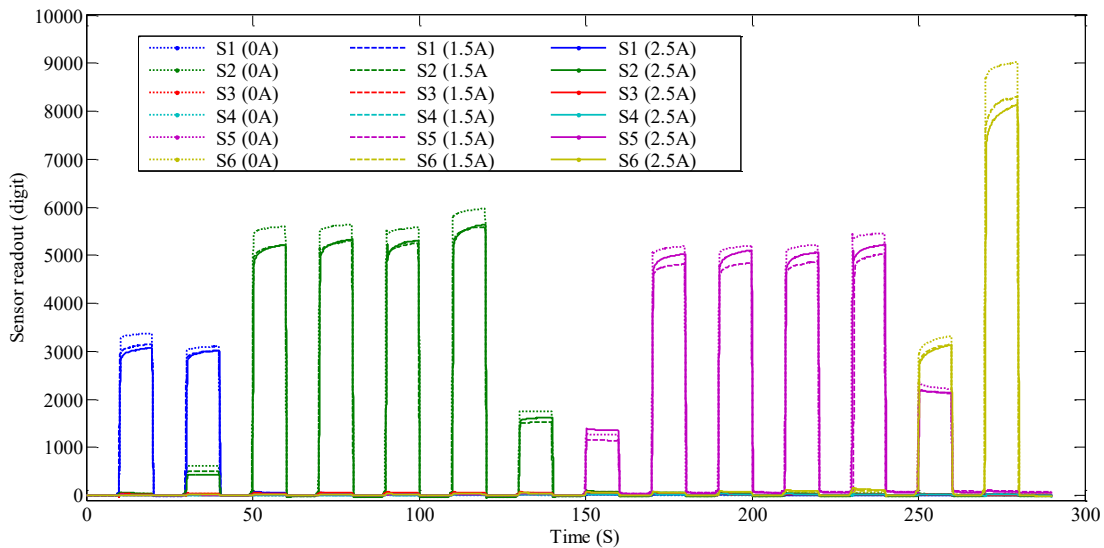


Figure 3.12 Spatial response of the sensor to the load of 450 g with 2 mm spacing between each push. The resultant response at 0 A, 1.5 A, and 2.5 A of magnetization current is shown together.

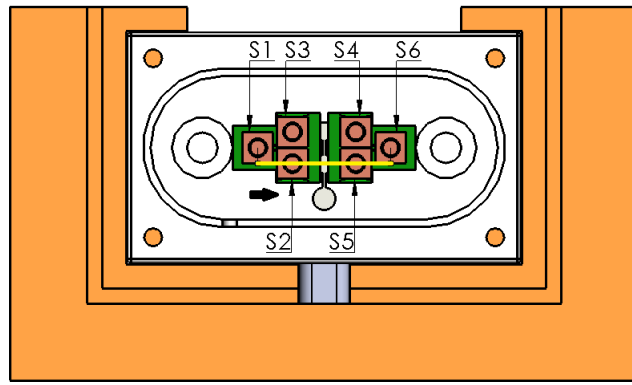


Figure 3.13 The layout showing the location of each sensing unit with designated number. The 26 mm trace (yellow line) and the direction of movement (black arrow) of the push rod of the spatial test also shown here.

3.5 Conclusion

This chapter presented a novel haptic device using the combination of MR fluid to provide the user the adjustable stiffness and the capacitive tactile sensor to sense the external force exerted by the user. The adjustable stiffness was realized by adjusting the amount of magnetic field flow through the MR fluid. The tactile sensor used here was first implemented in the previous chapter and it is shown here in this chapter that the sensor can be used in another application not only for force sensing in the robotics field. The haptic device was tested with several experiments, and the results showed many interesting findings. We found that the capacitive force sensors work correctly regardless of the magnetic field; the external force acting on the MR pouch can be sensed by the capacitive sensor while the stiffness of the pouch is being changed. The compliance of the pouch only slightly affected the force sensing response. In particular, the transient response lasts slightly longer when the pouch is stiffer. Interestingly, it is discovered that the MR pouch can actually provide an additional feedback to the user; the vibration of the MR pouch can be generated by reversing the direction of the input current of the electromagnet. The frequency of the vibration is proportion to the switching frequency of the input current.

4 3-AXIS DISTRIBUTED SOFT SKIN SENSOR

In this chapter, the implementation of the capacitive transducers for 3-axis distributed force sensor is presented. The novelty lies in the arrangement of the transducers in such a way that tri-axial force acting on a smooth and soft skin sensor's surface can be sensed. As a result, the sensor possesses not only high sensitivity but also a compliant property which is important for ensuring safe interaction between humans and robots. Additionally, the sensor provides digital 2-bit-address I2C output which can reduce the number of wiring required when a network of multiple sensors is to be implemented on an actual robot where only limited space is available. The concept of how this skin sensor works is described first. The two prototypes of the sensor are then explained. The design and the production process are presented including several requirements which needed to be fulfilled during the realization of the proposed sensor. The experiments and results of the evaluation of the two prototypes are then discussed. Lastly, the conclusion and the future work of the sensor are provided.

4.1 Concept

In order to be able to distinguish and measure a force vector which composes of normal and shear forces while still being compliant and have a smooth and flat outer surface, the proposed skin sensor has four capacitive-type force sensing units tilting in different directions and covered with a soft material in particular silicone rubber, as can be seen in Figure 4.1. This allows the sensor to sense and distinguish the shear forces exerted on the

upper skin surface while the softness of the sensor is not compromised. For each tilted force sensing unit, two copper beryllium plates with a bump are used as a double-sided force sensing unit as one force sensing unit consisting of a copper beryllium plate and a copper foil located on one side of the PCB. The benefit of the bump (the cylindrical extrusion of the copper beryllium seen in Figure 2.1) is to foster the parallel deformation of the copper beryllium to enhance the sensitivity/range of the sensor which has been presented in Chapter 2. Furthermore, the double-sided capacitor can potentially enhance the sensitivity of the sensor with respect to a single sided capacitor [80].

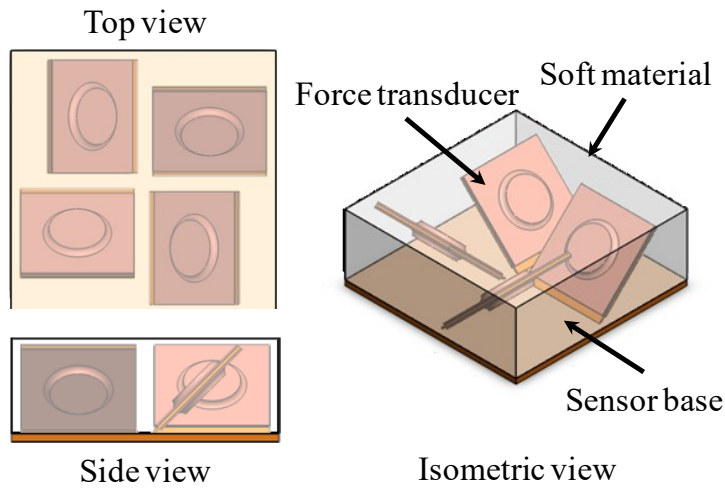


Figure 4.1 The conceptual design of the proposed 3-axis distributed skin sensor. The views of the sensor from the top, the side and in the isometric perspective can be seen.

The ability of the sensor to detect the force vector can be explained as follows (see also Figure 4.2). When there is only a normal force acting on the center of the sensor, all four transducers will sense the same magnitude of force equally. However, when a shear force additionally acts on the sensor, the transducer which points in the same direction as the shear force will sense more force while the other transducer which points in the opposite direction will sense less force. The other two transducers which are perpendicular to the shear force will not sense the shear force.

When the sensor is being exerted by a force, not only the copper beryllium plates are elastically deformed, but also, the bending angle of the transducer is expected to temporarily change (this is due to the fact that the transducers are surrounded by a compliant material such as soft silicone rubber). It is beneficial because it allows the transducers to be closer to the surface which increase its sensitivity, and at the same time maintain the overall compliance of the sensor.

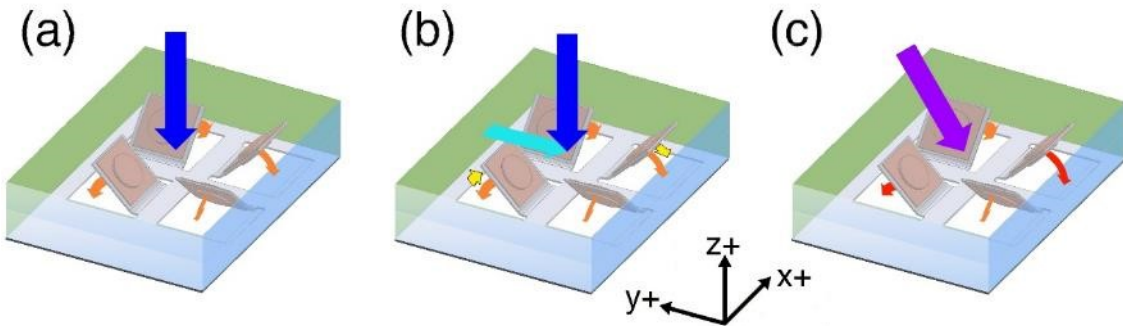


Figure 4.2 The force detection principle of the proposed skin sensor. (a) When a normal load (blue) is applied to the top of the sensor, all 4 sensing units sense the force (orange). (b) When a shear force (cyan) is added, the force sensed by the pair of 2 perpendicular sensing units becomes increased and decreased, respectively (yellow). (c) The resultant forces of input force (purple) and the sensed forces of all 4 units (red and orange) are shown.

4.2 Implementation: Version 1

As the first prototype of this novel 3-axis soft skin sensor, this version of the sensor mainly focused on the feasibility evaluation of the 3-axis force detecting ability of the proposed concept while the following requirements were not the priority at the moment of developing the first prototype:

- The miniaturization to make the sensor the most space efficient
- The compatibility of being distributed sensory network
- The highest spatial resolution possible
- The optimization of the transducer's size
- The optimization of the bending angle of the transducer.
- The finding of the most appropriate compliant material.
- The complete shielding of the analog traces.

Indeed, these requirements are important for the sensor to be effectively used on robots, but the feasibility of the concept needed to be tested first.

4.2.1 Circuit design and manufacturing

In order to test the feasibility of the proposed concept in detecting 3-dimensional force, the sensor's circuitry was designed to be made of flexible PCB. This allowed the circuit, especially the transducers' portions which were embedded in the circuit to be able to bend up.

The overview of the circuit can be seen in Figure 4.3. The PCB is $24 \times 32 \text{ mm}^2$ in size, and it has two layers. On the top side, there were five capacitive electrodes; four for the force sensing purpose where the copper beryllium plates would be put above each electrode and act as a deformable reference ground for each capacitive sensor. The other one was called Temperature Compensation Pad (TCP) which was designed for monitored the thermal change effect as what had been done as well in the previous chapters. Additionally, at the bottom of the top side, four small copper pads representing I2C port can be seen; using I2C port can reduce the amount of wiring required when installing several sensors on a limited space on any robot. Since AD7147 has a configurable 2-bit address pins for I2C addressing, four of the chips can share the same data line (SDA). On the bottom side, the other pairs of electrodes can be seen. This side as well that the copper beryllium plate would be placed above each electrode to create double-sided force transducers in order to increase the sensitivity of the sensor.

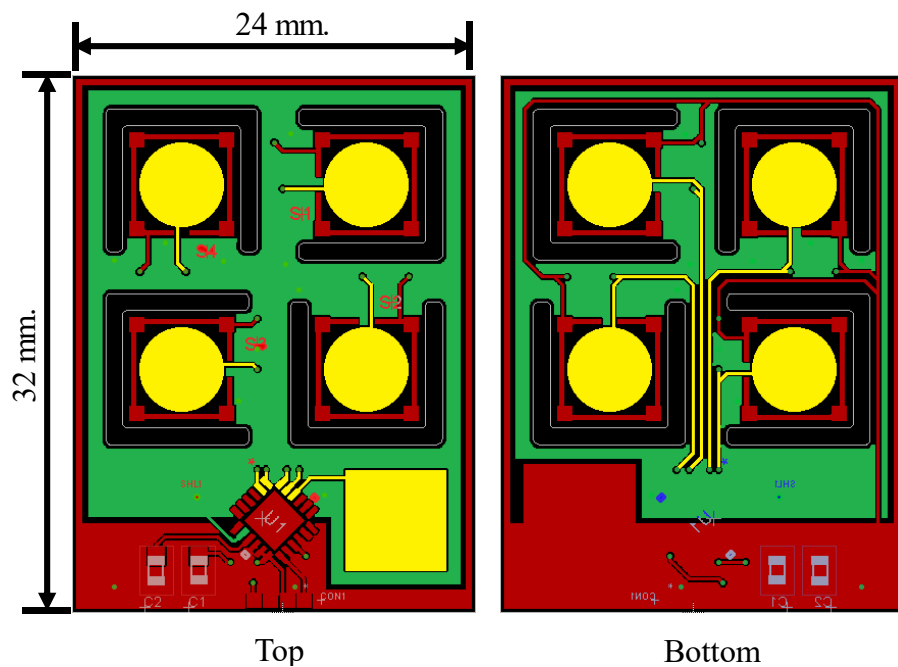


Figure 4.3 The overview of the circuit. It shows the capacitive electrodes and their traces (yellow), the ACShield area (green), and the ground area (red). The top view is shown on the left and the bottom view is on the right.

4.2.1.1 Enlarged surrounding pad

The force sensing of the transducer part used here was the same design of the copper beryllium plate used in the earlier chapters due to its advantages in improving the sensor's sensitivity and measurement range. However, the surrounding copper pads which were used to mount the CuBe₂ plate to the PCB was enlarged to be 0.2 mm bigger than the

plate's width, see Figure 4.4. This could potentially help in spreading the excess solder out in order to maintain the capacitive gap of the sensor comparing to the sensor designed in Chapter 3 where the width of the surrounding pads (the four pads at the corner, see Figure 2.3(a)) was the same as the width of the copper beryllium plate.

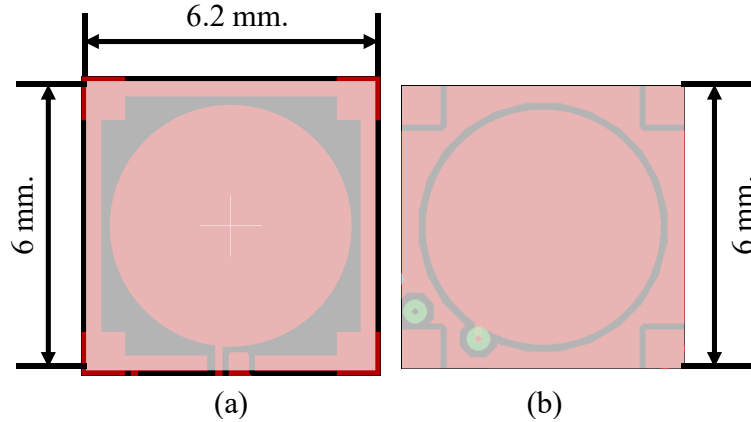


Figure 4.4 The comparison of the size of the surrounding pad of the two designs. (a) The diagram shows that the surrounding pad (red) for mounting the copper beryllium plate is slightly bigger than the plate (transparent white) in the current design. (b) While the corner pads were under the plate in the previous design used in the previous chapters.

Finally, the actual PCB with the thickness of approximately 0.230 mm was made. The size comparison of the surrounding pad and the copper beryllium plate can be seen in Figure 4.5.



Figure 4.5 The comparison between the size of the copper beryllium plate and the size of the surrounding pad can be seen; the plate was slightly smaller. Note that the distortion on the upper part of the image was due to the use of a magnifying glass used when the picture was taken.

4.2.1.2 Assembly and soldering

Regarding the placement of the copper beryllium plates onto the flexible PCB, a small amount of the lead-free no-clean solder paste SMD291SNL from Chip Quik Company was applied at the 4 corners of the surrounding pads on the PCB before a pair of tweezers was used to manually place each CuBe₂ plate as much as possible at the preferred location where the center of the plate aligns with the center of each circular electrode pad. We expected that this slight difference in the position of the copper plate which varied from one to another would slightly affect the force measurement of the sensor and it could be compensated by the calibration of the sensor.

Firstly, four copper plates were placed on the bottom side of the PCB and the PCB were put into a reflow oven to perform reflow soldering which the temperature inside the oven was controlled to follow a reflow solder's temperature profile provided by the solder paste supplier. The highest temperature inside the oven was controlled to be 250 °C. After the reflow solder was completed, the PCB was taken out after the cool down process finished.

Consequently, the same process was repeated to place another four copper beryllium plates on the top side of the PCB. On the top side, the solder paste was applied also on the area where the AD7147 chip and the capacitor chips would be placed. These three components also manually placed on the PCB as well. The PCB was through the reflow soldering process once again for mounting all the components on the top side.

Note that during the reflow soldering when the solder paste melts into a liquid form, the surface tension of the liquid solder would assist in repositioning the components into the balance position where the surface tension of the solder in all direction are equal. Therefore, for example, all the pins of the chip would be position correctly after the reflow process. However, the effect of surface tension did not significantly reposition the copper plate. This might be due to the fact that the amount of solder applied to the surrounding pad could not generate sufficient amount of surface tension to move the plate. However, the reason that only slight amount of solder paste was used for mounting the copper plate was to minimize the chance that the excess solder would potentially affect the initial capacitive gap even the surrounding pad was designed to be slightly bigger than the size of the plate.

The PCB after the reflow solder on both sides were done is shown in Figure 4.6. The excess solder can be seen at the four corners of each surrounding pad. However, it can be seen that only a small area of the surrounding pad that was not cover by the copper plate.

We were not sure whether that small expose area would be enough or not. This issue would be taken into consideration in the second prototype. The connection wires which compose of two power wires (3.3 VDC and ground) and two communication wires (SCL and SDA) could be seen as well.

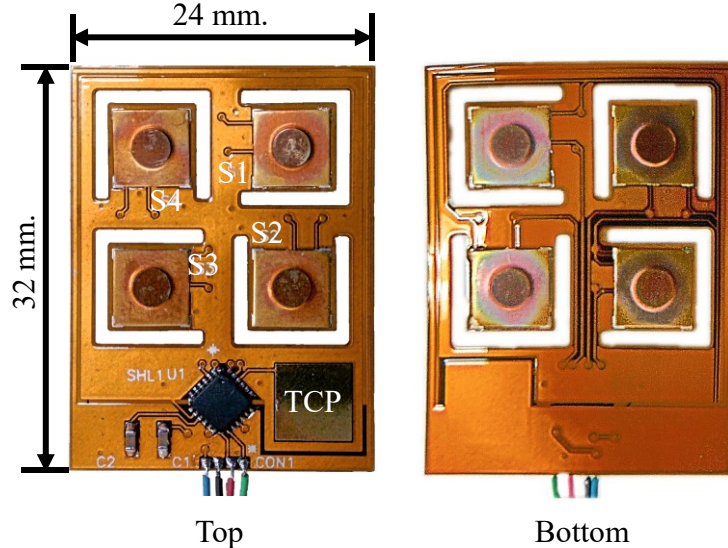


Figure 4.6 The sensor's PCB after all of the components were soldered to it. Note that there was a distortion from the magnifying glass in the picture.

This completed PCB was tested with a set of experiments prior to the inclusion of soft silicone rubber to make the final soft skin sensor. The experiments aimed for presenting the comparison result of several sensor's characteristics before and after the present of the soft silicone to show the effect that the compliant material could affect the performance of the sensor. The detail of the experiments including the result of the test would be discussed in Section 4.2.3.

4.2.2 Sensor molding

After the PCB was made and all the components were soldered onto the PCB, the PCB needed to be covered with compliant material in order to make a tactile sensor with a soft outer. Since the material selection is not in the current scope of interest, Ecoflex Supersoft 30 (from Smooth-On) is used due to its availability as a high strain material. It has a shore hardness of 00-30 which is softer than human skin. While the ideal hardness depends on the application and encountered force limits, softness, in general, is beneficial, yet causes problems for the sensor characteristics. Therefore, Ecoflex Supersoft 30 was purposely chosen, to test how the sensor works in a soft skin material. Note that Ecoflex Supersoft

10 is even softer with a shore hardness of 00-10, but has an oily film on the surface even after curing which could be problematic.

The Ecoflex Supersoft 30, see Figure 4.7, comes as two separate liquid silicone rubber substances which when mixed together at the ratio of 1 to 1 by weight or volume will solidify or cure at the temperature around 23 °C but not lower than 18 °C. Before left the mixed silicone to cure at the suggested temperature, it is recommended to degas the silicone – remove air bubbles from the mixed substance – in order to have a more homogenous silicone rubber.



Figure 4.7 The silicone rubber used to make the soft skin sensor. It is Ecoflex Supersoft 30 from Smooth-on and consists of 2 liquid substances which when mixed together create a soft silicone rubber with the shore hardness of 00-30.

Since the transducers portion needed to be tilted upward at an angle during the molding process, a method to maintain that angle is necessary to ensure that:

1. The desired angle is achieved.
2. All the bent segment will have approximately the same tilting angle.

For the bending angle, the 45-degree bending was chosen as the first candidate because it could provide a good balance of sensitivity for shear and normal forces. Therefore, 45-degree triangular supports made from the same silicone rubber were to be molded first with a 3D printed plastic mold.

4.2.2.1 Triangular support

In order to control the bending angle of the force transducers to be according to the proposed concept especially while the PCB is being submerged in the liquid silicone rubber, a support made from the same silicon rubber was designed to support the bent-up

transducer portion before the molding completed. Using the same material allows the cured silicone to floss together with liquid silicone which would be added in later on during the final molding process.

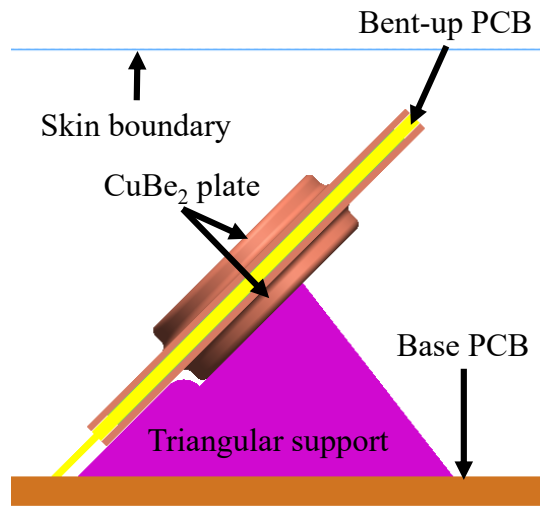


Figure 4.8 The cross-section view shows how the triangular support contact with the CuBe₂ plate. The bent-up PCB, the base PCB, and the skin boundary can be seen as well.

As can be seen in Figure 4.8, the cross section of the triangular support was designed so that it could support the bent PCB while giving least pressure to the copper beryllium plate mounted at the bottom side of the PCB. Excessive pressure on the bottom-sided copper plate could lead to extra pre-load of the sensor and the reduction in sensitivity and measurement range.

The negative version of the triangular support was used in designing the mold for the production of the support. The mold was 3D printed using the AGILISTA-3100, the 3D printer from Keyence. A transparent resin called AR-M2 was used as the main material while another resin AR-S2 which is water-soluble was used as a support material assisting when printing overhanging part. The first mold was shown in Figure 4.9 (a) and (b), it simply composed of twelve small grooves where the triangular supports would be made and a silicone buffer area above those grooves to ensure that sufficient amount of silicone would fill all the grooves. Moreover, when the silicone was first poured into the mold, air will trap inside the grooves while most of the more viscous silicone liquid stays in the buffer area; the silicone will slowly flow into the grooves afterward. The trapped air can be removed when the mold is put in a vacuum bag to perform the degassing process. The bag was connected to a generic vacuum cleaner which was used to depressurized the bag resulted in the gas inside the bag being removed.

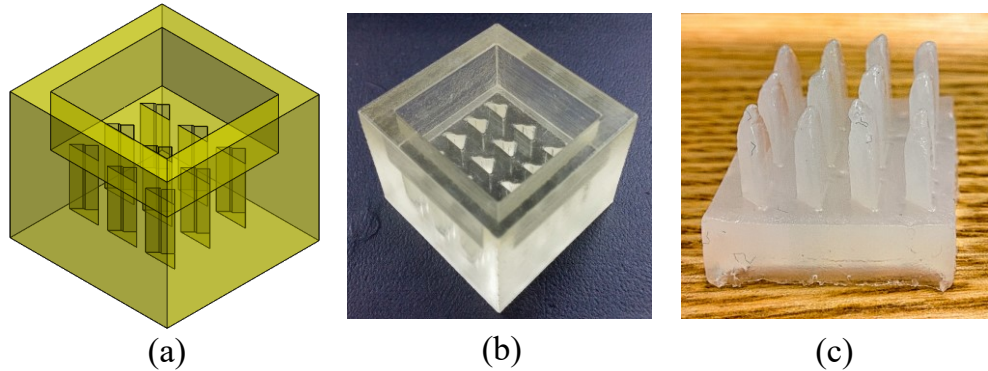


Figure 4.9 The first mold uses in making the triangular support silicone. (a) The CAD model of the mold. It mainly consists of 12 triangular grooves and buffer area above them. (b) The actual 3D printed mold. (c) The resultant silicone was not cured completely, especially at the tip even left outside the mold for several days.

However, as can be seen in Figure 4.9 (c) that the resultant silicone made from this mold was not completely cured even it was left exposed to air for several days, especially at the end of the triangular part where was in contact with the bottommost of the grooves when molding. It was suspected that the mold was not properly cleaned after 3D printed especially at the bottom of the grooves which is difficult to reach. A small amount of a material which we believed is the support material used when printing the mold could be seen at the bottom of the grooves.

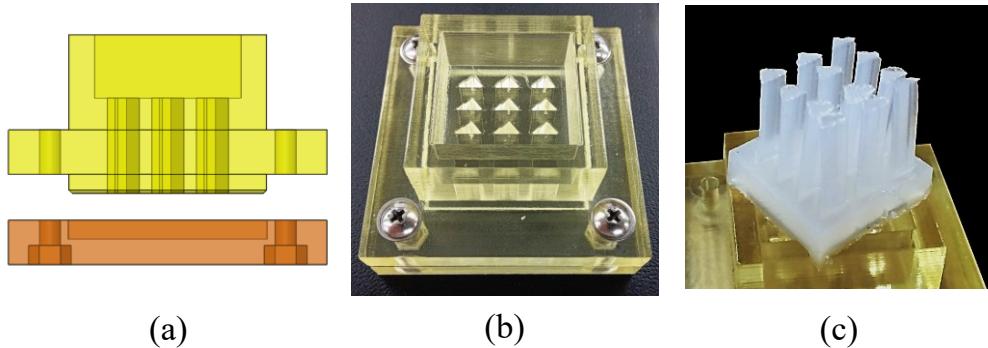


Figure 4.10 The second mold uses in making the triangular support silicone. (a) The CAD model of the mold which now composed of 2 pieces; the top and the bottom piece. (b) The actual mold when the 2 pieces were assembled together. (c) The resultant silicone shows perfect curing throughout the length.

Therefore, the mold was redesigned so that it is easier to be cleaned thoroughly especially the bottom of the grooves as shown in Figure 4.10 (a) and (b). The mold now composed of 2 pieces; the top part is similar to the previous design but the grooves go completely through the part, and the bottom part is used to prevent the leakage of the silicone when

it is poured into the mold. The two parts were mounted together by four bolts and nuts. The resultant silicone can be seen in Figure 4.10 (c), it can be seen that now the silicone was completely cured throughout its length. The silicone would be cut to the desired length of approximately 7 mm when it was used to support the bottom of the bent-up portion of the sensor's PCB so that it supported the whole width of the PCB.

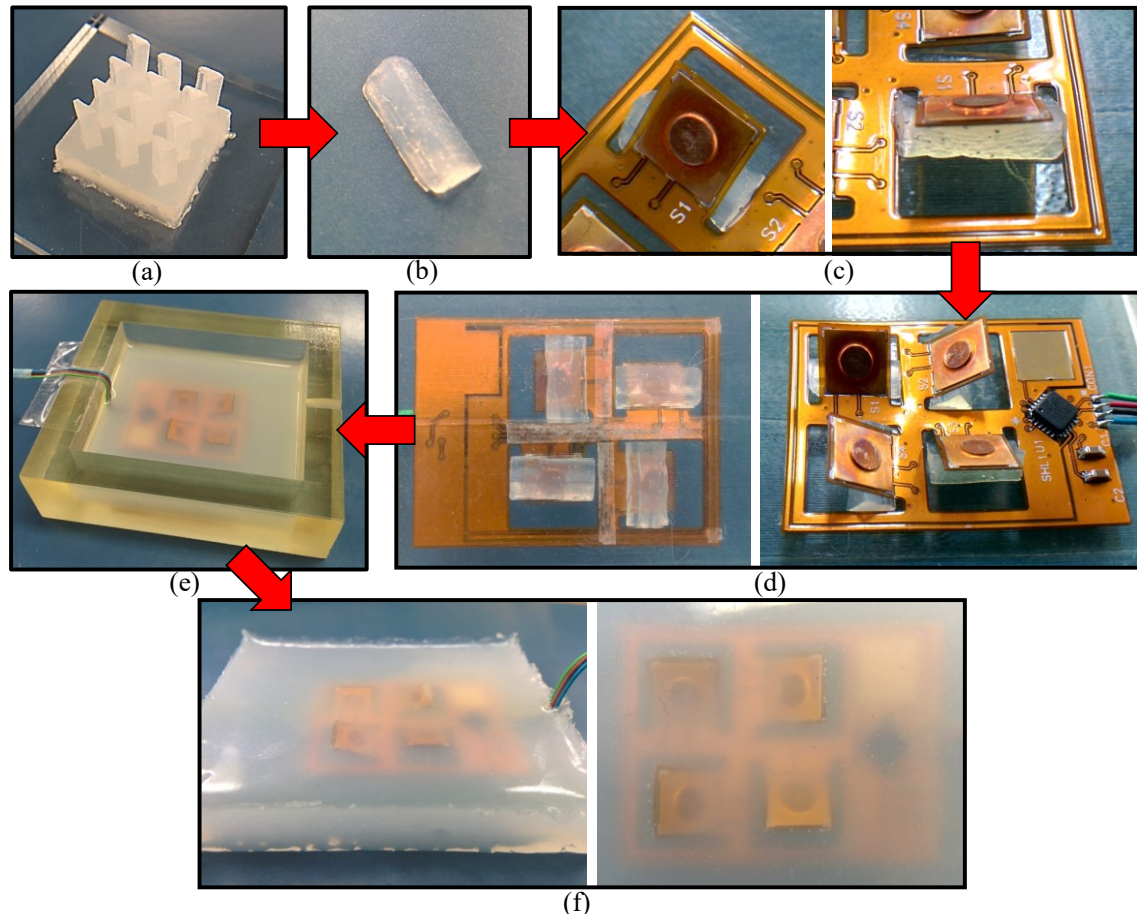


Figure 4.11 The molding process of the proposed skin sensor. (a) The molded triangular supports. (b) One triangular support. (c) The support is inserted under the tilted transducer. (d) The sensor after all of the transducers have been tilted up and supported by the triangular supports. (e) The sensor is being covered by liquid silicone rubber inside the 3D printed plastic mold. (f) The sensor after it has been taken out of the mold.

4.2.2.2 Sensor molding process

The molding process is shown in Figure 4.11. In order to bend the sensor units to approximately 45 degrees while being embedded in silicone, the 45-degree triangular supports made out of the same silicone rubber are molded first with a 3D printed plastic mold and then cut to the length of around 7 mm, see Figure 4.11 (a). The flexible PCB was positioned in another 3D printed rectangular plastic mold using thin double-sided

tape. The molded support was then inserted under the transducer as seen in Figure 4.11 (d). The bending angle was approximately controlled by a triangular silicone support and the angle after supported was only visually confirmed. After all the sensing elements are supported, the whole sensor is covered under liquid silicone rubber which is then allowed to cure for 4 hours, during which it also bonds to the triangular support silicone, see Figure 4.11 (e). Finally, as seen in Figure 4.11, the cured skin sensor with the thickness of 7 mm is taken out of the mold. The thickness of 7 mm was chosen in order to cover the whole transducer and have a roughly 2 mm thick layer of silicone on top to increase the robustness and softness (with possible detrimental effects on the sensor performance). The degassing process was done both when molding the triangular supports and the sensor. Future work will include the study of the influence of the bending angle on the measurements and the optimization of the bending angle, and the thickness of the silicone above the transducers will also be optimized for future work.

4.2.3 Experiments setup

A set of experiments was performed in order to test several characteristic of the sensor before and after the molding of the silicone rubber. The pre-mold and post-mold test were compared and the influence of the soft silicone on the sensor's performance was discussed. Furthermore, the tri-axial test was done after the molding to test the ability of the sensor in measuring 3D force. The result of this experiments was used afterward for further improvement in the second version of the sensor.

A Signal-to-noise ratio (SNR) test, accumulated load test and temperature drift test were done both before and after the sensor was covered in the silicone rubber (Section 4.2.4 and 0 respectively) to determine and compare the sensor characteristics. During all the experiments, the sensor was connected (via I2C bus) and powered by an Arduino Due, and the sensor readout was recorded at 40 Hz sampling rate onto an SD card mounted to the Arduino. The four force sensing units were left lying coplanar with the surrounding circuit board, as shown in Figure 4.6.

Figure 4.12 shows the measurement setup for the SNR test and accumulated load test. The former aimed to find the SNR value of the sensor while the later test aimed to determine non-linearity and hysteresis levels of the sensor. The known weights were placed on a weight placement plate with a $\varnothing 6$ mm shaft to push on the $\varnothing 3$ mm bump of each force sensing unit of the PCB which rested on the flat platform. The shaft went through a linear bushing which allows the weight to be transferred only in the vertical

direction. The weight of the weight placement plate and the shaft were also considered for the force acting on a transducer.

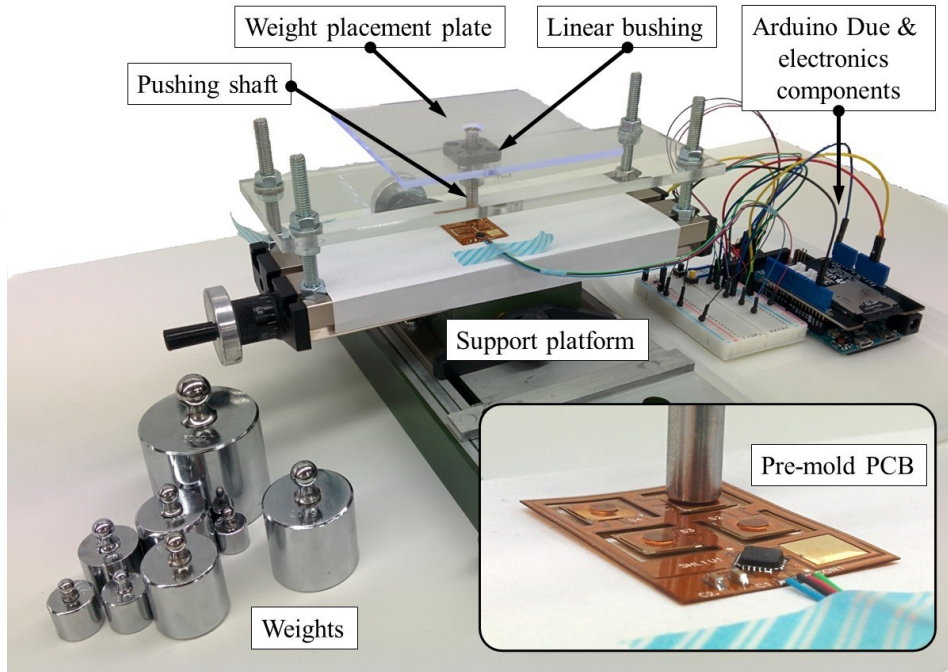


Figure 4.12 The experiment setup used in SNR and accumulated load test. It mainly consists of the set of weights, weight placement platform connecting with the pushing shaft. The shaft is supported by the linear bushing and used to exert the weight on each force transducer. The Arduino Due is used to record the sensor readout.

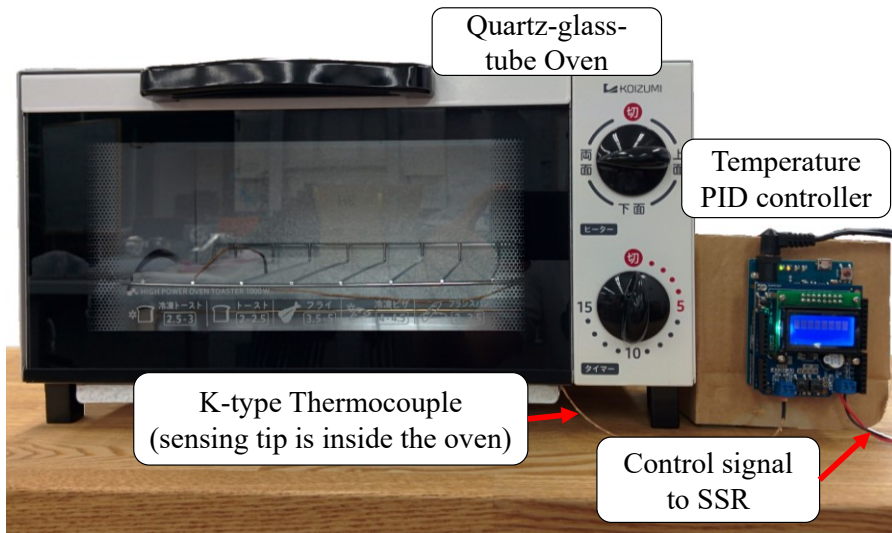


Figure 4.13 The experiment setup for the temperature test. It includes a quartz-glass-tube oven, a K-type thermocouple, a solid-state relay, and a temperature PID controller.

Since capacitive sensors are known to be affected by temperature changes and copper beryllium has a high thermal conductivity, a temperature drift test aimed to study the thermal drift occurring in the sensing unit and to test the feasibility of the temperature compensation pad to counteract the drift. A system as shown in Figure 4.13 was used to control the heating inside a quartz-glass-tube oven and cooling was achieved through the low room temperature. A simple temperature PID controller was used to control the oven to achieve a desired temperature via a solid state relay. As a reference, a temperature sensor (TMP102 from Sparkfun) and a humidity sensor (HIH6130 from Sparkfun) were placed only several millimeters away from the capacitive sensor.

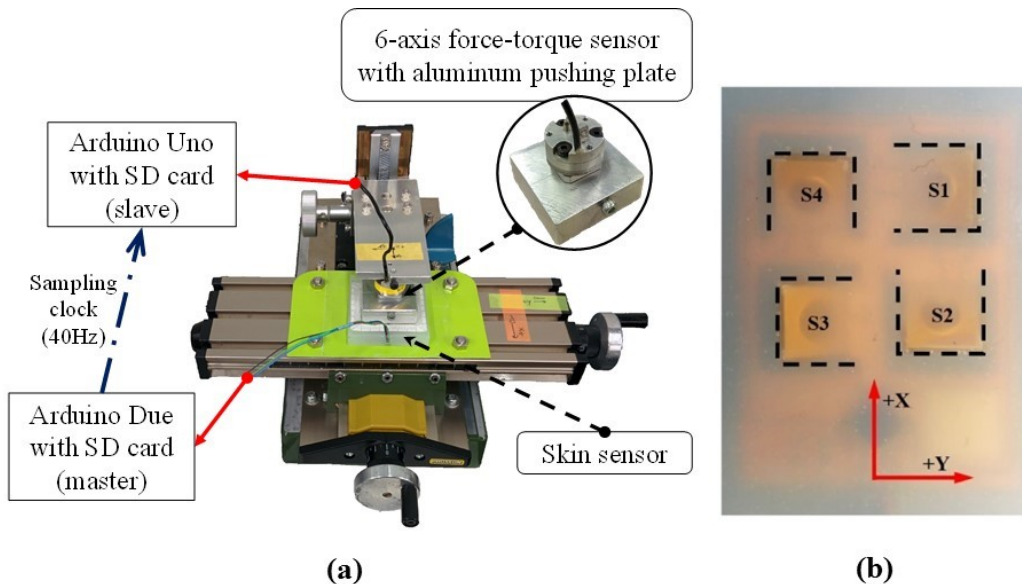


Figure 4.14 The experiment setup of the triaxial force test. (a) It consists of the 6-axis force-torque sensor, a $30 \times 30 \times 10 \text{ mm}^3$ aluminum pusher, and a manually-operated x-y-z-stage. (b) The 4 transducers and the axis of the load cell are shown. For example, +Y force will increase S₁ readout, but decrease S₃ readout.

Moreover, in order to verify the ability to detect and distinguish 2D shear forces of the skin sensor, the simple tri-axial force test was done. The setup as shown in Figure 4.14 consists of a manually operated 3-axis stage, a 6-axis force-torque sensor (Nano1.5/1.5 from BL Autotech) which was mounted to the z-axis of the stage, and an aluminum $30 \times 30 \times 10 \text{ mm}^3$ pushing plate which connected to the tool side (the force sensing part) of the Nano1.5/1.5 sensor to monitor the actual force exerted on the skin sensor. During the experiment, the actual force-torque data from the load cell and the readout of the skin sensor including environment parameters (temperature and humidity) were recorded by the Arduino Uno (slave) and Arduino Due (master) with a synchronized sampling rate of

40 Hz. Two microcontrollers were used because of the different voltage level of the skin sensor (3.3 V) and the 6-axis force-torque sensor (5 V). The synchronization of the two sensor readings was verified with an oscilloscope.

4.2.4 Pre-mold experimental result

4.2.4.1 SNR test

In this test one sensor unit was loaded with a certain fixed weight per trial. The weights and the weight placement plate were manually placed on a sensor knob to transfer the force onto the force sensing unit for approximately five seconds, and the response of the sensor was recorded. Four weight sums were used in this experiment, which were 50 mg, 250 g, 500 g, and 1250 g. For example, the 250 g consisted of 45 g for the weight placement plate and the shaft, and 200 g and 5 g weights. The 50 mg is a special case and was placed directly on the knob of the sensor unit, as we wanted to record the sensor response to our smallest available weight, not including the weight of the shaft and weight placement plate. Ultimately, the sensor values before and during loading were used to obtain the SNR, which was calculated according to Eq. 2 or 3.

The results for all transducers can be found in Table 4.1. The value of S_1 drops to zero under 1250 g load which corresponds to overload. Despite being overloaded, the sensor still functions normally afterward, which indicates that the proposed sensor is able to withstand excessive load without losing its functionality. The hard limits of the sensor should make it robust to overload, however, more overload tests will be performed in the future.

Table 4.1. The value of S_1 drops to zero under 1250 g load which corresponds to overload. Despite being overloaded, the sensor still functions normally afterward, which indicates that the proposed sensor is able to withstand excessive load without losing its functionality. The hard limits of the sensor should make it robust to overload, however, more overload tests will be performed in the future.

The SNR increases with higher load, as expected. Figure 4.15 shows the exemplary step response of S_2 when loaded with 250 g, with $\sigma_u=0.68$. As a result, the value of SNR is 3627.24 or 71.19 dB, which is relatively high for this kind of sensor, compared for example to the SNR of 315 (49.97 dB) found in [24] at the load of approximately 306 g. Moreover, as can be seen as an example in Figure 6, the force sensing transducer has a high level of sensitivity and can apparently sense the load of 50 mg.

The value of S_1 drops to zero under 1250 g load which corresponds to overload. Despite being overloaded, the sensor still functions normally afterward, which indicates that the proposed sensor is able to withstand excessive load without losing its functionality. The hard limits of the sensor should make it robust to overload, however, more overload tests will be performed in the future.

Table 4.1 The comparison of the SNR_{dB} value of each sensing element the molding.

| Weight (g) | S ₁ | S ₂ | S ₃ | S ₄ |
|------------|----------------|----------------|----------------|----------------|
| 0.05 | 13.78 | 18.62 | 25.93 | 17.73 |
| 8.7 | | | | |
| 250 | 78.78 | 71.19 | 70.71 | 61.87 |
| 500 | 88.75 | 76.90 | 76.46 | 73.63 |
| 1250 | | 85.78 | 89.04 | 86.32 |

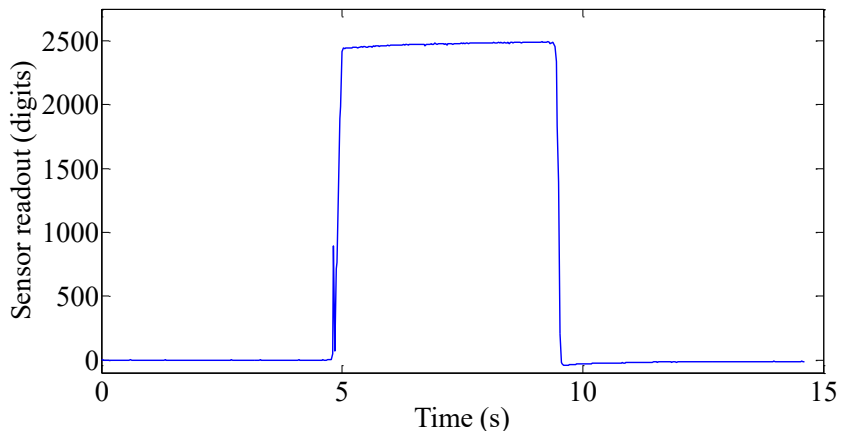


Figure 4.15 The response of S₂ under 250 g of weight.

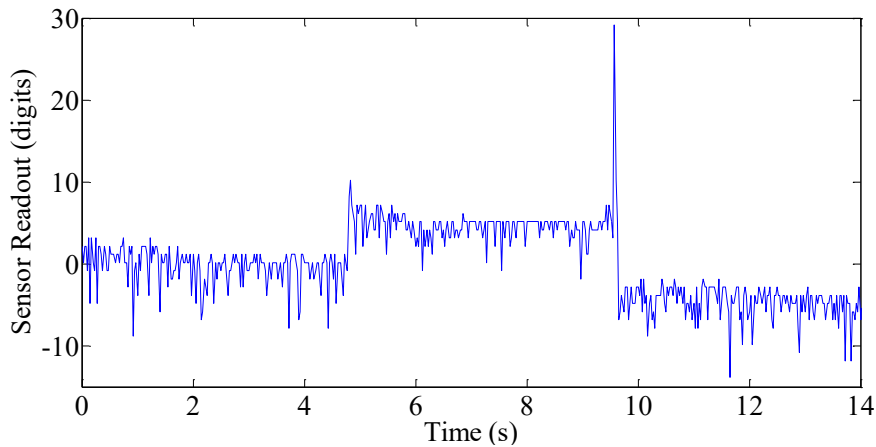


Figure 4.16 The response of S₃ to the load of 50 mg.

4.2.4.2 Accumulated load test

The accumulated load test used weights starting from placing nothing on the weight placement plate which was previously put on the knob of one force sensing unit (step 1, 45 g), and steadily adding more weights as described in Table 4.2 with five seconds interval until the total weight reaches 1253 g (step 17), then removing them one by one in the opposite order, again with 5 seconds interval. This test was conducted to observe the relationship between the weight and the sensor readout both when the sensor is being loaded and unloaded.

Table 4.2 The list of weights which will be put on a single force sensing unit during the accumulated load test at each step. The loading sequence goes from 0 to 17 and the unloading sequence goes from 17 to 0.

| Step | Weight (g) | Step | Weight (g) |
|------|------------|------|------------|
| 0 | 0 | 9 | 133 |
| 1 | 45 | 10 | 153 |
| 2 | 46 | 11 | 203 |
| 3 | 48 | 12 | 253 |
| 4 | 53 | 13 | 353 |
| 5 | 63 | 14 | 453 |
| 6 | 73 | 15 | 553 |
| 7 | 93 | 16 | 753 |
| 8 | 113 | 17 | 1253 |

Figure 4.17 shows the sensor readout of S_3 . For each step, the sensor measurement slowly and gradually changes, which is most obvious for step 17, for which also the highest change between steps occurs (500 g). As can be expected, some hysteresis can be observed. In particular, for the 753 g load, there is a difference of 853 digits when comparing loading and unloading which corresponds to about 42 g according to the calibration with quadratic curve fitting.

The response of S_3 to both the loading and unloading sequences is shown in Figure 4.18. Also, the quadratic approximation lines for the loading and unloading are drawn to show the nonlinear behavior of the sensor. The results for the other sensor units (S_1 , S_2 , and S_4) were similar to the one shown here. Moreover, the hysteresis can also be seen. By using Eq. 4, the hysteresis percentage of S_3 was 0.37% of the maximum load of 1253 g.

$$\text{Hysteresis\%} = \left| \frac{(F_{mu} - F_{ml})}{(F_{max} - F_{min})} \right| \times 100\% \quad (4)$$

Where F_{ml} and F_{mu} were the converted force values of the loading and unloading cycles taken at the midpoint weight of $(1253 \text{ g} - 0 \text{ g})/2 = 626.5 \text{ g}$.

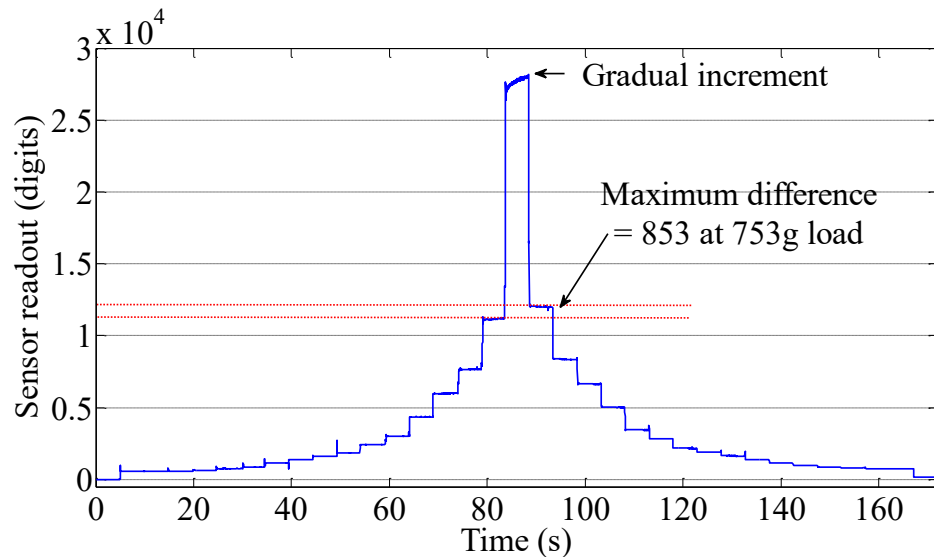


Figure 4.17 The relationship between time and sensor readout of S_3 during the accumulated load test before molding.

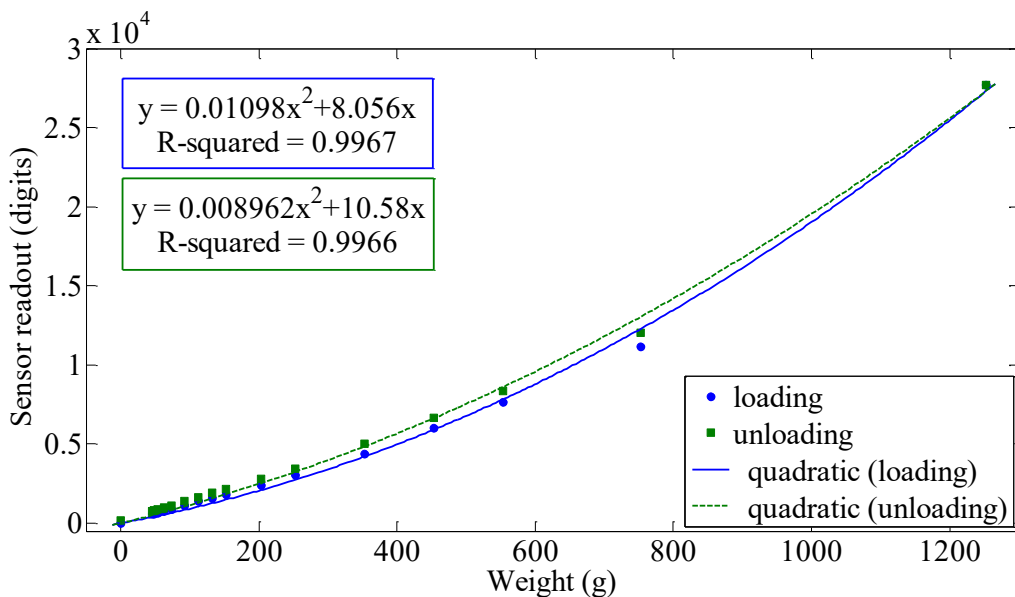


Figure 4.18 The relationship between the load and sensor readout of S_3 before the molding and its quadratic approximation line of both loading and unloading sequences. The values shown in the blue box are for loading and those in the green box are for unloading.

4.2.4.3 Temperature test

The circuit board was exposed to varying temperatures, starting from 15 °C and gradually increased to 40 °C, and then brought back to 15 °C. During this process, the values of S₁, S₂, S₃, S₄, and TCP were recorded.

Figure 4.19 shows the plot of the thermal drift found in all sensing units, TCP, and the actual temperature near the sensor as measured with the TMP102 temperature sensor. It can be seen that the measurements of the force sensing units and the TCP follow the profile of the temperature (purple). The result shows that the measurements of the force sensing units and the TCP follow the profile of the temperature. Therefore, the drift of the TCP can be used to cancel the thermal effect on the force sensing transducers by using Eq. 5,

$$\hat{S}_i(t) = S_i(t) - K_i \times \text{TCP}(t) \quad (5)$$

where $\hat{S}_i(t)$ is the value of the sensor i at time t after being compensated, and $S_i(t)$ is the raw value recorded from the same sensor at time t. TCP(t) is the value taken from the TCP at time t. Lastly, K_i is the gain factor estimated for calibration purposes, set differently for each sensor.

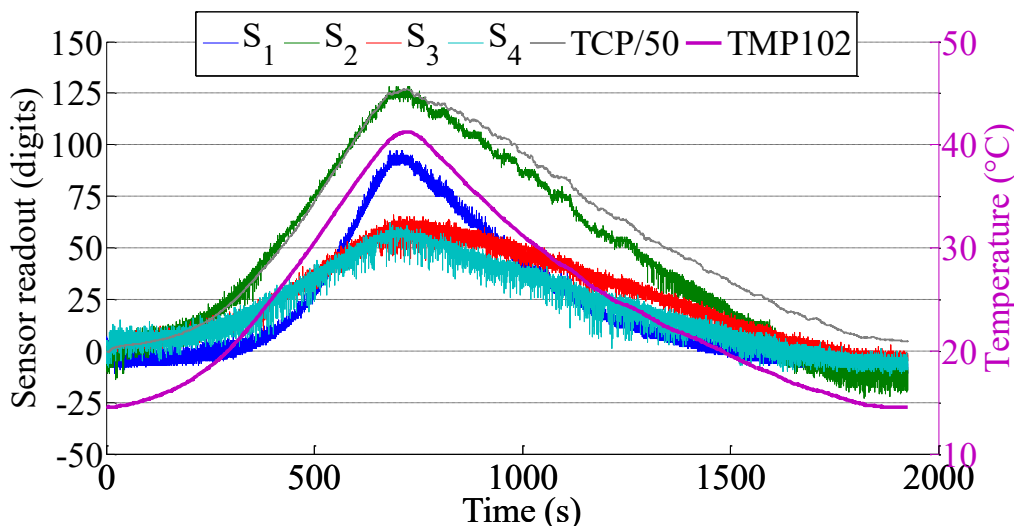


Figure 4.19 The thermal drift of all sensing units before the molding including TCP (gray, scaled down by 50) are shown together with the actual temperature (purple) sensed by the TMP102 sensor.

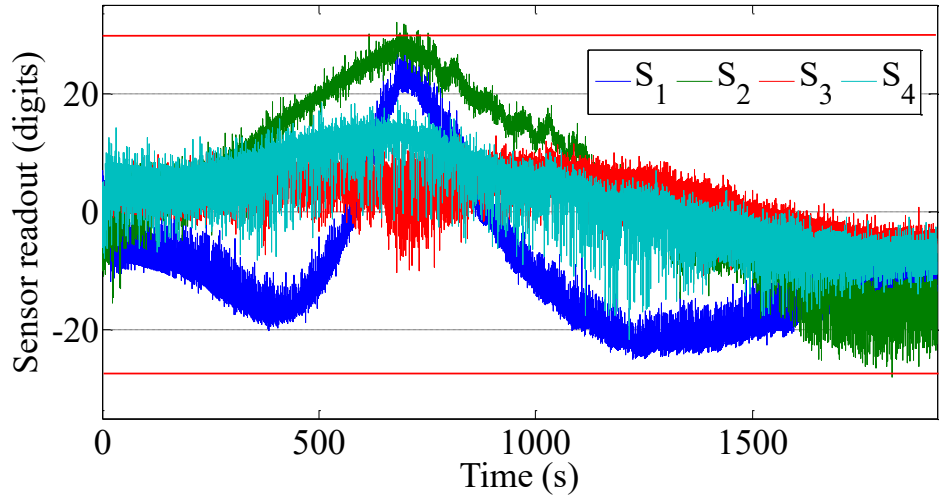


Figure 4.20 The sensor readout of all four transducers after the temperature compensation (pre-mold).

The result of the compensation can be found in Figure 4.20, showing that the thermal drift can be successfully suppressed from a band of around 150 digits (Figure 4.19, S2 [from +125 to -25]) into ± 30 digits or less, which is very low considering the sensitivity and range of the sensor, as shown previously. This method has been used successfully previously [20][63]. The compensation was successful; the drift was reduced from 10g to 5g. Post-mold experimental result

4.2.4.4 SNR test

This test was done in the same fashion as in Section 4.2.4.1 but the weights of 8.7 g, 250 g, 500 g, and 1250 g were used in this test. The 50 mg weight was replaced by the 8.7 g shaft because the 50 mg weight could not be sensed by the molded sensor. Furthermore, with the shaft, the weight could repeatedly be placed in the same location.

All results are shown in Table 4.3 with the comparison with the pre-mold SNR results. As expected, the SNR are higher when the load increases, and the SNR values are lower after the molding compared to before the molding. This might be due to the fact that the load that was applied on the sensor surface above a transducer was distributed not only to the element underneath but also to the surrounding silicone and to the other sensing elements as well as can be observed in Figure 4.21. This is further supported by the fact that the post-mold S₁ could sense the load of 1250 g.

Table 4.3 The comparison of the SNR_{dB} value of each sensing element before and after the molding.

| Weight (g) | S ₁ | | S ₂ | | S ₃ | | S ₄ | |
|------------|----------------|-------|----------------|-------|----------------|-------|----------------|-------|
| | Pre | Post | Pre | Post | Pre | Post | Pre | Post |
| 0.05 | 13.78 | N/A | 18.62 | N/A | 25.93 | N/A | 17.73 | N/A |
| 8.7 | N/A | 34.47 | N/A | 22.42 | N/A | 20.72 | N/A | 23.32 |
| 250 | 78.78 | 54.45 | 71.19 | 48.89 | 70.71 | 54.97 | 61.87 | 48.84 |
| 500 | 88.75 | 61.83 | 76.90 | 56.89 | 76.46 | 62.42 | 73.63 | 56.28 |
| 1250 | N/A | 78.98 | 85.78 | 75.43 | 89.04 | 73.99 | 86.32 | 78.84 |

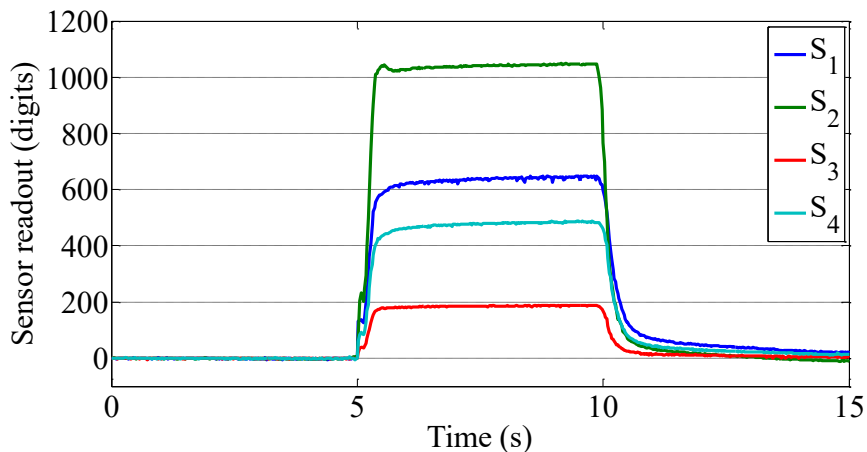


Figure 4.21 The post-mold step response of all sensing elements when the load of 250 g is applied to S₂. It can be seen that the load is also sensed by the surrounding sensor units.

4.2.4.5 Accumulated load test

This test was performed in the same fashion as in Section 4.2.4.2. The weights were sequentially added and taken off in a LIFO fashion following the sequence as shown in Table 4.2.

Figure 4.22 shows the sensor readout of S₃. At each step, the sensor readout slowly and gradually changes, most obviously at step 17, where the highest weight change between steps occurs (500 g). Comparing to Figure 4.17, the transient response time of the molded sensor was drastically longer which we expect is due to the viscoelasticity of the silicone. Again some hysteresis can be seen especially at the 753 g load of around 41 g difference

when comparing loading and unloading. The difference in gram was obtained in the same fashion as Section 4.2.4.2.

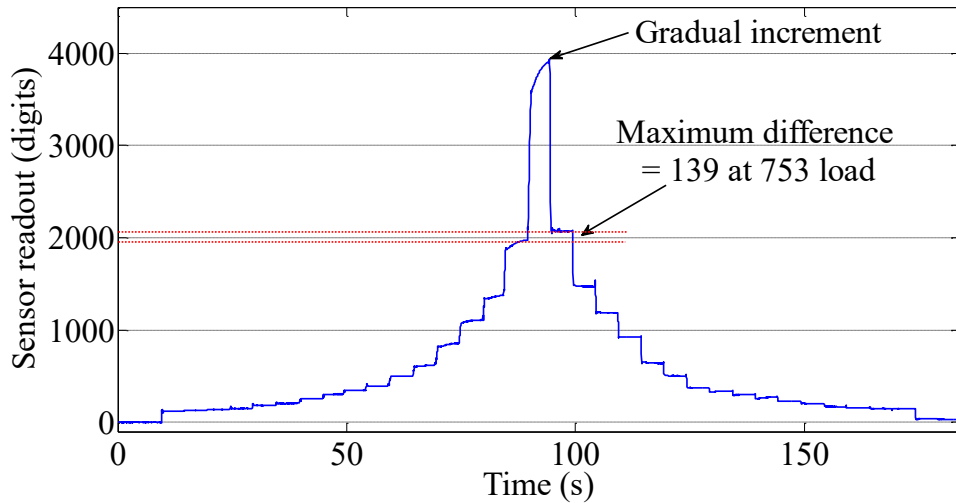


Figure 4.22 The relationship between time and sensor readout of S₃ during the accumulated load test after molding.

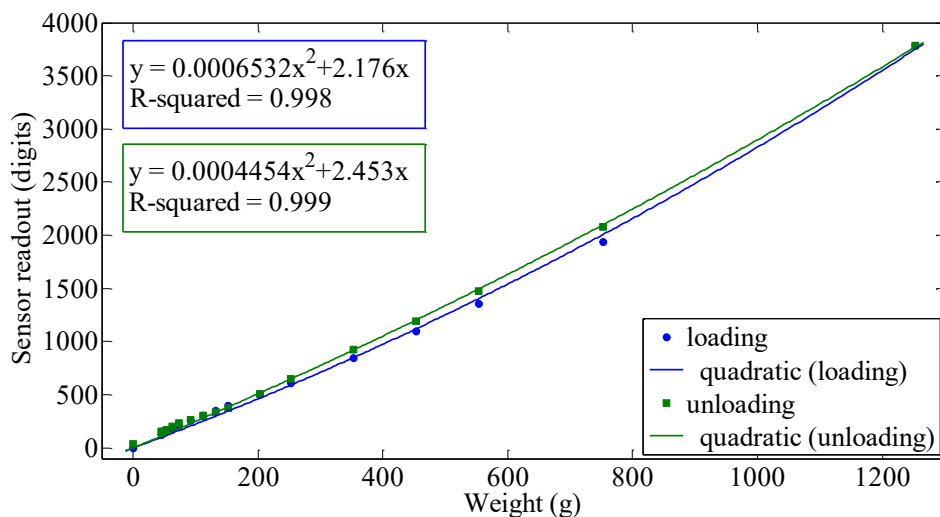


Figure 4.23 The relationship between the load and sensor readout of S₃ after the molding and its quadratic approximation line of both loading and unloading sequences. The values shown in the blue box are for loading and those in the green box are for unloading.

The response of S₃ to both the loading and unloading sequences is shown in Figure 4.23. Comparing to Figure 4.18, it can be seen from the higher R-squared values that the result here is closer to the quadratic approximation lines both when loading and unloading. Moreover, it can be seen that the response after the molding is about 7.5 times less

compared to pre-molding. This is due to the fact that the load is distributed to the silicone rubber and the other sensors as explained above and shown in Figure 4.21.

Furthermore, by using Eq. 3, the hysteresis percentage of S_3 was 1.27% of the maximum load of 1253 g while that of the pre-mold was 0.37%. Nevertheless, we expect that the hysteresis (and also the difference between the transducers) can be reduced with an improved version of the PCB, which will be discussed later on.

4.2.4.6 Temperature test

With the same method used in Section 4.2.4.3, the result of the experiment is shown in Figure 4.24. By using Equation (3) but with new constants K_i , the compensation of the thermal drift can be accomplished as shown in Figure 4.25. The drift can be reduced from around 260 g to 54 g.

Compared to the pre-mold result, the drift band is bigger but is also attenuated more significantly as well. The cause of the higher residual drift (in digits as well as in gram) might be the force transducers located higher to the surface than the TCP, which was still located at the bottom of the skin. This could lead to a different temperature distribution in those 2 locations. Nevertheless, the TCP measurements are more related to the sensor measurements S_1 , S_2 , S_3 and S_4 than the TMP102 temperature sensor just a few millimeters away from the sensor. Further possibilities of drift compensation will be discussed in the future work section. Finally, the humidity sensor measurements of both pre- and post-mold are nearly identical and are inversely proportional to the temperature.

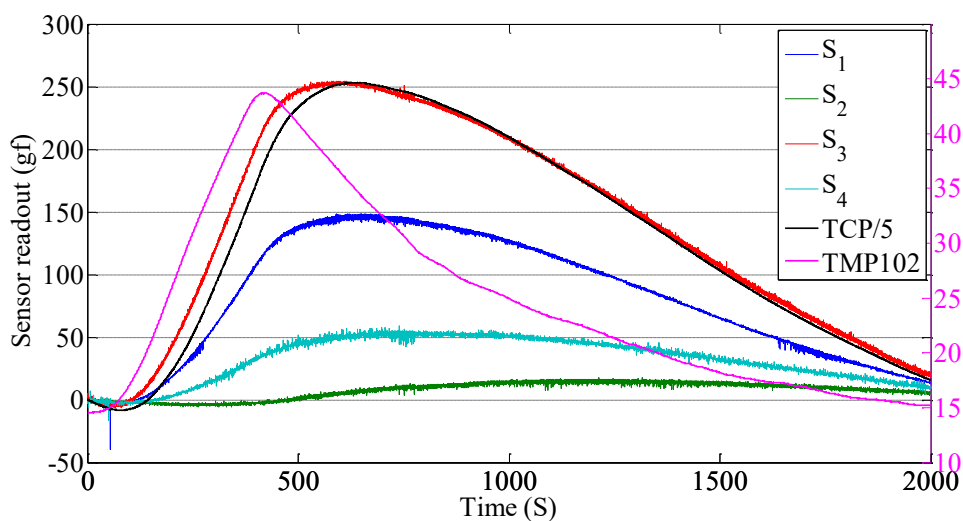


Figure 4.24 The thermal drift of all sensing units after the molding including TCP (gray, scaled down by 5) are shown together with the actual temperature (purple) sensed by the TMP102 sensor.

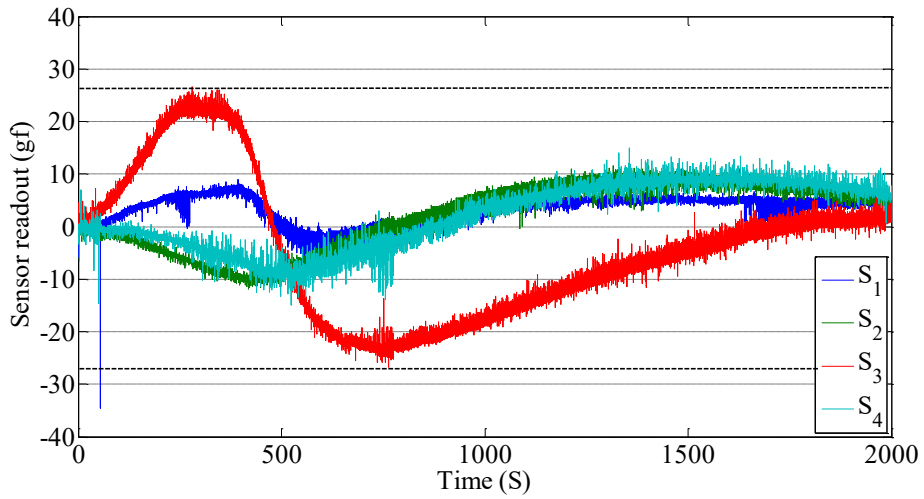


Figure 4.25 The sensor readout of all four transducers after the temperature compensation (post-mold).

4.2.4.7 Triaxial test

The experiment was conducted by first manually moving the z-axis stage down until the plate pushed the skin sensor with the magnitude of approximately 800 g, as measured by the load cell. After that, the x-y stage was displaced one axis at a time by 2 mm to generate shear force at the sensor surface while the z-axis was locked in place. Figure 4.14 (b) shows the relationship between the shear force in each direction and the 4 capacitive sensor units. For example, a force created by moving the x-y stage in +Y direction should increase the sensor readout of S_1 but decrease that of S_3 .

The result of this experiment is shown in Figure 4.26, which shows that the direction of the applied shear force could be identified by the proposed sensor. For example, when there was a force acting in +Y direction, the readout of the transducers S_1 increased while that of S_3 decreased, as seen in Figure 4.26 (c). S_2 and S_3 increased slightly corresponding to the increment of the force in Z-axis. However, the sensor measurements resulting from shear in +X direction did not correspond to our expectations, and this phenomenon has to be further investigated.

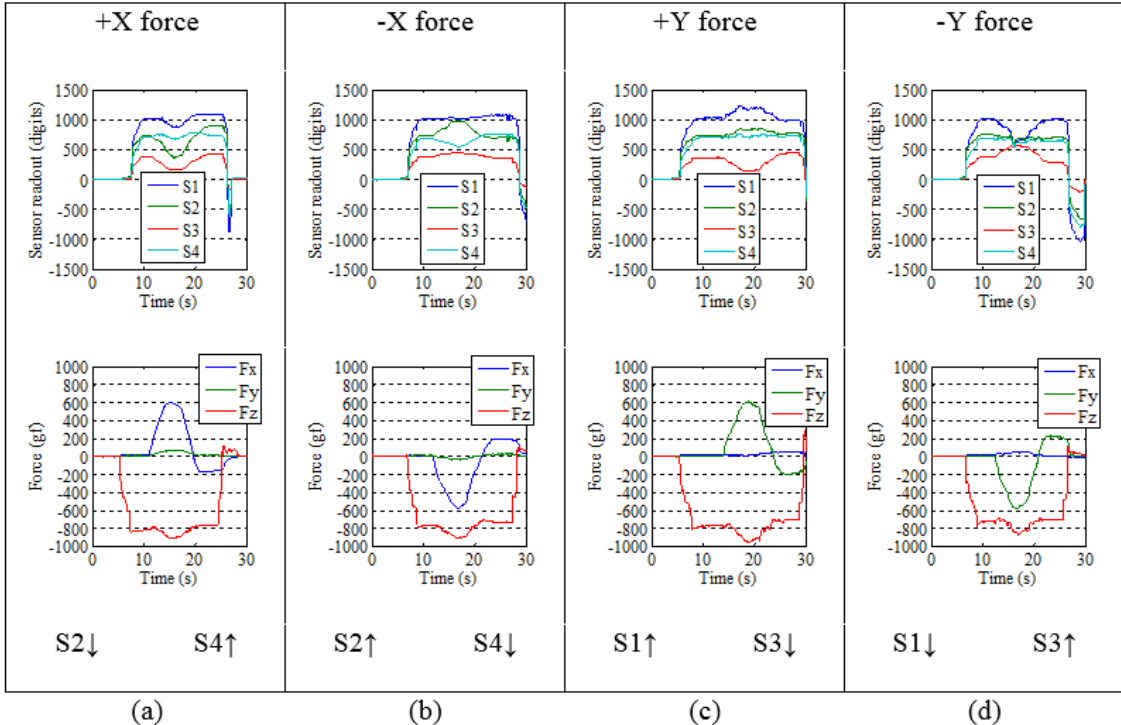


Figure 4.26 The sensor readouts when applying a shear force in different directions.

S_1 , S_2 , S_3 and S_4 are the 4 sensor units of the capacitive sensor. F_x , F_y and F_z are measured with the 6-axis force-torque sensor.

4.2.5 Discussion

Section 4.2 presents the first design and experimental evaluation of a novel capacitive triaxial skin force torque sensor. The implementation was successful, and should make it possible to measure distributed force vectors directly at the impact sites. The included digitization of the sensor signals reduces the amount of necessary wiring, which is important for the installation on a robot. Tests before and after the molding process were performed. The following aspects were evaluated:

1. The main novelty is the tilted capacitive transducers with copper beryllium that should enable to measure the tangential forces acting on the sensor. First experiments have shown the capability to differentiate the shear forces.
2. Even after the molding, the sensor has a relatively high SNR, comparable to the one published in [24]. In our experiment, the hysteresis was limited within 4% of the maximum force after the molding when covered with a 7 mm-thick layer of Ecoflex Supersoft 30 silicone rubber.
3. The temperature compensation pad enables to limit the effect of temperature changes on the sensor measurements. To further minimize the influence of the temperature on

the sensor measurements, low-frequency low-amplitude signals can get filtered out, similar to [21].

4. The molded version of the sensor introduces cross-talk, has higher hysteresis and decreases the sensitivity of the sensor. Such characteristics are to be expected, due to the silicone, and are not catastrophic for our intended use in a humanoid robot, especially as no good alternatives are currently available to measure distributed force vectors in a soft skin. The source of the hysteresis in the unmolded sensor is relatively small, but will be further investigated and can potentially be reduced with an updated version of the flexible PCB or the copper beryllium plates. For the molded version, the hysteresis and crosstalk can only be reduced to a certain extent with the choice of different viscoelastic materials while maintaining the softness of the skin, which is important for the safety property of the skin. Moreover, the thickness of pure silicone above the sensor units could be reduced (it is currently about 2 mm), but the robustness of the sensor has to be taken into account. The sensitivity/range of the sensor units can be changed by the thickness of the copper beryllium plates, and thinner plates can be used to adjust the sensitivity/range suitable for our intended use in a humanoid robot.

Further experimental evaluations were necessary. In particular, an improved version of the experimental setup would make it possible to better test the sensor response to shear forces (including twist around the z-axis, which has not been tested so far) and acquire the calibration matrix. A voice coil motor would be used to enable testing with consistent force input and also for frequency response testing. Several instances of the same sensor will be produced and tested, to obtain more comparative results.

The production procedure should be improved. Currently, the components were soldered manually, and the size of the solder pads for the copper beryllium plates might be too small, so a slight excess of solder could affect the sensor characteristics. Using an improved PCB or a metal stencil could help distribute the solder equally. Furthermore, a more reliable method was needed to ensure the bending of the sensing units to a 45-degree angle. In general, the production process currently involved a lot of manual work, and should be further automatized to make the production cheaper and more reliable.

4.3 Implementation: Version 2

According to the implementation and the experimental result of the first version, the improvement was done in the second version in several aspects. Namely,

further increment in the area of the surrounding pad to ensure sufficient space for the excess solder used in mounting the copper beryllium plate to the PCB,

the regulation of the solder paste's quantity by using a stencil, especially to solder the CuBe₂ plates on the PCB with a constant amount. This also reduces the difficulty and the time of the production as well.

the addition of a copper pattern between the center capacitive electrode and the surrounding pad in order to ensure the present of the support structure of the CuBe₂ plate to control the initial gap of the capacitive sensor,

repositioning the four transducers so that their centers form a square with respect to the measurement axis of the sensor after the 45-degree bending,

further stray capacitive noise attenuation procedure by surrounding the bent-up transducer with grounded conductive ink to prevent the noise from entering the side of the PCB and disturbing the measurement when a metal part is near the sensor,

the bending angle confirmation method,

the improvement in sensor molding in order to prevent the curved edge due to the effect of surface tension on the open-top mold,

and the improvement in the experimental setup to have a force control pusher.

4.3.1 Circuit redesign

The major points of improvement in this second version of the skin sensor were the inclusion of the support pattern to maintain the no-load gap of the capacitive sensor, the enlargement of the surrounding pad area, and the repositioning of the four transducers so that their center form a square after the 45-degree bending.

4.3.1.1 Supportive triangular copper patterns

For the additional support patterns which located between the center capacitive electrode and the surrounding pad as can be seen in the second version design of Figure 4.27, this is due to the fact that there was no such support provided in the area in the design of the first version which can be seen in Figure 4.28 (a). It could lead to the unreliability of the initial gap between the CuBe₂ plate and the center electrode pad in no-load condition; the gap would depend only on the amount of the solder paste applied. Moreover, since the surrounding pad was only 0.1 mm bigger than the CuBe₂ plate on each side and there was no regulation in the amount of the solder paste, there could be a high possibility that the

initial gap of each capacitive sensor would varied remarkably. In the worst case, it could lead to the contact of the plate and the pad which resulting in a zero capacitance and the malfunctioned sensor. The effect of adding the triangular pattern into the PCB can be seen in Figure 4.28 (b) where the elevation of the area can be seen. According to the PCB manufacturer, the elevated area is approximately 0.046 ± 0.01 mm. higher from the center electrode and the surrounding pad.

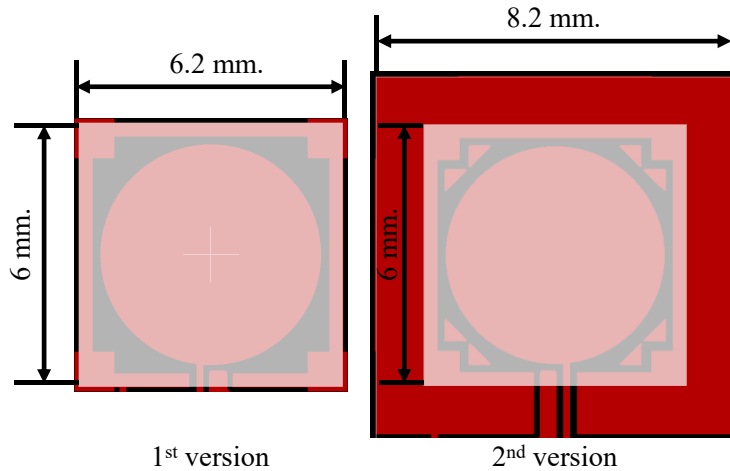


Figure 4.27 The comparison between the size of the surrounding pad of the first and the second version. Note the larger surrounding pad and the eight triangular patterns were added in the second version.

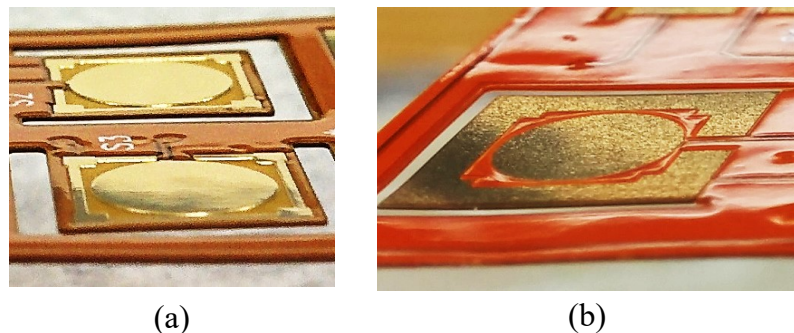


Figure 4.28 The comparison of the CuBe₂ support area of the first and second version. (a) The lack of the support area in the first version. (b) The present of the support area by adding the triangular patterns into the area.

4.3.1.2 Further enlargement of the surrounding pad

For the surrounding pad, it was only 0.2 mm bigger than the copper beryllium plate in the first version. Even slight extra solder could affect the no-load capacitive gap of the sensor. Therefore, the surrounding pad of the second version was increased to 8 mm. which made it 2.2 mm. bigger than that of the first version, see Figure 4.27. This was done to ensure

that the excess solder would spread on the wider pad and the height of the copper beryllium would not be affected by that excess solder. Indeed, this increment in the surrounding pad would increase the overall size of the PCB but since the miniaturization of the PCB was not the most important priority at the moment, especially when comparing to the finding of the appropriate size of the surrounding pad which is sufficient for the amount of solder used.

4.3.1.3 Repositioning of the transducers

This repositioning is to make all the transducers align themselves so that their centers are at the corners of a square after they are bent up 45 degrees when seeing the sensor from the top. The square is aligned to the x and y reference axis of the sensor used in determining the direction of the sensed force. The comparison between the position of the transducer of the first and the second version can be seen in Figure 4.29. It can be argued here that this repositioning might lead to a better shear force sensing (considering that the squares are in the same size) since now the center of all transducers are forming a square parallel with the axis of the sensor. The size comparison between the PCB used in the first version and the second version can be seen in Figure 4.30.

Finally, the actual PCB of the second version sensor can be seen in Figure 4.31. The triangular patterns which surrounded the center electrode pad can be seen. The surrounding pad was now becoming bigger compared to the previous design as well.

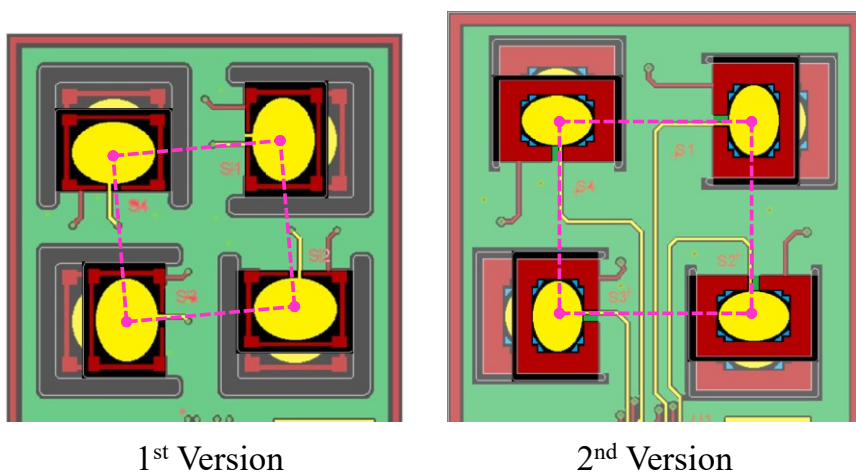


Figure 4.29 The comparison of the position of the transducers between the first and the second prototype. The magenta square shows how the transducers align.

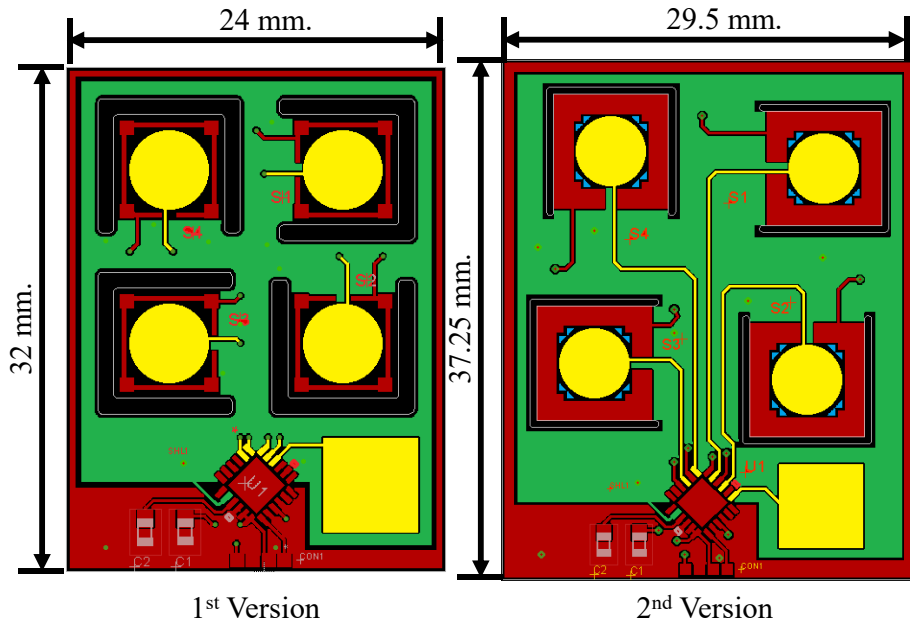


Figure 4.30 The comparison between the design of the first and the second version.
It shows the capacitive electrodes and their traces (yellow), the ACShield area (green), the ground area (red), and the triangular patterns (light blue).

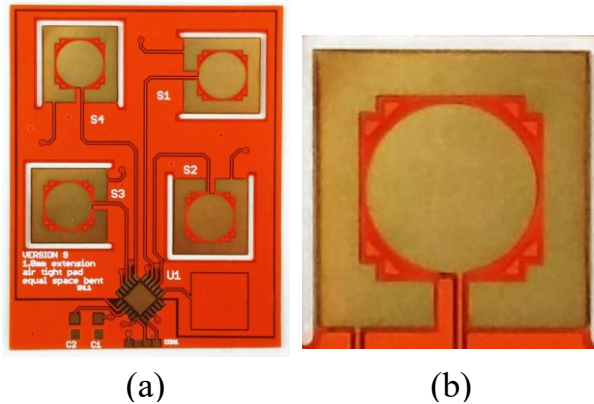


Figure 4.31 The actual PCB of the second version. (a) The overall view of the PCB.
(b) The close-up view of a bent-up portion; the triangular patterns can be seen.

4.3.2 Improved production process

In the previous version of the sensor, the amount of solder was not regulated and the copper beryllium plates were manually placed on the PCB. The uncontrolled amount of solder could potentially lead to huge variation in sensitivity and measurable range from a transducer to the next. As a solution, a stencil was used to make the amount of solder consistent. A vacuum nozzle was used to pick up and steadily position the copper plate to the desired location. Furthermore, the generic vacuum cleaner cannot generate sufficient power for an effective degassing which can be seen from the leftover bubble

when the silicone is cured. A vacuum chamber using a proper vacuum pump is built and used instead in the production of the version 2 sensor.

4.3.2.1 Stencil

The stencil made from 50 µm thin stainless steel is shown in Figure 4.32. It composes of two sets of patterns; one is for the top side and the other is for the bottom side of the PCB. Stencils are commonly used to apply solder paste to desired positions in the electronics industry. The amount of solder is controlled by the thickness of the stencil and the width of each pattern (called aperture).

Furthermore, PCB support blocks as shown in Figure 4.33 were 3D-printed to use together with the stencil. Each has four locating pins which fit into the four holes on the stencil in order to hold the stencil and the support block together while the solder paste is being applied on the PCB. The center of the block where the PCB would be located has grooves for assisting in positioning the PCB in the correct location. Five holes at the center are filled with a reusable clay-like adhesive called Blue-Tack (from Bostik) which is just strong enough to hold the PCB in place but still easy to remove after the solder paste is applied on the PCB. Moreover, as can be seen in Figure 4.33 (b), there are four shallow holes located in the position where the bumps of the transducers on the bottom side of the PCB are soldered. These holes on the support block are slightly bigger than the bumps on the transducers; they are to avoid applying excessive force on the bumps when the stencil is pushed by the squeegee use in pasting the solder into the apertures of the stencil.

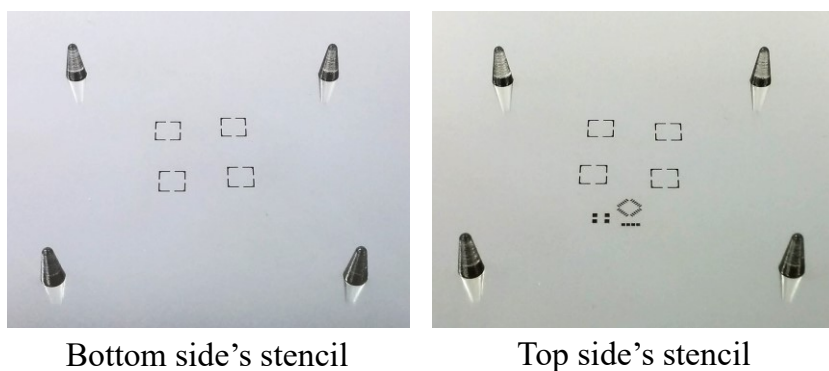


Figure 4.32 The stencils used in the production of the 2nd version sensor. They are for the top side and bottom side of the PCB. The locating pins of the support block can be seen as they go through the holes located on the stencil.

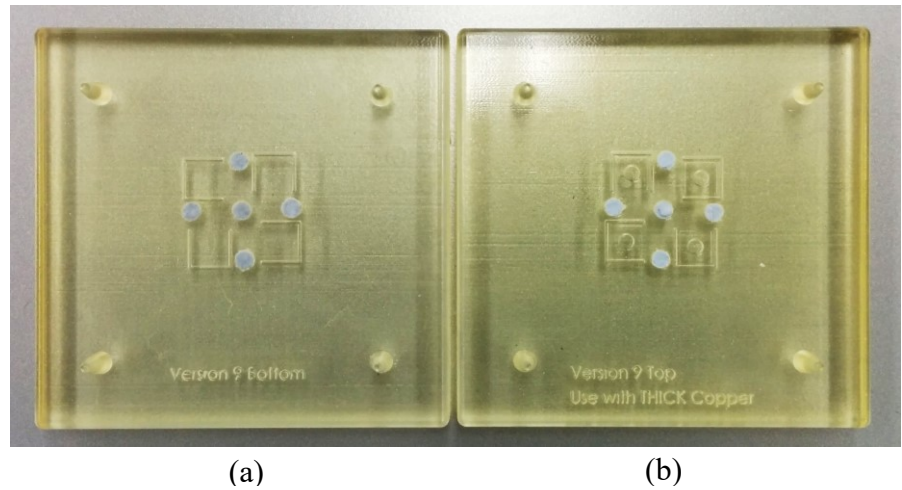


Figure 4.33 The PCB support blocks. Four locating pins are at four corners, five holes filled with Blue-Tack are at the center part and grooves for easy positioning of the PCB. (a) The support block for putting the PCB with the bottom side down. (b) The support block for putting the PCB with the top side down. Additional holes for the transducers' bumps can be seen.

The components used during the process of using the stencil to paste the solder on the PCB can be seen in Figure 4.34. For the procedure of mounting the copper beryllium plates on the PCB, the bottom side of the PCB would be mounted first because there are more components need to be mounted on the top side so it was easier to mount the top-side component last.

After the PCB was carefully placed on the support block, a light pressure was used to hold the PCB down by the provided Blue-Tack. The block was then placed under the stencil; the locating pins guided the block to the correct position; the stencil would be pushed slightly against the block to provide a firm contact between the stencil and the PCB. This would help in pasting a sharp and clear solder pattern on the PCB. The result of using the stencil to print solder paste on the PCB can be seen in Figure 4.35. Note that a slight shift in the location of the solder is allowable since the solder will be attracted and melt to the surrounding copper pad during the reflow process, not the overlay area (orange).



Figure 4.34 The components used in applying the solder paste on the 2nd version PCB. They are a stencil, a PCB support block, a container of solder paste, and a squeegee.

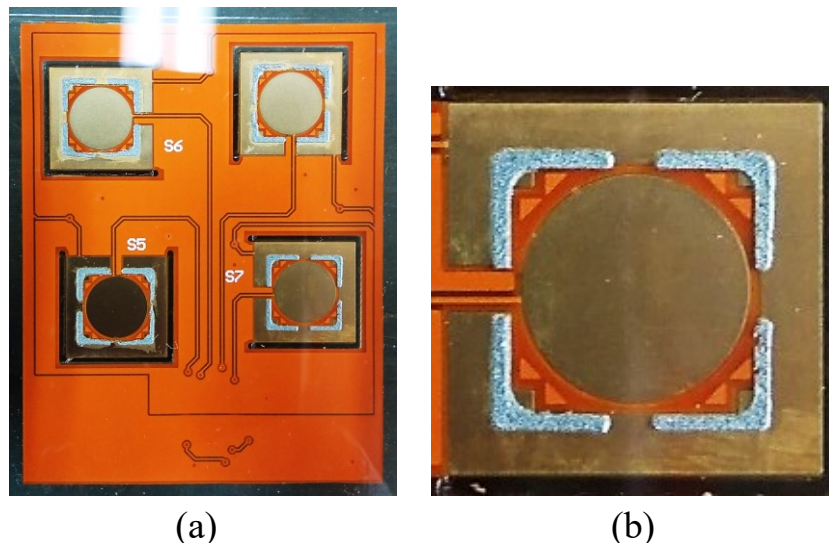


Figure 4.35 The result of using the stencil to regulate the amount of solder and control the desired location. (a) Overview of the pasted PCB. (b) A close-up view of a transducer area. Note that a slight shift in the location of the solder is allowable since the solder will be attracted to the surrounding copper pad during the reflow process.

4.3.2.2 Vacuum pick-up tool

After each side of the PCB was pasted with solder, the PCB was moved from the support block to place on a general-purpose FR-4 rigid PCB board as shown in Figure 4.36. This board was used to support the flexible PCB when it was inside the reflow oven; it also made the transportation of the PCB into the oven easier than just holding a flexible PCB which contains not-yet-soldered copper plates that could move with only a slight impact.

FR-4 is a composite material which can withstand the maximum reflow temperature of 250 °C while the support block will start to soften at around 50 °C. Additionally, Kapton tape was used to fix the flexible PCB steady to the FR-4 board. This tape is made of polyimide film and high-temperature silicone adhesive, and it can also withstand the temperature up to 260 °C.

Consequently, the copper beryllium plates were manually placed on each side of the PCB where the solder was pasted. In order to make the placement as steady as possible, a vacuum pick-up tool P-835 from Hozan was used together with a manual z-axis stage to hold the pick-up tool vertically above the PCB while holding the copper plate; the setup can be seen in Figure 4.36. The stage was carefully moved on a flat table to adjust the placement position. The z-axis was lower down until only a few millimeters left between the copper plate and the PCB. The vacuum pump of the tool was then turned off to let the plate drop onto the PCB. When four copper plate was successfully placed on the PCB, the flexible PCB was placed inside the reflow oven together with the FR-4 board.

The result of the reflow process is shown in Figure 4.37. It can be seen that the solder expanded outward into a small area of the surrounding pad.

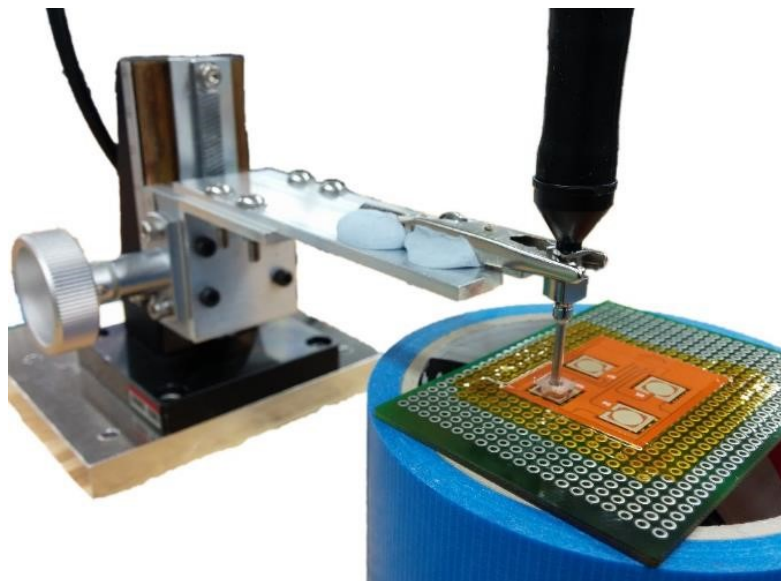


Figure 4.36 The vertical vacuum pick-up tool setup used to steadily place the copper beryllium plate on the pasted PCB. A general purpose FR-4 is used to provide rigid support to the PCB.

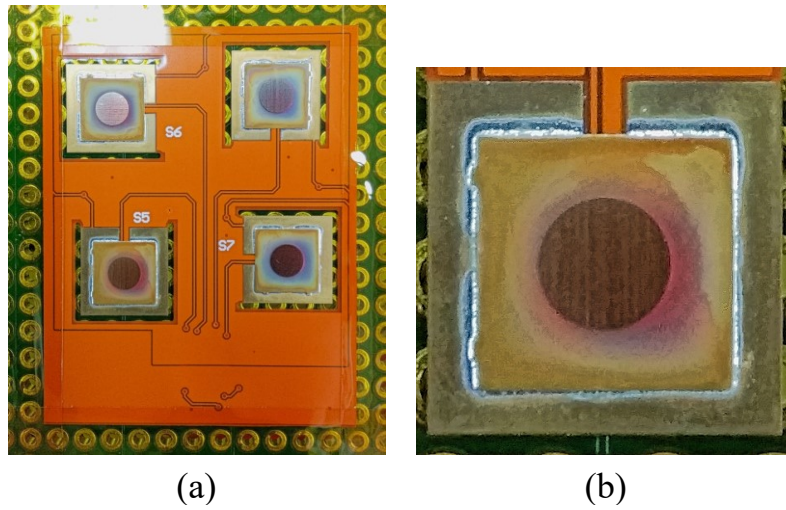


Figure 4.37 The resultant PCB after reflow soldered. (a) Overview of the PCB. (b) A close-up view of a transducer area. Note that only slight amount of solder expands outside the perimeter of the copper beryllium plate.

4.3.2.3 Degassing chamber

In order to create sufficient degassing power to properly remove all the air bubbles during the silicone molding process, a degassing chamber with a vacuum pump is built. The degassing equipment can be seen in Figure 4.38; it consists of cylindrical stainless pot which the top is wrapped with soft rubber to ensure a perfect seal, the top lid made from a 10 mm-thick polycarbonate plate, turning valves for controlling the pressure, a pressure dial for monitoring the current pressure, an air filter, and a vacuum pump G-10DA by ULVAC. The pressure of -0.09 MPa is generated and used for remove the residual bubbles after 1) the silicone is well mixed, and 2) after the silicone is poured into the mold.



Figure 4.38 The degassing equipment.

4.3.3 Conductive ink

According to the specification of the flexible PCB manufacturer, it can be seen in Figure 4.39 that there were two gaps which could allow the center electrode to be interfered by external stray capacitance if there is an object, especially one made of metal nearby. A gap of 50 μm is located where the solder paste would be in order to mount the CuBe₂ plate to the surrounding pad. It could be assumed that this gap was mostly sealed with the ground signal when the reflow process was completed. However, some spots around the perimeter of the copper plate could be left unsealed since there were 4 points where no solder would be pasted onto the PCB as can be seen in Figure 4.35(b). Another gap is located on the side of the PCB with the size of around 32.5 μm . This gap cannot be closed by the solder because it is not solderable.

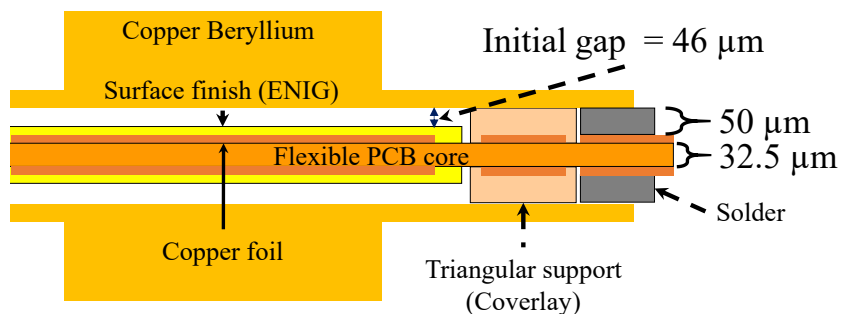


Figure 4.39 The section view of the transducer. The thickness of the solder, the PCB core are shown.

In order to close these gaps, a conductive ink called Electric Paint from Bare Conductive (see Figure 4.40) was chosen to do “cold solder” at the gaps. The ink was used to paint on the desired spot which will become conductive after it fully dried. The ink was applied carefully to the two areas mentioned before; the 50- μm gap was sealed first before the bending of the transducers was performed. The resultant paint after dried can be seen in Figure 4.41. While the 32.5- μm gap was painted after the bending because of the ease of access to the side of the bent PCB, and the result can be seen in Figure 4.42. Since the ink using here was quite viscous, painting the side of the PCB became relatively easy; a small portion of the ink would wrap around the side of the PCB toward both the top and the bottom of the PCB. Additionally, a small amount of silicone was applied around the perimeter of the CuBe₂ plate on top of the well-dried conductive ink in order to prevent the leakage of the liquid silicone into the transducers which might occur when a vast amount of silicone of the final molding was poured on the PCB.



Figure 4.40 The conductive ink used in this version of the sensor. It is Bare Conductive electric paint.



Figure 4.41 The sensor's PCB after it is painted with the conductive ink at the perimeter of the CuBe₂ plate.

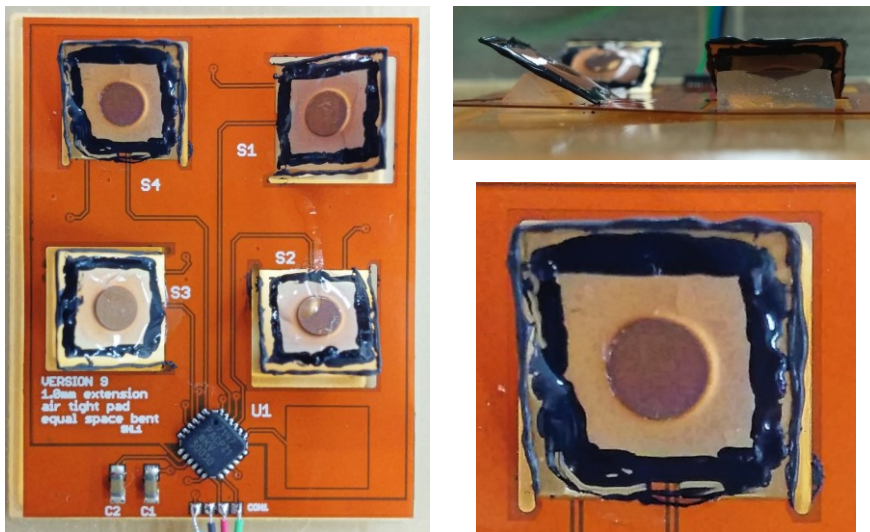


Figure 4.42 The sensor's PCB after it is painted on the side of the transducers. Note a small amount of silicone on the transducers' top, especially around the CuBe₂ plate.

4.3.4 Bending angle assessment

Compared to the bending procedure in the first version, an additional step was added in this version in order to make sure all the transducers were bent at the same angle; particularly, a protractor was used as shown in Figure 4.43 to ensure the uniform angles. As a result, it was found that the desired 45-degree angle could not be achieved due to the springback of the bent PCB portion which pushed back onto the silicone triangular support. Therefore, the bending angle was set to 30 degrees instead for all the transducers.

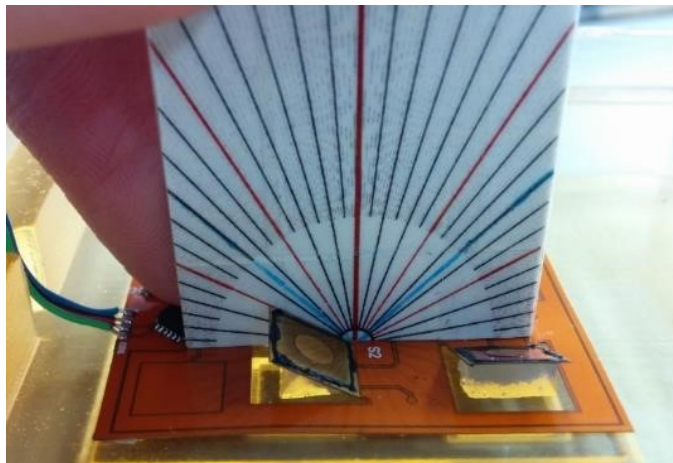


Figure 4.43 The method of using a protractor to confirm the bending angle of all the transducers.

4.3.5 Sensor molding improvement

As can be seen in Figure 4.11(e) and (f) that the molded sensor has a curved edge on the surface due to the surface tension of the liquid silicone. Moreover, if the previous mold was left to cure on the slant surface, the sensor surface would be slant as well. Therefore, the mold was designed in this second version sensor as can be seen in Figure 4.44. This mold composed of two pieces: the base and the cover. The base has an open on one side for the silicone to be poured in. The cover was designed to put on top of the base to make a flat top surface without any curve around the perimeter of the silicone due to the surface tension. Moreover, the thickness of the skin can be easily and reliably controlled now.

To use this mold, firstly the sensor's PCB was fixed with double-sided tape at the center of the mold where the pattern of the PCB was embossed on the outside of the mold for easy positioning. The silicone triangular supports were then inserted under the transducers; the bending angle of 30 degrees was controlled by the protractor. The side of the transducers was then carefully painted by the conductive ink. The mold cover was assembled to the mold base, and they were fixed together with hot glue. The glue also

used to prevent any leakage of the silicone when it was poured into the mold. After left the ink to dry completely for approximately 30 minutes, the mold was put on its side opposite to the opening. The liquid silicone was then slowly poured into the mold through the opening. The mold was left sitting on its side for 4 hours until the silicone was completely cured. The process of molding and the completed skin sensor can be seen in Figure 4.45.



Figure 4.44 The improved mold consists of 2 pieces: the base and the cover. The silicone would be poured from the side in this version for a more effective degassing and to acquire flat surface.

4.3.6 Experiments setup

Four tests were done with the second version sensor for evaluating its tri-axial force detection. These tests were to calibrate normal force sensing, to calibrate shear force sensing, being pushed simultaneously by x- and y-shear forces, and being pushed at varied ratios of normal and shear force. The last two tests were to validate the calibrated force vector detection. The tri-axial force detection setup as shown in Figure 4.46 consists of a vertical force generating unit which is mounted on the vertical axis of a manually-operated 3-axis stage. The force generating unit is composed of a VM5050-190 linear voice coil motor from Geplus (called VCM hereafter), a 6-axis force-torque sensor (Nano1.5/1.5 from BL Autotech), a linear bushing, an aluminum shaft that connect VCM's shaft to the force-torque sensor, and a 30x30 mm² acrylic push plate which is mounted to the end of the force-torque sensor for pushing on the skin sensor. The size of the plate is chosen to cover all the sensing units, allowing all units to be pushed at the same time.

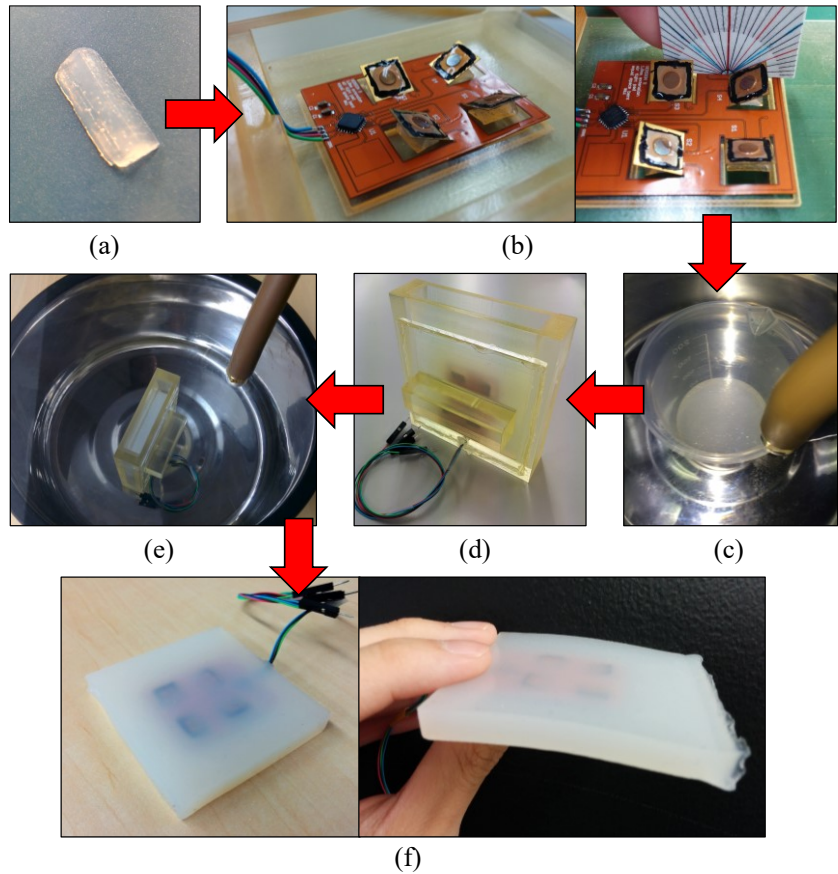


Figure 4.45 The molding process of the second skin sensor. (a) One of the molded triangular support. (b) The supports are inserted under the transducer; the tilting angles are confirmed with a protractor. (c) The mixed silicone is being degassed before pouring into the mold. (d) The mold with the liquid silicone and the sensor inside. (e) The degassing right after pouring the liquid silicone into the mold. (f) The sensor after the molding.

The force exerted by the VCM was controlled by a motor driver (LMD18245 from Texas Instrument); by regulating the current feed to the motor; the force produced by a VCM is proportional to the applied current. The current command and the direction of motion were given by the Arduino Due. The actual forces and torques were sensed by the force-torque sensor and read by an Arduino Uno. Two microcontrollers were used because of the different voltage levels of the skin sensor (3.3 V) and the 6-axis force-torque sensor (5 V) (the VCM is powered with 24 VDC). The actual forces and the readouts of the sensor were recorded into an SD card on each Arduino with synchronized sampling rate of 40 Hz. The synchronization of the two sensor readings was verified with an oscilloscope.

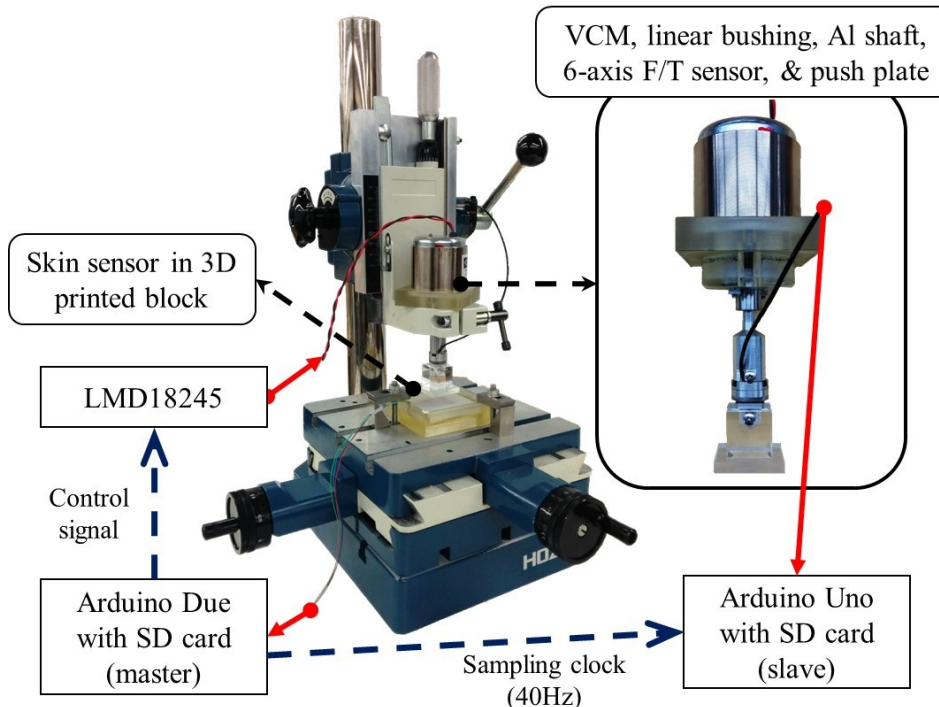


Figure 4.46 The experimental setup of the triaxial force test.

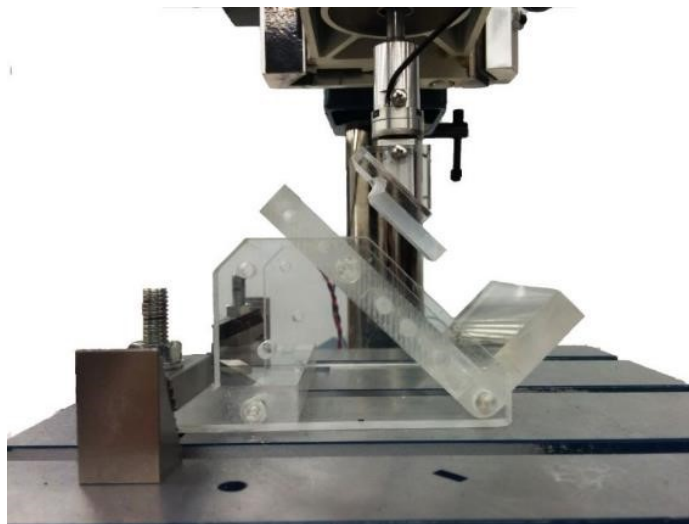


Figure 4.47 The adjustable angle stage fixed at 45 degrees with respect to the x-y stage surface and the corresponding 45-degree push plate.

In the normal force calibration, the molded skin sensor was placed in a 3D printed hard-plastic block and the block was then mounted to the top of the x-y stage with step clamps. In the shear force calibration, the push plate was changed to a plate which had a 45-degree alignment with the axis of the push unit, and an acrylic adjustable angle stage was used to position the skin sensor at 45 degrees (refer to Figure 4.47). Therefore, the vertical force generated by the VCM was decomposed into normal and tangential forces acting on the sensor's surface. Additionally, by rotating the sensor on the surface of the tilted

stage, the multi-directional shear force can be generated. The axes of the sensor and its origin are defined as shown in Figure 4.48. In the x-y shear push test, a new 3D printed plastic block as shown in Figure 4.49 was used to hold the skin sensor. With this block, the shear force acting in both x- and y-directions can be generated simultaneously. In the last test, the adjustable angle stage was altered to 30 and 15-degrees in order to change the proportion of the normal force and shear force acting on the proposed sensor (the push plates having the same angle were used correspondingly (refer to Figure 4.50)).

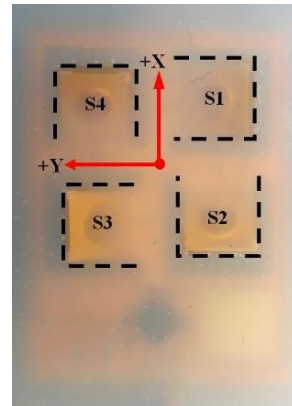


Figure 4.48 The location of the 4 force sensing units and the axes and origin of the skin sensor are shown.

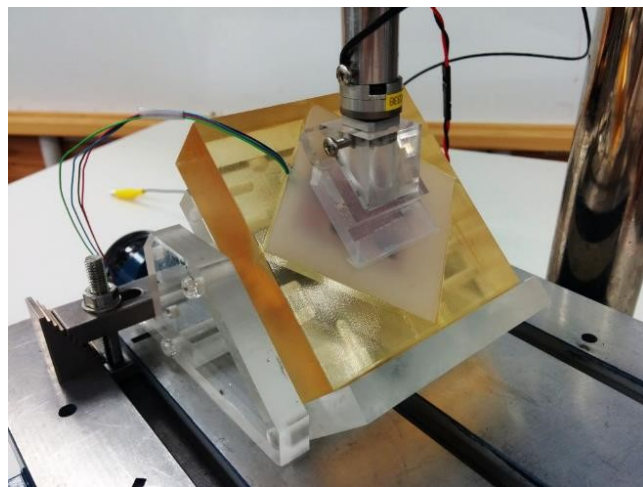


Figure 4.49 A 3D printed plastic block that allows the sensor to be aligned at 45 degrees with respect to the outer edge of the block. This allows the shear force to act in both x and y directions at the same time.

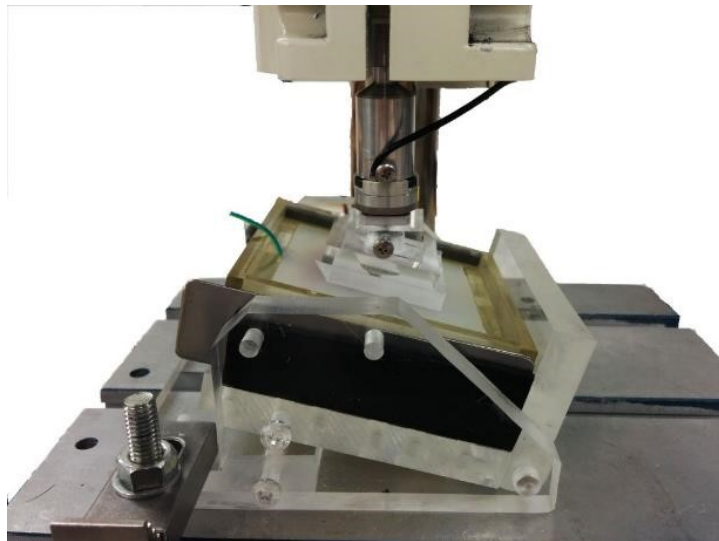


Figure 4.50 The adjustable angle stage is set at 15 degrees with respect to the x-y stage surface and the corresponding 15-degree push plate.

4.3.7 Result and discussion

4.3.7.1 Normal force calibration

The experiment was conducted by continuously pushing the sensor vertically with 6 equally-spaced steps of forces which the VCM can generate, which ranges from around 340 g to 1440 g. Each step lasted for 10 seconds. Then the force was increased at the end of each step.

The test was repeated 4 times, all collected data were filtered with a Savitzky-Golay filter. The sensor's readout and the forces sensed by the force-torque sensor are shown in Figure 4.51(a) and (b) respectively; the different response of each sensing unit to the same force can be clearly seen. The calibration of each sensing unit with respect to the vertical force F_z is done by firstly dividing the F_z by 4 considering that the force is equally distributed to all 4 sensing units. A quadratic polynomial was then used to convert the i th sensor measurements $S_i(t)$ in digits at time t to force $F_i(t)$ in gram.

$$F_i(t) = a_i S_i(t)^2 + b_i S_i(t) \quad (5)$$

The coefficients a and b of each sensing unit were computed by using all of the collected data excluding the 1st second of each push in order to remove the transient response. As a result, 4 quadratic functions were constructed with averaged root-mean-square error (RMSE) of 5.8035g and averaged R-squared value of 0.9776.

The result of the calibration is shown in Figure 4.51(c). It can be seen that the readouts are close to each other. Moreover, the summation of all calibrated readouts is mostly identical to F_z as can be seen in Figure 4.51(d) with the RMSE value of 21.69 g.

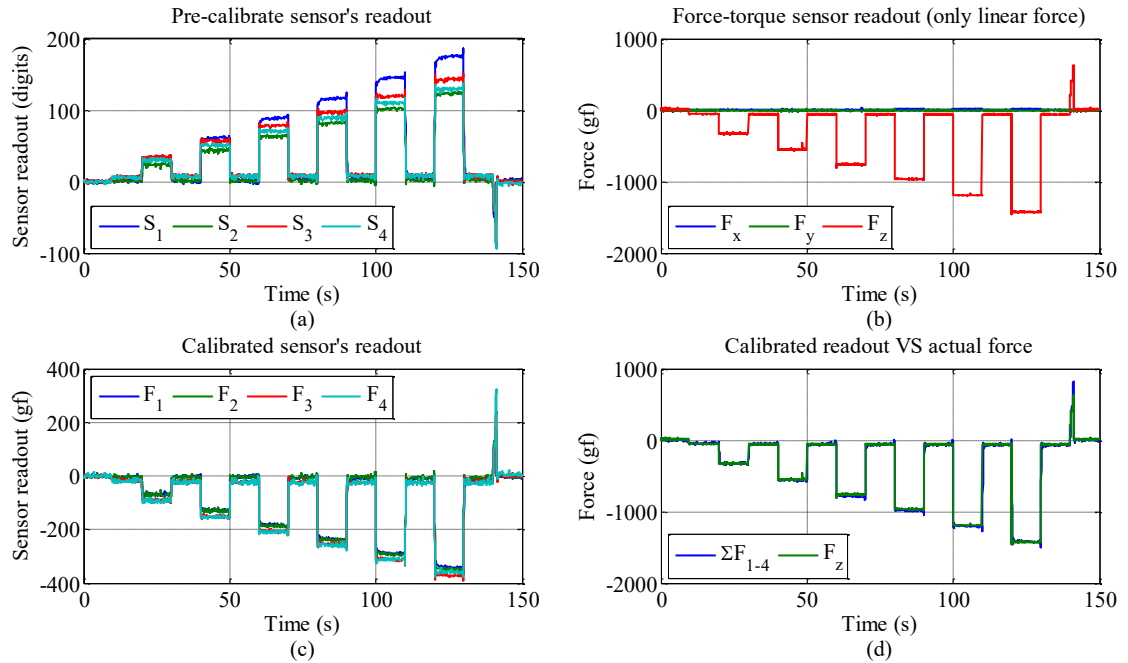


Figure 4.51 The result of the sensor calibration experiment. (a) pre-calibrate sensor's readout (b) force-torque sensor readout (only linear force) (c) calibrated sensor's readout (d) the comparison between converted sensor's readout and actual force readout.

4.3.7.2 Shear force calibration

This test was performed in the same fashion as the previous test; the VCM exerts a vertical force on the sensor's surface. The same 6 steps of incremental forces were applied on the sensor for a 10-second interval per step. However, this time, the test with a shear force acting in each direction (+x, -x, +y, -y) was repeated 4 times. All collected data was then filtered with a Savitzky-Golay filter and then converted into force values by using their corresponding quadratic equations obtained from the previous experiment.

The resultant force sensed by each sensing unit when the shear force was acting in each direction is shown in Figure 4.52. It can be seen that the transducer that points in the same direction as the shear force sensed higher forces while the transducer that points in the opposite direction sensed lower forces when compared to the average of all sensing units. The forces sensed by the other 2 units which point in the direction perpendicular to the shear force were close to the average line. Moreover, it can also be seen that the increment and the decrement of force sensed by the 2 units which are parallel to the shear force

direction had relatively the same magnitude of change. This pattern of response can be used to decompose a force vector into normal and shear force components.

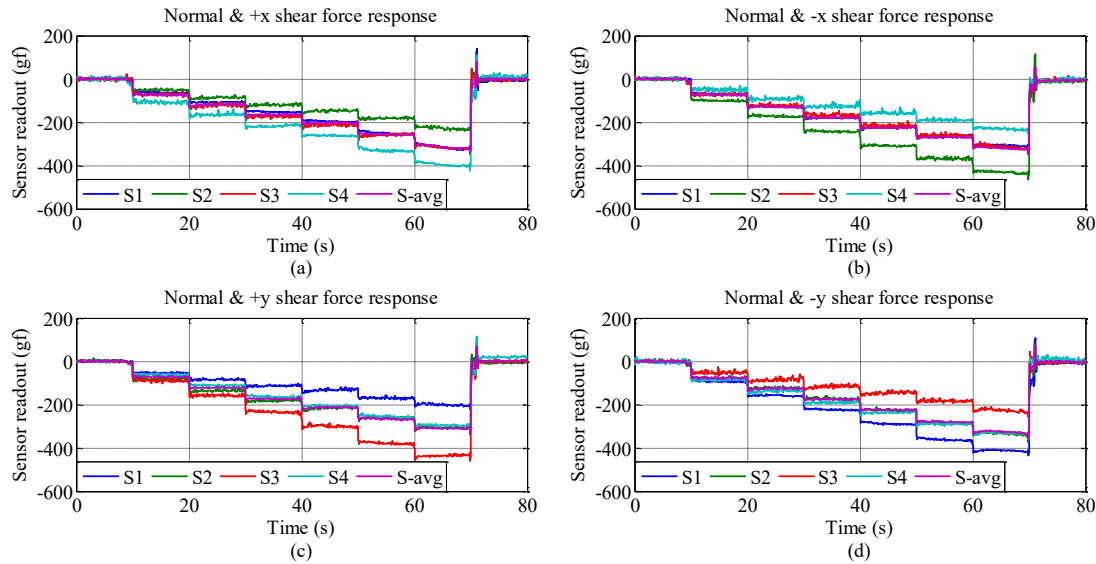


Figure 4.52 The resultant force sensed by all 4 units when being pushed with a normal and a shear force acting in different directions. (a) with $+x$ shear force (b) with $-x$ shear force (c) with $+y$ shear force (d) with $-y$ shear force.

Subsequently, the result of this experiment was used to determine the coefficients of the following equations in order to allow the sensor to measure an arbitrary force vector.

$$F_{x,\text{skin}}(t) = a_x(F_4(t) - F_2(t)) \quad (6)$$

$$F_{y,\text{skin}}(t) = a_y(F_3(t) - F_1(t)) \quad (7)$$

A linear function was used for acquiring the equation for each axis of force. The linear curve fitting was done by firstly excluding out the 1st second and the 10th second of each step of a push to eliminate the transient-state data. The data of $+x$ and $-x$ shear forces were used to determine a_x and $+y$ and $-y$ shear force's data were used to calculate a_y . As a result, the coefficients a_x and a_y were calculated with RMSE values of 42.33 g, 42.60 g, and 27.07 g, and R-squared values of 0.9820, 0.9836, and 0.9958 respectively.

Furthermore, to demonstrate the ability of force vector detection, a plot between calculated force vector and one of the actual force data (used during the calculation of a_x , and a_y previously) with the $+x$ shear component is shown in Figure 4.53 with RMSE values of 33.00 g, 39.54 g, and 18.24 g for $F_{x,\text{skin}}$, $F_{y,\text{skin}}$, and $F_{z,\text{skin}}$ respectively. It can be seen that $F_{y,\text{skin}}$ is the least accurate while $F_{z,\text{skin}}$ is the most accurate. On the other hand,

when comparing the force calculation when applying +y shear force, $F_{x,skin}$ becomes the least accurate. Moreover, it can be seen that the sensor is more sensitive to normal force than shear force. This could be due to the PCB bending angle of 30 degrees; hence, the sensor is more affected by the normal force component.

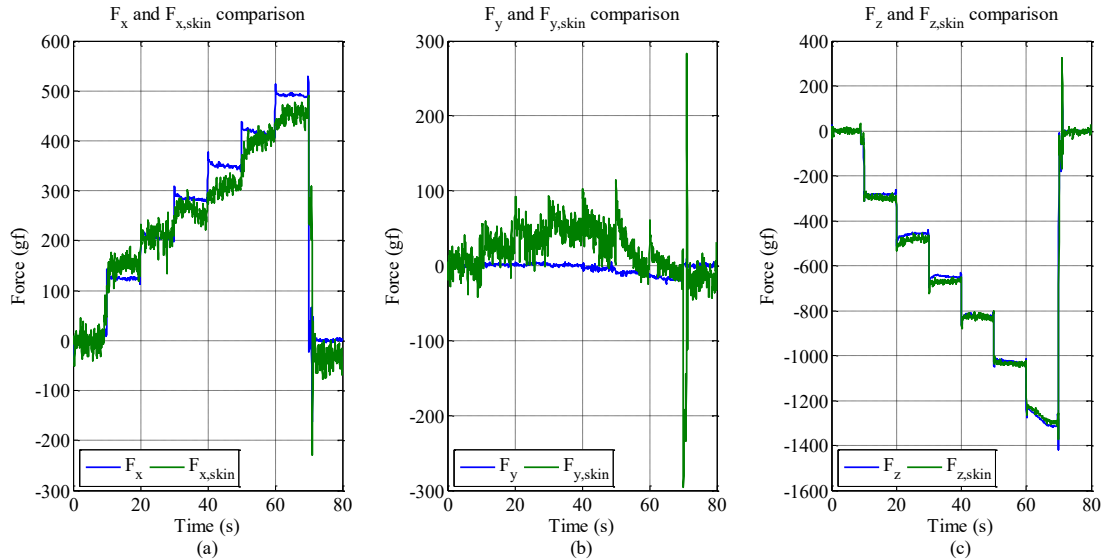


Figure 4.53 The comparison between the calculated force vector and the actual force vector when normal force and +x shear force is applied. The adjustable angle stage is set to 45-degrees.

4.3.7.3 X-Y shear force push

The block shown in Figure 4.49 was used. The same pattern of pushing of the force generating unit as in the previous experiment was used.

In this test, normal force and shear force acting in 4 directions; +x+y, +x-y, -x+y, and -x-y directions were exerted on the sensor in this experiment. The result of pushing the sensor with shear force in the direction of +x+y can be seen in Figure 4.54 with RMSE values of 24.41 g, 31.98 g, and 20.74 g while the averaged RMSEs of all 4-direction shear tests are 36.01 g, 38.69 g, and 19.93 g for $F_{x,skin}$, $F_{y,skin}$, and $F_{z,skin}$ respectively.

4.3.7.4 30- and 15-degree pushes

The stage was adjusted to 30 and 15 degrees and the block as in Section 4.3.7.1 and 4.3.7.2 was used. At each angle setting, the sensor was pushed in 4 directions of shear force namely +x, -x, +y, and -y direction with their corresponding push plates having the same angle (refer to Figure 4.50). Again, the same pattern of pushing of the force generating unit as in the previous experiment was used.

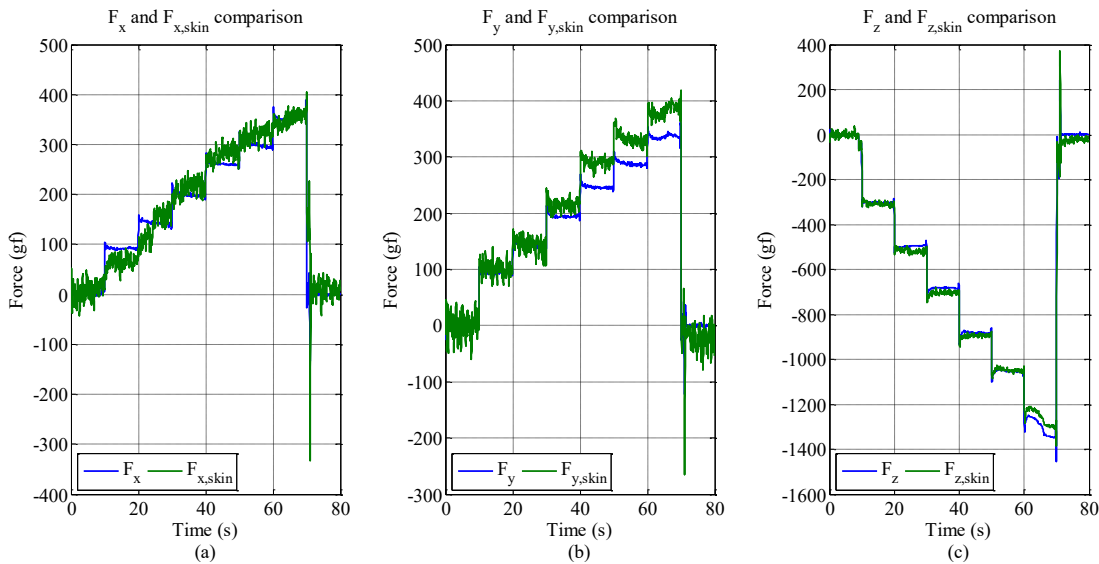


Figure 4.54 The comparison between calculated force vector and the actual force vector when the normal force and +x+y shear force is applied. The adjustable angle stage is set to 45-degree.

Table 4.4. The comparison of the force vector calculation's accuracy at all experiments in the Triaxial force test section.

| Experiment | RMSE | | | R-squared | | |
|-----------------------------------|--------------|--------------|--------------|--------------|--------------|--------------|
| | $F_{x,skin}$ | $F_{y,skin}$ | $F_{z,skin}$ | $F_{x,skin}$ | $F_{y,skin}$ | $F_{z,skin}$ |
| Calibration at 45 degree | 41.7728 | 34.3551 | 24.9617 | 0.93878 | 0.93882 | 0.99618 |
| With both x & y shear | 36.0068 | 38.6854 | 19.9335 | 0.88953 | 0.86793 | 0.99721 |
| Varied normal & shear ratio | 30 degree | 49.6397 | 25.4368 | 38.7147 | 0.73647 | 0.90931 |
| | 15 degree | 38.2085 | 29.3996 | 46.9959 | 0.43489 | 0.64024 |
| | | | | | | 0.98067 |

The comparison of the force vector calculation's accuracy in various experiments is shown in Table 4.4 as the values of averaged RMSE and R-squared for each axis at each test. When the pushing angle is decreasing, the ratio of shear force to normal force decreases too. According to the result when the sensor was pushed at 15-degree in +y direction, the maximum $F_{y,skin}$ was only 120 g while the maximum $F_{z,skin}$ was 1400 g. Therefore, when less force is sensed at a certain axis, the slightly varied RMSE values could further influence the measurement, resulting in lower R-squared values. Figure 4.55

shows the result of pushing the sensor at 15-degree with shear force in the direction of +y.

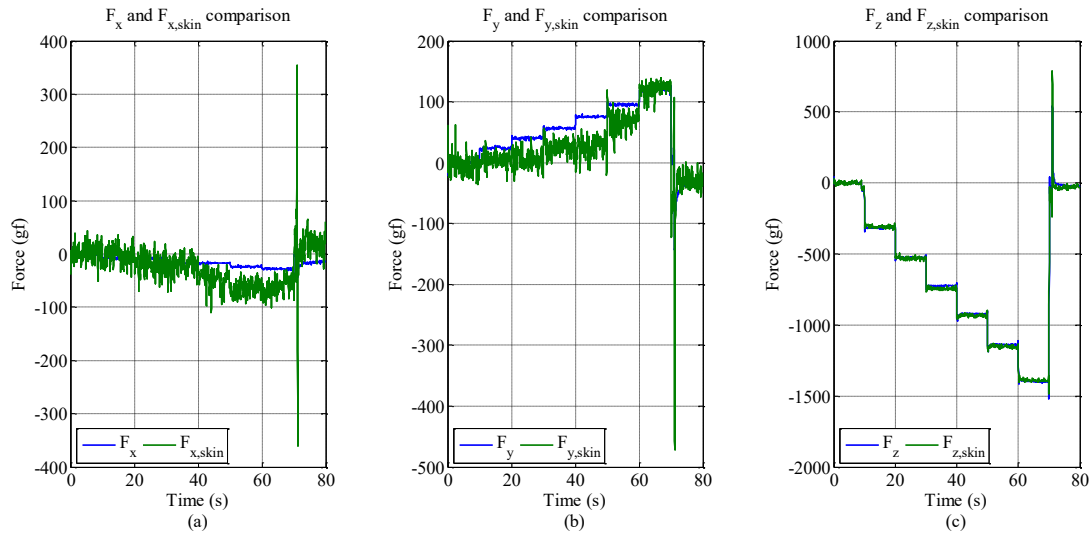


Figure 4.55 The comparison between calculated force vector and the actual force vector when normal force and +y shear force is applied. The adjustable angle stage is set to 15-degrees.

4.4 Conclusion

The skin sensor introduced a novel concept of tri-axial force measurement. It is made of compliant material and has a flat skin surface. Two versions of sensors were developed in this chapter.

The first version has proven that the proposed concept can distinguish both normal and shear force. Even submerge under 7 mm thick of soft silicone (Ecoflex Supersoft 30), the capacitive sensor is still able to sense the minimum force of 8.7 g. The sensor showed a second-order polynomial relationship against the applied load. The maximum measurable load at the moment was limited to 1400 g due to the maximum producible force of the actuator and the maximum known weight used in the test setup.

The design, the manufacturing process, and the experiment setup of the first version were used to improve those perspectives in the second version as listed below:

- The design was changed to allow a square-shaped alignment of the transducers after bending (at 45 degrees). (Repositioning the four transducers so that their centers form a square with respect to the measurement axis of the sensor after the 45-degree bending).

- The addition of a copper pattern between the center capacitive electrode and the surrounding pad in order to ensure the present of the support structure of the CuBe₂ plate to control the initial gap of the capacitive sensor. By putting the triangular copper pattern and the overlay on the area, the desired support can be produced properly by the PCB manufacturer.
- Further increment in the area of the surrounding pad to ensure sufficient space for the excess solder using in soldering the copper beryllium plate to the PCB.
- The amount of solder used, especially to solder the copper beryllium plate to the PCB, was controlled by the stencil. Moreover, the position of the solder can be easily and reliably controlled as well. The stencil makes the production of the sensor more reliable, less difficult, and consume less time.
- Further stray capacitive noise attenuation procedure by surrounding the bent-up transducer with grounded conductive ink to prevent the noise from entering the side of the PCB and disturbing the measurement when a metal part is near the sensor.
- The desired angle in the concept was 45 degrees since it could give a good balance between the measurement of normal and shear force. However, eventually, the achievable bending angle after confirmed with the protractor was only 30 degrees. This was due to the spring back of the flexible PCB and also, the triangular support made from the Ecoflex 30 had an angle of 45 degree. In the future, in order to achieve 45-degree bending by using the same method, the angle of the triangular support should be more than 45 degrees, a finite element simulation software can be used to make the redesign more reliable.
- The improvement in sensor molding in order to prevent the curved edge due to the surface tension of the liquid silicone on the open-top mold. The mold in the second iteration was designed to have a flat top surface. This was done by putting the mold up on its side where the pouring hole was. Moreover, the thickness of the skin can be reliably controlled now.
- The improvement in the experimental setup to have a force control pusher. The voice coil motor which its actuated force is proportion to the applied current was used to provide a regulated force onto the sensor. The force exerted on the sensor was monitor with the 6-axis force-torque sensor. The adjustable angle tilt stage

was used in order to introduce simultaneously normal and shear force on the sensor surface; this reduced the required actuator to only one. The angle of the stage can be adjusted to 45, 30, and 15 degrees. The 45-degree rotated square block allow the exertion of the shear force acting in both x and y-direction on the sensor to be possible.

The second prototype of the sensor showed that the tri-axial force can be measured successfully after the calibration even some RMSEs of around 50 g can be observed. The sensor calibrated by using the data of 45-degree test could be used to measure the force acting at 30 and 15 degrees.

5 CONCLUSION AND FUTURE WORK

5.1 Conclusion

The development of a sensitive yet soft and flexible robotic skin sensor with tri-axial force sensing capability was described. The development started from the construction of a simplified prototype built on a rigid PCB with only 1-axis force sensing capability. This first prototype, however, proposed an improved design of the transducer made of copper beryllium. The thick bump compared to the thin base of the transducer created a more uniform and more parallel deformation when it is subjected to external force. This enhanced both the sensitivity and the range of measurement of the sensor by allowing the copper beryllium plate to be put closer to the grounded electrode and increase the effective area which leads to more change in the total capacitance. This prototype also has a temperature compensation capability using a capacitive sensor which is insensitive to external force but sensitive to the thermal change. It also has a small-sized CDC chip installed on the PCB which allows the sensor to provide digital output directly in the form of I2C bus protocol. This I2C allows several PCB to share the same data wire hence reducing the amount of wiring required. Furthermore, after testing the sensor's performance, it can be seen that the sensor has a high signal-to-noise ratio of approximately 71 dB measured at 2.5 N load. It can sense 1 g to 1200 g-force while having only small hysteresis and has a close-to-linear relationship between the sensor's readout and actual load. The tested specification of the sensor is shown in Table 5.1.

Table 5.1. The specification of the capacitive-type force transducer developed in Chapter 2.

| Parameter | Value | Unit |
|---------------------------------|--------------------------------|------|
| Signal-to-noise ratio | 71 (tested at 0.254 gram load) | dB |
| Digital output (I2C) | 16 | bit |
| Hysteresis | 2.91 | % |
| Measurable force | 1 – 1200 | gram |
| Maximum thermal drift reduction | 60 | % |

Additionally, in order to demonstrate the wide spectrum of applications for which tactile sensors can be used, a two-way haptic interface which can provide a user the feeling of variable stiffness while measure the contact force and location from the user by using the first prototype sensors developed in Chapter 2 was proposed. The results of the experiments showed that the sensors work correctly regardless of the magnetic field. Moreover, it was discovered that the MR pouch can actually provide an additional feedback to the user; the vibration of the MR pouch can be generated by reversing the direction of the input current of the electromagnet. The frequency of the vibration is proportion to the switching frequency of the input current.

Lastly, a 3-axis soft skin sensor was developed in Chapter 4. The sensor proposed a novel arrangement of the capacitive transducers developed in Chapter 2. Two versions of the sensors were developed; the findings from the first version were used to improve the design, the production, and the performance of the second version. The second version showed improvements such as less stray capacitive noise, and uniform thickness and flat silicone skin. More importantly, the skin sensor showed that the measurement of the force vector can be successfully done after the calibration even though some RMSEs of around 50 g can be observed. The force measurement provided satisfactory results when compared to the actual force sensed by a commercially available 6-axis force/torque sensor. The sensor has only 3% hysteresis even though the transducers were suspended inside 7 mm thick silicone. The temperature compensation can suppress the susceptibility to thermal change by approximately 80%. The specification of the developed skin sensor is shown in Table 5.2. It should be noted that the measurable force in x and y direction are limited by the characteristic of the test setup used (refer to the test setup in Figure

4.46). The test setup cannot tilt more than 45 degrees, hence, the force of the pusher cannot exceed 500 g in x and y direction. Moreover, it is also due to the fact that the tilting angle of the transducer is 30 degrees which make the transducer more sensitive to the z-axis force than the x- and y-axis force.

Table 5.2. The specification of the second version of the 3-axis soft skin sensor developed in Chapter 4.

| Parameter | Value | Unit |
|---------------------------------|--------------------------------|----------|
| Signal-to-noise ratio | 51 (tested at 0.254 gram load) | dB |
| Digital output (I2C) | 16 | bit |
| Hysteresis | 3.36 | % |
| Measurable force | x | 30 - 500 |
| | y | 40 - 500 |
| | z | 9 - 1400 |
| Maximum thermal drift reduction | 80 | % |

5.2 Future Work

The capacitive-type 3-axis soft skin sensor has been presented with the novel arrangement of the transducers. The sensor could be installed in several parts of robots (e.g. hand, arm, chase, or back of the robots) to enhance the capability of the robot in interaction with the environment, object manipulation, and response to external force intelligently and effectively. With the sensor installed at the hands, the robots could utilize the tri-axial force sensing capability to estimate the weight of grasped object, or grasp an object with minimum force required (without dropping the object or allow the object to slide away from the hand), or improved its skill in in-hand object manipulation. Additionally, the compliance of the skin could help in holding an object firmly and attenuate error in manipulation because it can conform to the contour of the object to some extent. With the sensor installed at the arms, the chase, or the back of the robots, the robot can utilize the 3-axis force sensing ability to interaction with human or surrounding objects effectively. By knowing the magnitude and the direction of force, the robot can move its limb or its body in the opposite direction of the force in order to minimize the impact or to move away from it.

However, several aspects of the sensor can be improved. Further experimental evaluation is necessary to gain more information on the characteristics of the sensor. For example, several instances of the same sensor will be produced and tested, to obtain more comparative results. Overload experiments will be done as well.

Moreover, even though the tri-axial force measurement can be successfully done, there are many points for improvement for future work. Some improvement points are as follows.

- **The utilization of the whole top surface for tactile sensing:** as can be seen that in the current sensor, some area on the top of the PCB was used for the CDC chip and its necessary electronics components. In future work, these components can be placed on the bottom side of a 4-layer PCB while its traces are contained inside the middle two layers of the PCB. As a result, the whole surface of the robot can be covered with transducers and to make the sensor space efficient.
- **The compatibility of being distributed sensory network:** in the current PCB, there is only 1 I2C port which might lead to some challenges when trying to implement several of the sensors on a robot as a patch of skin sensor. Instead, having ports on all four sides will enable an efficient networking structure with minimal wiring, as in [81]. The adjacent sensors can directly connect to its closest port of the neighbor sensor and thus form the network.
- **The optimization of the transducer's size:** currently, the thesis presented just one size of the copper beryllium plate and its simulation result. Nevertheless, in order to obtain the desired force measurement range and sensitivity for a certain application, the optimal dimension of the plate including the size of the bump are necessary to be determined. The sensor with several sizes of the plate needed to be produced, tested and evaluated.
- **The optimization of the bending angle of the transducer:** only the bending angle of 30 degrees was done in this thesis in order to prove the feasibility of the concept. However, the optimal angle is needed to be determined and this optimal angle might be varied depending on the application. For example, if the sensitive shear force detection is more preferred, the more bending angle such as 60 degrees might be more suitable.
- **The finding of the most appropriate compliant material:** The Ecoflex Supersoft 30 silicone rubber from Smooth-On Company was selected in this thesis due to its durability, ease of use, and its softest (the Ecoflex Supersoft 10 is softer

but is covered with oily film). A less compliant silicone or another material might be preferable depending on applications.

- **A more automatized production procedure:** the production processes used in making the sensor shown in this thesis relied mostly on manual works but for practical reason and a more consistent result in sensors' performance, a more automatized manufacturing process is mandatory in the future. Additionally, the thought of feasibility in production need to be further signified during the sensor design phase.

As for the haptic interface, future work will improve the design; in particular, the size of the magnet could be reduced. Further experimental evaluation and improvement can be done. In particularly, the spatial test of the sensing unit on both sides can be done to have a more completed result. The vibration property of MR fluid by fast switching the magnetization current direction will be further investigated as well. Additionally, the sensor distribution for the optimal force sensor can be done in order to cover more space under the MR pouch. Furthermore, we plan to integrate two such devices into a robotic parallel gripper, in order to achieve a pick-and-place mechanism for fragile objects. Local magnetized MR fluid with different amperages could increase the flexibility and variety of applications as well.

REFERENCES

- [1] R. S. Dahiya, G. Metta, M. Valle, and G. Sandini, “Tactile Sensing - From Humans to Humanoids,” *IEEE Trans. Robot.*, vol. 26, no. 1, pp. 1–20, 2010.
- [2] M. R. Cutkosky, R. D. Howe, and W. R. Provancher, “Force and tactile sensors,” in *Springer Handbook of Robotics*, Springer, 2008, pp. 455–476.
- [3] G. Westling and R. S. Johansson, “Factors influencing the force control during precision grip.,” *Exp. brain Res.*, vol. 53, pp. 277–84, 1984.
- [4] R. S. Johansson and J. R. Flanagan, “Coding and use of tactile signals from the fingertips in object manipulation tasks.,” *Nat. Rev. Neurosci.*, vol. 10, no. 5, pp. 345–59, 2009.
- [5] S. Chitta and M. Piccoli, “Tactile Object Class and Internal State Recognition for Mobile Manipulation,” *Comp. Gen. Pharmacol.*, pp. 2342–2348, 2010.
- [6] R. A. Russell and S. Parkinson, “Sensing surface shape by touch,” in *Robotics and Automation, 1993. Proceedings., 1993 IEEE International Conference on*, 1993, pp. 423–428.
- [7] R. D. D. Howe and M. R. R. Cutkosky, “Sensing skin acceleration for slip and texture perception,” in *Robotics and Automation, 1989. Proceedings., 1989 IEEE International Conference on*, 1989, pp. 145–150.
- [8] J. Engel, J. Chen, X. W. X. Wang, Z. F. Z. Fan, C. L. C. Liu, and D. Jones, “Technology development of integrated multi-modal and flexible tactile skin for robotics applications,” in *Proceedings 2003 IEEERSJ International Conference on*

References

- Intelligent Robots and Systems IROS 2003 Cat No03CH37453*, 2003, vol. 3, pp. 2359–2364.
- [9] R. S. Dahiya, P. Mittendorfer, M. Valle, G. Cheng, and V. J. Lumelsky, “Directions toward effective utilization of tactile skin: A review,” *IEEE Sens. J.*, vol. 13, no. 11, pp. 4121–4138, 2013.
 - [10] K. Kojima, T. Sato, A. Schmitz, H. Arie, H. Iwata, and S. Sugano, “Sensor Prediction and Grasp Stability Evaluation for In-Hand Manipulation,” in *Intelligent Robots and Systems (IROS), 2013 IEEE/RSJ International Conference on*, 2013, pp. 2479 – 2484.
 - [11] R. D. Howe, N. Popp, P. Akella, I. Kao, and M. R. Cutkosky, “Grasping, manipulation, and control with tactile sensing,” *Proceedings., IEEE Int. Conf. Robot. Autom.*, pp. 1258–1263, 1990.
 - [12] A. Schmitz, Y. Bansho, K. Noda, H. Iwata, T. Ogata, and S. Sugano, “Tactile Object Recognition using Deep Learning and Dropout,” in *IEEE-RAS International Conference on Humanoid Robots (Humanoids 2014)*, 2014, pp. 1044 – 1050.
 - [13] A. Bierbaum, M. Rambow, T. Asfour, and R. Dillmann, “A potential field approach to dexterous tactile exploration of unknown objects,” *2008 8th IEEE-RAS Int. Conf. Humanoid Robot. Humanoids 2008*, pp. 360–366, 2008.
 - [14] S. J. Lederman and R. L. Klatzky, “Hand movements: a window into haptic object recognition.,” *Cogn. Psychol.*, vol. 19, no. 3, pp. 342–368, 1987.
 - [15] H. Iwata and S. Sugano, “Design of human symbiotic robot TWENDY-ONE,” in *Robotics and Automation, 2009. ICRA ’09. IEEE International Conference on*, 2009, pp. 580–586.
 - [16] M. Botvinick and J. Cohen, “Rubber hands’ feel’touch that eyes see,” *Nature*, vol. 391, no. 6669, p. 756, 1998.
 - [17] J. Bongard, V. Zykov, and H. Lipson, “Resilient machines through continuous self-modeling.,” *Science*, vol. 314, no. 5802, pp. 1118–21, 2006.
 - [18] M. H. Lee, “Tactile sensing: new directions, new challenges,” *Int. J. Rob. Res.*, vol. 19, no. 7, pp. 636–643, 2000.
 - [19] J. S. Son, M. R. Cutkosky, and R. D. Howe, “Comparison of contact sensor

- localization abilities during manipulation,” in *Robotics and Autonomous Systems*, 1995, vol. 2, pp. 96 – 103.
- [20] P. Maiolino and M. Maggiali, “A flexible and robust large scale capacitive tactile system for robots,” *IEEE Sens. J.*, vol. 13, no. 10, pp. 3910–3917, 2013.
- [21] A. Schmitz, P. Maiolino, M. Maggiali, L. Natale, G. Cannata, and G. Metta, “Methods and technologies for the implementation of large-scale robot tactile sensors,” *IEEE Trans. Robot.*, vol. 27, no. 3, pp. 389–400, 2011.
- [22] G. Robles-De-La-Torre, “The Importance of the sense of touch in virtual and real environments,” *IEEE Multimed.*, vol. 13, no. 3, pp. 24–30, 2006.
- [23] R. D. Howe and M. R. Cutkosky, “Integrating tactile sensing with control for dexterous manipulation,” in *IEEE International Workshop on Intelligent Motion Control*, 1990, no. 1, pp. 369–374.
- [24] P. Mittendorfer and G. Cheng, “Integrating discrete force cells into multi-modal artificial skin,” in *2012 12th IEEE-RAS International Conference on Humanoid Robots (Humanoids 2012)*, 2012, pp. 847–852.
- [25] H. R. Nicholls and M. H. Lee, “A Survey of Robot Tactile Sensing Technology,” *Int. J. Rob. Res.*, vol. 8, pp. 3–30, 1989.
- [26] M. . Lee and H. . Nicholls, “Review Article Tactile sensing for mechatronics—a state of the art survey,” *Mechatronics*, vol. 9, no. 1, pp. 1–31, 1999.
- [27] S. C. Jacobsen et al., “Design of tactile sensing systems for dexterous manipulation,” *{IEEE} Control Syst. Mag.*, vol. 8, no. 1, pp. 3 – 13, 1988.
- [28] P. Puangmali, K. Althoefer, L. D. Seneviratne, D. Murphy, and P. Dasgupta, “State-of-the-art in force and tactile sensing for minimally invasive surgery,” *IEEE Sens. J.*, vol. 8, no. 4, pp. 371–380, 2008.
- [29] R. D. Howe, “Tactile Sensing and Control of Robotic Manipulation.” *J. Adv. Robot.*, vol. 8, no. 3, pp. 245–261, 1994.
- [30] B. D. Argall and A. G. Billard, “A survey of Tactile Human-Robot Interactions,” *Rob. Auton. Syst.*, vol. 58, no. 10, pp. 1159–1176, 2010.
- [31] D. Silvera-Tawil, D. Rye, and M. Velonaki, “Artificial skin and tactile sensing for socially interactive robots: A review,” *Rob. Auton. Syst.*, vol. 63, pp. 230–243, 2015.

References

- [32] D. Göger, N. Gorges, and H. Wörn, “Tactile sensing for an anthropomorphic robotic hand: Hardware and signal processing,” in *IEEE International Conference on Robotics and Automation*, 2009, pp. 895–901.
- [33] B. Choi, S. Lee, H. R. Choi, and S. Kang, “Development of anthropomorphic robot hand with tactile sensor: SKKU hand II,” in *IEEE International Conference on Intelligent Robots and Systems*, 2006, pp. 3779–3784.
- [34] J. Jockusch, J. Walter, and H. Ritter, “A tactile sensor system for a three-fingered robot manipulator,” in *Proceedings of International Conference on Robotics and Automation*, 1997, vol. 4, pp. 3080–3086.
- [35] K. Hosoda, Y. Tada, and M. Asada, “Anthropomorphic robotic soft fingertip with randomly distributed receptors,” *Rob. Auton. Syst.*, vol. 54, no. 2, pp. 104–109, 2006.
- [36] T. Minato, Y. Yoshikawa, T. Noda, S. Ikemoto, H. Ishiguro, and M. Asada, “CB2: A child robot with biomimetic body for cognitive developmental robotics,” in *2007 7th IEEE-RAS International Conference on Humanoid Robots, HUMANOIDS 2007*, 2007, pp. 557–562.
- [37] S. Saga, T. Morooka, H. Kajimoto, and S. Tachi, “High-Resolution Tactile Sensor Using the Movement of a Reflected Image,” in *Proceedings of Eurohaptics*, 2006, pp. 81–86.
- [38] W. Yuan, R. Li, M. A. Srinivasan, and E. H. Adelson, “Measurement of shear and slip with a GelSight tactile sensor,” in *Robotics and Automation (ICRA), 2015 IEEE International Conference on*, 2015, pp. 304–311.
- [39] K. Yamada, K. Goto, Y. Nakajima, N. Koshida, and H. Shinoda, “A sensor skin using wire-free tactile sensing elements based on optical connection,” in *Proceedings of the 41st SICE Annual Conference. SICE 2002.*, 2002, vol. 1, pp. 131–134.
- [40] T. Yoshikai, M. Hayashi, Y. Ishizaka, H. Fukushima, A. Kadokawa, T. Sagisaka, K. Kobayashi, I. Kumagai, and M. Inaba, “Development of robots with soft sensor flesh for achieving close interaction behavior,” *Adv. Artif. Intell.*, vol. 2012, pp. 8–8, 2012.
- [41] M. Ohka, A. Tsunogai, T. Kayaba, S. C. Abdullah, and H. Yussof, “Advanced Design of Columnar-conical Feeler-type Optical Three-axis Tactile Sensor,”

- Procedia Comput. Sci.*, vol. 42, pp. 17–24, 2014.
- [42] L. Jamone, G. Metta, F. Nori, and G. Sandini, “James: A humanoid robot acting over an unstructured world,” in *Humanoid Robots, 2006 6th IEEE-RAS International Conference on*, 2006, pp. 143–150.
 - [43] L. Jamone, L. Natale, G. Metta, and G. Sandini, “Highly Sensitive Soft Tactile Sensors for an Anthropomorphic Robotic Hand,” *Sensors Journal, IEEE*, vol. 15, no. 8, pp. 4226–4233, 2015.
 - [44] L. Natale and E. Torres-jara, “A sensitive approach to grasping,” in *Proceedings of the sixth international workshop on epigenetic robotics*, 2006, pp. 87–94.
 - [45] S. Youssefian, N. Rahbar, and E. Torres-Jara, “Contact Behavior of Soft Spherical Tactile Sensors,” *Sensors Journal, IEEE*, vol. 14, no. 5, pp. 1435–1442, 2014.
 - [46] C. Ledermann, S. Wirges, D. Oertel, M. Mende, and H. Woern, “Tactile sensor on a magnetic basis using novel 3D Hall sensor-First prototypes and results,” in *Intelligent Engineering Systems (INES), 2013 IEEE 17th International Conference on*, 2013, pp. 55–60.
 - [47] T. Liu, Y. Inoue, and K. Shibata, “Design of low-cost tactile force sensor for 3D force scan,” in *Sensors, 2008 IEEE*, 2008, pp. 1513–1516.
 - [48] H. Iwata and S. Sugano, “Whole-body covering tactile interface for human robot coordination,” in *Robotics and Automation, 2002. Proceedings. ICRA’02. IEEE International Conference on*, 2002, vol. 4, pp. 3818–3824.
 - [49] G. Cannata and M. Maggiali, “An embedded tactile and force sensor for robotic manipulation and grasping,” in *Humanoid Robots, 2005 5th IEEE-RAS International Conference on*, 2005, pp. 80–85.
 - [50] G. Cannata and M. Maggiali, “Design of a Tactile Sensor for Robot Hands,” in *Sensors: Focus on Tactile Force and Stress Sensors*, no. December, J. G. Rocha and L.-M. Senentxu, Eds. InTech, 2008, pp. 271–288.
 - [51] L. B. Bridgewater, C. A. Ihrke, M. A. Diftler, M. E. Abdallah, N. A. Radford, J. M. Rogers, S. Yayathi, R. S. Askew, and D. M. Linn, “The robonaut 2 hand - Designed to do work with tools,” in *Robotics and Automation (ICRA), 2012 IEEE International Conference on*, 2012, pp. 3425–3430.
 - [52] R. Platt, C. Ihrke, L. Bridgewater, D. Linn, R. Diftler, M. Abdallah, S. Askew, and

References

- F. Permenter, “A miniature load cell suitable for mounting on the phalanges of human-sized robot fingers,” in *2011 IEEE International Conference on Robotics and Automation*, 2011, pp. 5357–5362.
- [53] H. Liu, P. Meusel, N. Seitz, B. Willberg, G. Hirzinger, M. H. Jin, Y. W. Liu, R. Wei, and Z. W. Xie, “The modular multisensory DLR-HIT-Hand,” *Mech. Mach. Theory*, vol. 42, no. 5, pp. 612–625, May 2007.
- [54] C. M. Oddo, M. Controzzi, L. Beccai, C. Cipriani, and M. C. Carrozza, “Roughness encoding for discrimination of surfaces in artificial active-touch,” *Robot. IEEE Trans.*, vol. 27, no. 3, pp. 522–533, 2011.
- [55] H. Takahashi, A. Nakai, N. Thanh-Vinh, K. Matsumoto, and I. Shimoyama, “A triaxial tactile sensor without crosstalk using pairs of piezoresistive beams with sidewall doping,” *Sensors Actuators, A Phys.*, vol. 199, pp. 43–48, 2013.
- [56] K. Noda, K. Hoshino, K. Matsumoto, and I. Shimoyama, “A shear stress sensor for tactile sensing with the piezoresistive cantilever standing in elastic material,” in *Sensors and Actuators, A: Physical*, 2006, vol. 127, no. 2, pp. 295–301.
- [57] K. Noda, K. Matsumoto, and I. Shimoyama, “Flexible tactile sensor sheet with liquid filter for shear force detection,” in *Proceedings of the IEEE International Conference on Micro Electro Mechanical Systems (MEMS)*, 2009, pp. 785–788.
- [58] M. Y. Cheng, C. L. Lin, Y. T. Lai, and Y. J. Yang, “A polymer-based capacitive sensing array for normal and shear force measurement,” *Sensors*, vol. 10, no. 11, pp. 10211–10225, 2010.
- [59] H. Lee, J. Chung, S. Chang, and E. Yoon, “Normal and Shear Force Measurement Using a Flexible Polymer Tactile Sensor With Embedded Multiple Capacitors,” *J. Microelectromechanical Syst.*, vol. 17, no. 4, pp. 934–942, 2008.
- [60] L. Viry, A. Levi, M. Totaro, A. Mondini, V. Mattoli, B. Mazzolai, and L. Beccai, “Flexible three-axial force sensor for soft and highly sensitive artificial touch,” *Adv. Mater.*, vol. 26, no. 17, pp. 2659–2664, 2014.
- [61] J. A. Dobrzynska and M. A. M. Gijs, “Polymer-based flexible capacitive sensor for three-axial force measurements,” *J. Micromechanics Microengineering*, vol. 23, no. 1, pp. 15009(1–11), 2013.
- [62] Analog Devices, “AD7147: CapTouch® Programmable Controller for Single-Electrode Capacitance Sensors (REV.D),” *Data Sheet*, <http://www.Analog>.

- com/static/imported-files/Data\Sheets/AD7147.pdf*, 2011.
- [63] S. Somlor, A. Schmitz, R. S. Hartanto, and S. Sugano, “A Prototype Force Sensing Unit for a Capacitive-type Force-Torque Sensor,” in *System Integration (SII), 2014 IEEE/SICE International Symposium on*, 2014, pp. 684–689.
 - [64] K. Kim, Y. Sun, R. M. Voyles, and B. J. Nelson, “Calibration of multi-axis MEMS force sensors using the shape-from-motion method,” *IEEE Sens. J.*, vol. 7, no. 3, pp. 344–351, 2007.
 - [65] E. Cheung and V. Lumelsky, “Development of sensitive skin for a 3D robot arm operating in an uncertain environment,” in *Proceedings, 1989 International Conference on Robotics and Automation*, 1989.
 - [66] E. Cheung and V. Lumelsky, “A sensitive skin system for motion control of robot arm manipulators,” *Rob. Auton. Syst.*, vol. 10, no. 1, pp. 9–32, 1992.
 - [67] S. Pratt, “AN-957 Application Note: Layout Guidelines for the AD7147 and AD7148 CapTouch Controllers,” pp. 2–5, 2008.
 - [68] Materion, “High Performance Electronic Spring & Connector Alloys.” [Online]. Available: <http://materion.com/Products/Alloys/SpringandConnectorAlloys.aspx>. [Accessed: 05-Sep-2014].
 - [69] I. National Bronze & Metals, “Beryllium Copper C17200 or Alloy 25 Copper.” [Online]. Available: <http://www.nbmmetals.com/c17200-beryllium-copper.html>. [Accessed: 05-Sep-2014].
 - [70] B. Davison, “Techniques for Robust Touch Sensing Design,” *AN1334 Microchip Technol. Inc*, pp. 1–28, 2010.
 - [71] V. Hayward, O. R. Astley, M. Cruz-Hernandez, D. Grant, and G. Robles-De-La-Torre, “Haptic interfaces and devices,” *Sens. Rev.*, vol. 24, no. 1, pp. 16–29, 2004.
 - [72] J. G. W. Wildenbeest, D. a. Abbink, C. J. M. Heemskerk, F. C. T. Van Der Helm, and H. Boessenkool, “The Impact of Haptic Feedback Quality on the Performance of Teleoperated Assembly Tasks,” *IEEE Trans. Haptics*, vol. 6, no. 2, pp. 242–252, 2013.
 - [73] A. Bolopion and S. Régnier, “A Review of Haptic Feedback Teleoperation Systems for Micromanipulation and Microassembly,” *IEEE Trans. Autom. Sci. Eng.*, vol. 10, no. 3, pp. 496–502, 2013.

References

- [74] K. Kim and J. E. Colgate, “Haptic Feedback Enhances Grip Force Control of sEMG-Controlled Prosthetic Hands in Targeted Reinnervation Amputees,” *IEEE Trans. Neural Syst. Rehabil. Eng.*, vol. 20, no. 6, pp. 798–805, 2012.
- [75] T. R. Coles, D. Meglan, and N. W. John, “The Role of Haptics in Medical Training Simulators: A Survey of the State of the Art,” *IEEE Trans. Haptics*, vol. 4, no. 1, pp. 51–66, 2011.
- [76] T. Ohba, H. Kadone, and K. Suzuki, “An elastic link mechanism integrated with a magnetorheological fluid for elbow orthotics,” in *2012 IEEE/RSJ International Conference on Intelligent Robots and Systems*, 2012, pp. 2789–2794.
- [77] D. S. Walker, D. J. Thoma, and G. Niemeyer, “Variable impedance magnetorheological Clutch Actuator and telerobotic implementation,” *2009 IEEE/RSJ Int. Conf. Intell. Robot. Syst. IROS 2009*, pp. 2885–2891, 2009.
- [78] C. R. Liao, D. X. Zhao, L. Xie, and Q. Liu, “A design methodology for a magnetorheological fluid damper based on a multi-stage radial flow mode,” *Smart Mater. Struct.*, vol. 21, no. 8, p. 085005, 2012.
- [79] B. Heintz, P. Fauteux, D. Létourneau, F. Michaud, and M. Lauria, “Using a Dual Differential Rheological Actuator as a high-performance haptic interface,” *IEEE/RSJ 2010 Int. Conf. Intell. Robot. Syst. IROS 2010 - Conf. Proc.*, no. 5, pp. 2519–2520, 2010.
- [80] J. Ulmen and M. Cutkosky, “A robust, low-cost and low-noise artificial skin for human-friendly robots,” in *Robotics and Automation (ICRA), 2010 IEEE International Conference on*, 2010, pp. 4836–4841.
- [81] M. Maggiali, G. Cannata, P. Maiolino, G. Metta, M. Randazzo, and G. Sandini, “Embedded Distributed Capacitive Tactile Sensor,” in *11th Mechatronics Forum Biennial International Conference*, 2008.

LIST OF PUBLICATION

Related publication

S. Somlor, A. Schmitz, R. S. Hartanto, and S. Sugano, “First Results of Tilted Capacitive Sensors to Detect Shear Force,” *Procedia Comput. Sci.*, 2015. – Best Paper Award at 2015 IEEE International Symposium on Robotics and Intelligent Sensors (IEEE-IRIS 2015), Langkawi, Malaysia.

S. Somlor, R. S. Hartanto, A. Schmitz, and S. Sugano, “A Novel Tri-axial Capacitive-Type Skin Sensor,” *Adv. Robot.*, vol. 29, no. 21, pp. 1375–1391, 2015.

S. Somlor, G. A. Dominguez, A. Schmitz, M. Kamezaki, and S. Sugano, “A Haptic Interface with Adjustable Stiffness Using MR Fluid,” in *Advanced Intelligent Mechatronic (AIM), 2015 IEEE/ASME International Conference on*, 2015, pp. 1132 – 1137.

S. Somlor, A. Schmitz, R. S. Hartanto, and S. Sugano, “A Prototype Force Sensing Unit for a Capacitive-type Force-Torque Sensor,” in *System Integration (SII), 2014 IEEE/SICE International Symposium on*, 2014, pp. 684–689.

Additional publication

T. P. Tomo, S. Somlor, A. Schmitz, S. Hashimoto, S. Sugano, and L. Jamone, “Development of a hall-effect based skin sensor,” in *SENSORS, 2015 IEEE*, 2015, pp. 1– 4.

List of Publication

S. Funabashi, A. Schmitz, T. Sato, S. Somlor, and S. Sugano, “Robust in-hand manipulation of variously sized and shaped objects,” in *Intelligent Robots and Systems (IROS), 2015 IEEE/RSJ International Conference on*, 2015, pp. 257–263.

A. Schmitz, S. Bhavaraju, S. Somlor, G. A. Dominguez, M. Kamezaki, W. Wang, and S. Sugano, “A Concept for a robot arm with adjustable series clutch actuators and passive gravity compensation for enhanced safety,” in *Advanced Intelligent Mechatronics (AIM), 2015 IEEE International Conference on*, 2015, pp. 1322–1327.

A. Schmitz, T. Sato, S. Funabashi, S. Somlor, S. Sugano, “TWENDY-ONE’s Hand: Combining the Benefits of Dexterity, Passive Compliance and Tactile Sensing,” in *IEEE International Conference on Robotics and Automation (ICRA 2015), Workshop on “Robotic Hands, Grasping, and Manipulation”*, 2015.

T. Sato, A. Schmitz, S. Funabashi, S. Somlor, S. Sugano, “Compliance and Learning for Robust In-Hand Manipulation of Variously Sized and Shaped Objects,” in *IEEE International Conference on Robotics and Automation (ICRA 2015), Workshop on “Compliant and Versatile Robot Control in Human Environments: Bridging the Gap between Learning and Control”*, 2015.

R.S. Hartanto, S. Somlor, A. Schmitz, S. Sugano, “A Design for Distributed Capacitive-Type Skin Sensor” in *JSME 27th Robotics and Mechatronics Conference (ROBOMECH 2015)*, 2015.